

LASER POWDER BED FUSION OF LOW AND
NEGATIVE THERMAL EXPANSION
METAMATERIALS

LASER POWDER BED FUSION OF LOW AND NEGATIVE THERMAL EXPANSION
METAMATERIALS

By

DEVASHISH DUBEY, B.TECH

A Thesis Submitted to the School of Graduate Studies in Partial Fulfillment of the
Requirements for the Degree of Master of Applied Science

McMaster University© Copyright by Devashish Dubey, September 2024

MASTER OF APPLIED SCIENCE (2024)
(Mechanical Engineering)

McMaster University
Hamilton, Ontario

TITLE: Laser Powder Bed Fusion of Low and Negative
Thermal Expansion Metamaterials

AUTHOR: Devashish Dubey
B.Tech. in Mechanical Engineering

SUPERVISOR: Dr. Mohamed A. Elbestawi

NUMBER OF PAGES: xviii, 191

Preface

This M.A.Sc. thesis is an integrated article thesis, also known as sandwich thesis, which has been composed of five main chapters all focusing on the laser powder bed fusion additive manufacturing of negative thermal expansion metamaterials composed of metal alloys. The chapters represent papers which are either published or under consideration for publication in authentic international journals.

Chapter 1 provides a comprehensive literature review on the design, fabrication and applications of negative thermal expansion metamaterials. The work presented in this chapter was previously published in the journal “*Journal of manufacturing and materials processing*” as “Negative Thermal Expansion Metamaterials: A Review of Design, Fabrication, and Applications” by Devashish Dubey, Anoshe Sadat Mirhakimi and Mohamed A. Elbestawi.

Chapter 2 is focused on the design, simulation and laser powder bed fusion of negative thermal expansion metamaterials made of grade 304L Stainless Steel and grade 300 Maraging Steel. The work presented in this chapter is a research paper which focuses on additive manufacturing of steel metamaterials with low and negative thermal expansion and is authored by Devashish Dubey, Eskandar Fereiduni, Mohamed A. Elbestawi, Mehedi H. Mahfuz, and Ryan Berke.

Chapter 3 deals with the design, simulation and laser powder bed fusion of negative thermal expansion metamaterials made of Grade 304L Stainless Steel and Invar 36 alloy. The work presented in this chapter is a research paper focused on negative thermal expansion lattices using laser powder bed fusion of SS304L and Invar 36 and is authored by Devashish Dubey, Eskandar Fereiduni, Mohamed A. Elbestawi, Mehedi H. Mahfuz, and Ryan Berke.

Chapter 4 summarizes the main conclusions and contribution of the thesis, highlights the

strengths, and limitations, and presents some suggestions for future work.

I declare that this thesis is an original report of my research, has been written by me and has not been submitted for any previous degree.

Devashish Dubey

September 2024

Abstract

Laser Powder Bed Fusion (LPBF) is a metal additive manufacturing (AM) technique that creates objects layer by layer from a bed of loose powder, using a laser beam as the heat source. This layer-wise approach allows for the fabrication of highly complex structures and intricate geometries with high accuracy, including solid, porous, and lattice structures. LPBF offers significant potential for use in industries such as aerospace, biomedical, and automotive due to its ability to fabricate unique and sophisticated designs. This technology has recently attracted significant attention for the fabrication of multimaterial parts with improved properties and applicability in different fields. However, challenges persist in understanding the relationship between process parameters and the properties of resulting multimaterial parts and interfaces. Additionally, limitations exist in design and interface selection for multimaterial fabrication using this technique. Negative thermal expansion (NTE) metamaterials, discussed in this research, are mechanical structures that show negative expansion properties by contracting with increase in temperature, while expanding with a decrease in temperature. These metamaterials are typically multimaterial systems where constituents with positive coefficients of thermal expansion (CTE) are strategically integrated, resulting in an overall NTE effect in one or more directions

This research focuses on the design, simulation, and fabrication of negative thermal expansion (NTE) metamaterials using Laser Powder Bed Fusion (LPBF) with Grade 304L Stainless Steel (SS304L), Grade 300 Maraging Steel (MS300), and Invar 36 (Invar) alloys. Bimaterial combinations of SS304L-MS300 and SS304L-Invar were explored. After determining the optimal processing parameters, results showed that a robust, defect-free interface could be

achieved in both combinations. Various lattice structures were designed based on these alloy pairs and analyzed using finite element analysis. The designs with the high NTE potential were successfully fabricated through LPBF, using optimal interface parameters. Thermal expansion testing of the fabricated structures demonstrated NTE behavior in line with FEA analysis predictions.

*To my parents,
I owe you everything.*

Acknowledgments

I would like to begin by expressing my deep gratitude to my supervisor, Professor Mohamed Elbestawi, whose guidance and mentorship have been invaluable. Your insightful feedback has significantly improved my work, encouraging me to refine my ideas and raise the standard of my research. I am truly grateful for your constant support and patience throughout this journey.

It has been an honor to be a part of the Additive Manufacturing Group (AMG) at McMaster University, and I extend my sincere thanks to my colleagues, especially Dr. Eskandar Fereiduni and Hosseinali Shiravi, for their engaging discussions and continuous encouragement. I would also like to acknowledge the Center for Advanced Nuclear Systems (CANS) at McMaster University for providing access to the electron backscattered diffraction (EBSD) analysis facilities. My special thanks go to our collaborators, Mehedi Hasan Mahfuz and Dr. Ryan Berke from the Department of Mechanical and Aerospace Engineering at Utah State University, USA, for their valuable expertise and support with Digital Image Correlation (DIC) testing.

Lastly, I am deeply thankful to my parents for their unwavering support, trust, and encouragement. Their endless patience and faith in me have shaped who I am today. They have always motivated me to explore new opportunities and strive towards my goals, and for that, I dedicate this accomplishment to them. This achievement would not have been possible without their support.

Contents

	Page
1 Chapter 1 Introduction and literature review.....	1
1.1 Introduction.....	3
1.2 Design.....	4
1.2.1 Bending-Based Architectures	5
1.2.2 Stretch-Based Architectures	8
1.2.3 Other Designs	12
1.3 Fabrication	17
1.3.1 Metal Additive Manufacturing Techniques.....	17
1.3.2 Conventional Manufacturing Techniques and Multimaterial Fabrication.....	30
1.3.3 Comparison of Microstructural Properties in AM and CM Processes	34
1.3.4 Material Selection for NTE Architectures	38
1.4 Prospective Applications	42
1.4.1 Electronic Packaging	43
1.4.2 Fuel Cells.....	46
1.4.3 Dental Implants.....	51
1.4.4 Space Structures	53
1.5 Conclusions.....	55
References.....	58
2 Chapter 2 Additive Manufacturing of Steel Metamaterials with Low and Negative Thermal Expansion	102
2.1 Introduction.....	104

2.2	Experimental Details	108
2.2.1	Materials and Machine	108
2.2.2	Fabrication of Solid Samples.....	109
2.2.3	Material Characterization	110
2.2.4	Mechanical Testing.....	111
2.2.5	Lattice Structures.....	112
2.2.6	Expansion Simulations	115
2.2.7	Fabrication of metamaterial lattices.....	117
2.2.8	Thermal Expansion Testing.....	117
2.3	Results and Discussion.....	118
2.3.1	Interfacial Process Optimization.....	118
2.3.2	Interfacial Microstructural Analysis	123
2.3.3	Interfacial Crystallographic Analysis	129
2.3.4	Mechanical Performance Analysis	131
2.3.5	Simulation.....	134
2.3.6	Experimental Thermal Testing	136
2.4	Conclusion	138
	References.....	142
3	Chapter 3 Negative Thermal Expansion lattices using laser powder bed fusion of SS304L and Invar 36	151
3.1	Introduction.....	153
3.2	Experimental Details	156
3.2.1	Machine and Materials	156
3.2.2	Fabrication of Characterization Samples.....	157

3.2.3	Material Characterization	157
3.2.4	Mechanical Testing.....	158
3.2.5	Design of Lattice Structures	158
3.2.6	Finite Element Simulations	161
3.2.7	LPBF fabrication of lattices.....	162
3.2.8	Thermal Expansion Testing.....	163
3.3	Results and Discussion.....	163
3.3.1	Process Optimization	163
3.3.2	Microstructural Analysis	166
3.3.3	Crystallographic Analysis.....	170
3.3.4	Mechanical Performance Analysis	172
3.3.5	Simulation.....	174
3.3.6	Experimental Thermal Testing	176
3.4	Conclusion	178
	References.....	181
4	Chapter 4 Summary, Strengths and Future Work.....	187
4.1	Summary.....	188
4.2	Strengths	189
4.3	Limitations.....	189
4.4	Future Work.....	190

List of figures

Figure 1.1 2D NTE metamaterials: (A) Bimaterial-strip-based: (a) Concept of bimaterial strip (Reprinted with permission from [12]; Copyright 1996 Springer Nature), (b) Cellular structure of bimaterial strips (Reprinted with permission from [12]; Copyright Springer Nature), and (c) Equilateral triangular lattice using curved bimaterial ribs [14]. (B) Multilayered strip with vertical NTE (Reprinted with permission from [19]; Copyright 2010 John Wiley and sons). (C) Chirality-based: (a) Chiral lattice with bimaterial strip ligaments where lighter blue and darker blue represent two different constituents (Reprinted with permission from [16]; Copyright 2015 John Wiley and sons), and (b) Bimaterial anti-tetrachiral and anti-trichiral lattice units (Reprinted with permission from [20]; Copyright 2016 American Chemical Society). (D) Stretch-based: (a) Triangular grid design (Reprinted with permission from [17]; Copyright 2007 The Royal Society (U.K.)), (b) Triangle lattice NTE (Reprinted with permission from [21]; Copyright 2007 Elsevier), and (c) Hexagonal lattice design (Reprinted with permission from [22]; Copyright 2016 Elsevier). (E) Others NTE designs: (a) Hoberman-circle-inspired design where red colour represents the constituent with larger CTE while blue represents constituent with lower CTE (Reprinted with permission from [23]; Copyright 2018 Elsevier), (b) Hexagonal grid design (Reprinted with permission from [24]; Copyright 2009 Elsevier), (c) Re-entrant structure where red colour represents the constituent with larger CTE while blue represents constituent with lower CTE (Reprinted with permission from [26]; Copyright 2017 Elsevier), and (d) X-shaped structure (Reprinted with permission from [37]; Copyright 2005 Springer Nature)..... 11

Figure 1.2 3D NTE Metamaterials: (a) Tetrakaidecahedral foam cell with bimaterial strips (Reprinted with permission from [13]; Copyright AIP Publishing), (b) Negative-CTE tetrahedron with material a having a low CTE and material b having a higher CTE (Reprinted with permission from [29]; Copyright 2007 AIP Publishing), (c) Cubic quarter octahedral structure (Reprinted with permission from [32]; Copyright 2017 Elsevier), (d) Anti-chiral 3D NTE structures (Reprinted with permission from [20]; Copyright 2016 ACS Publications), (e) Star-shaped structures based on 2D re-entrant designs [25]; Copyright 2018 Elsevier), and (f) Auxetic NTE structures (Reprinted with permission from [34]; Copyright 2021 Elsevier)..... 13

Figure 1.3 Comparison of powder bed fusion and direct energy deposition processes.	18
Figure 1.4 Laser powder bed fusion setup schematic.	19
Figure 1.5 Critical parameters in laser powder bed fusion.	21
Figure 1.6 Multimaterial combinations fabricated using LPBF in research. The direction of arrows shows the order of fabrication of the parts (Information obtained from references [44-49, 55-62]).	23
Figure 1.7 (a) Powder-based and (b) wire-based DED setups.	24
Figure 1.8 Critical parameters in direct energy deposition.	25
Figure 1.9 Multimaterial combinations fabricated using DED in research. The direction of arrows shows the order of fabrication (Information obtained from references [49, 76, 79, 82, 83, 85-87, 91, 94-126]).	27
Figure 1.10 Schematic diagrams of various CM processes (Reprinted with permission from [179]; Copyright 2020 Hasanov et al.)	34
Figure 1.11 Electron backscatter diffraction (EBSD) maps of (a) LPBF-AlSi10Mg and (b) cast aluminium alloy. EBSD pole figures of (c) LPBF-AlSi10Mg and (d) cast aluminium alloy; (e) grain size area in LPBF-AlSi10Mg and the cast alloy (Reprinted with permission from [219]; Copyright 2020 Elsevier).	37
Figure 1.12 The iron–aluminium phase diagram (Reprinted with permission from [227]; Copyright 1990 ASM International).	41
Figure 1.13 The copper–nickel phase diagram (Reprinted with permission from [227]; Copyright 1990 ASM International).	42
Figure 1.14 CTE mismatch in electronic packaging.	44
Figure 1.15 Young’s modulus and thermal expansion coefficient of semi-conductors and metals	

(data obtained from [238–240]).	45
Figure 1.16 Design of fuel cell (Reprinted with permission from [245]; Copyright 2013 John Wiley and sons).	46
Figure 1.17 Structure of a general dental implant (Reprinted with permission from [281]; Copyright 2022 Elsevier).	51
Figure 1.18 Fluctuating thermal environment in Earth’s orbit (Reprinted with permission from [295]; Copyright 2023 Yu et al., Licensee MDPI).	54
Figure 1.19 Negative expansion design by Milward et al. for cylindrical lens system meant for space applications (Reprinted with permission from [296]; Copyright 2017 Milward et al.).	55
Figure 1.20 Bimaterial hourglass hexagonal negative expansion design by Yu et al. (Reprinted with permission from [295]; Copyright 2023 Yu et al., Licensee MDPI).	55
Figure 2.1 (a) Specimen used for OM, SEM, Nano-hardness and scratch testing (b) Tensile Test Specimen after printing (c) Tensile Test Specimen after machining	112
Figure 2.2 Boundary Conditions for finite element analysis.	116
Figure 2.3 Change of alloys during fabrication of bimaterial lattices.	117
Figure 2.4 Density of optimized SS and MS samples.	119
Figure 2.5 Optical microscopy images of various samples fabricated for optimum PSP identification for the interface with variation of scanning speed as per design of experiments matrix. The samples within dotted enclosures are identified to be optimum.	122
Figure 2.6 Optical microscopy images of various samples fabricated for optimum PSP identification for the interface with variation of laser power as per design of experiments matrix. The samples within dotted enclosures are identified to be optimum.	123
Figure 2.7 Optical microscopy images (a) Melt pools as observed in maraging steel region; (b)	

Difference in melt pool depth at interface and bulk maraging steel; (c) Inward maragoni flow in melt pools at the interface; (d) Grain structure of maraging steel.....	125
Figure 2.8 Scanning Electron Microscopy images: (a) Melt pools in maraging steel (b) Microstructure of maraging steel (c) Entrapments in interfacial region (d) Partially melted boundary between two alloys at the interface	128
Figure 2.9 Alloying element distributions across the interface using linear EDS analysis. ...	129
Figure 2.10 Interfacial Electron Backscatter Diffraction data (a) Inverse Pole Figure – Z Map; (b) Correlative Phase Distribution Map ;(c) Band Contrast Map; (d) Kernel Average Misorientation Map.....	131
Figure 2.11 (a) Nano-hardness across the interface (b) Depth of penetration and acoustic emission across the interface.....	133
Figure 2.12 Finite element analysis results for vertical expansion for (a) Hexagonal Lattice with 0.5 mm MS strut thickness (b) Hexagonal Lattice with 1 mm MS strut thickness (c) Octagonal Lattice (d) Dodecagonal Lattice.....	135
Figure 2.13 Equivalent Von Mises Stress contours in hexagonal lattice with MS Strut thickness 0.5 mm.....	136
Figure 2.14 Deformation contours on the top face along the Z axis (axis of contraction) in Octagonal Bipyramid lattice. In this specimen-camera configuration, the Z-axis, perpendicular to the camera, aligns with the FEA-predicted contraction direction.....	137
Figure 3.1 Change of alloys during fabrication of bimaterial lattices.....	163
Figure 3.2 Interface observation using optical microscopy for process-parameter optimization	166
Figure 3.3 (a) Microstructure of Invar (b) microstructure of SS (c) Interfacial morphology (d) Marangoni flows and embedments at the interface (e) Interlayer observed in overetched sample	

(f) Interlayer at high magnification	167
Figure 3.4 Scanning Electron Microscopy images: (a)Melt pools in Invar (b) Microstructure of Invar (c) Observed Interface (d) Marangoni flow with interfacial melt pools at high magnification.....	169
Figure 3.5 (a) Alloying element distributions across the interface based on linear EDS analysis (b) Interlayer peak identification from Cr-distribution curve (c) Interlayer peak identification from Ni-distribution curve.	170
Figure 3.6 Interfacial Electron Backscatter Diffraction data (a) Inverse Pole Figure – Z Map; (b) Correlative Phase Distribution Map ;(c) Band Contrast Map; (d) Kernel Average Misorientation Map (e) Pole figures for SS (f) Pole figures for Invar.	171
Figure 3.7 Nano-hardness across the interface.....	173
Figure 3.8 (a) Depth of penetration, and (b) acoustic emission, across the interface using scratch resistance testing	174
Figure 3.9 Finite element analysis results for thermal expansion of lattices in vertical direction (a) A30 (b) A35 (c) A40 (d) A45	176
Figure 3.10 Vertical deformation in A30 lattice using DIC analysis.....	177

List of Tables

Table 1.1 A comparison of NTE architectures in the literature.	14
Table 1.2 Various metal–metal combinations printed using LPBF.	22
Table 1.3 Different material combinations in polymer AM.....	29
Table 1.4 Material types used in electronic packaging.	44
Table 1.5 Different types of fuel cells, their properties, and applications.	47
Table 1.6. CTE values of SOFC components (Reprinted with permission from [264]; Copyright 2020 Elsevier).	48
Table 2.1 Elemental composition of feedstock powders.....	109
Table 2.2 Metamaterial unit cells and lattice designs used in this study. SS and MS struts are shown in red and green colours respectively.	114
Table 2.3 Properties of SS and MS as used in FEA simulations.	117
Table 2.4 Optimum process parameters for alloys found in this study.....	119
Table 2.5 Design of experiments matrix used for identification of optimum process parameters for the interface	120
Table 2.6 Thermal expansion data from Finite Element Analysis.....	134
Table 3.1 Elemental composition of feedstock powder	156
Table 3.2 Metamaterial unit cells and lattice designs used in this study. SS 304L and Invar struts are shown in red and blue colours respectively.....	160
Table 3.3 Optimal process parameters determined for the two alloys.	164

Table 3.4 Design of experiments matrix used for identifying optimum process parameters for the interface	165
Table 3.5 Negative Thermal Expansion Performance of different lattices using FEA	175

1 Chapter 1 Introduction and literature review

Complete Citation:

Dubey D, Mirhakimi AS, Elbestawi MA. Negative Thermal Expansion Metamaterials: A Review of Design, Fabrication, and Applications. *Journal of Manufacturing and Materials Processing*. 2024; 8(1):40.

Negative Thermal Expansion Metamaterials: A Review of Design, Fabrication, and Applications

Abstract

Most materials conventionally found in nature expand with an increase in temperature. In actual systems and assemblies like precision instruments, this can cause thermal distortions which can be difficult to handle. Materials with a tendency to shrink with an increase in temperature can be used alongside conventional materials to restrict the overall dimensional change of structures. Such structures, also called negative-thermal-expansion materials, could be crucial in applications like electronics, biomedicine, aerospace components, etc., which undergo high changes in temperature. This can be achieved using mechanically engineered materials, also called negative thermal expansion (NTE) mechanical metamaterials. Mechanical metamaterials are mechanically architected materials with novel properties that are rare in naturally occurring materials. NTE metamaterials utilize their artificially engineered architecture to attain the rare property of negative thermal expansion. The emergence of additive manufacturing has enabled the feasible production of their intricate architectures. Industrial processes such as laser powder bed fusion and direct energy deposition, both utilized in metal additive manufacturing, have proven successful in creating complex structures like lattice formations and multimaterial components in the industrial sector, rendering them suitable for manufacturing NTE structures. Nevertheless, this review examines a range of fabrication methods, encompassing both additive and traditional techniques, and explores the diverse materials used in the process. Despite NTE metamaterials being a prominent field of research, a comprehensive review of these architected materials is missing in the literature. This article aims to bridge this gap by

providing a state-of-the-art review of these metamaterials, encompassing their design, fabrication, and cutting-edge applications.

Keywords: mechanical metamaterials; multimaterial 3D printing; additive manufacturing; laser powder bed fusion; direct energy deposition

1.1 Introduction

The control of thermal expansion is a critical requirement in present-day industrial applications. A strain change as small as 10^{-5} in linear distortion has the potential to cause fatal errors in high-precision machines and their components [1]. This is evident in the creation of cutting-edge contemporary sectors, such as semiconductor manufacturing, fuel cell technology, thermoelectric converters, electronic packaging, and so forth [2,3]. The fundamental technology used to regulate thermal expansion involves materials that exhibit negative thermal expansion (NTE) which shrink when heated [2,4–6]. Research on negative thermal expansion garnered significant interest after the discovery of isotropic NTE in ZrW_2O_8 in 1996 [7]. Later, several different compounds were found to exhibit NTE behavior in various temperature ranges [8–11]. The NTE behavior found in these materials was caused by the molecular level structure of the constituent compounds in their NTE temperature range. As such, it is also very difficult to find these rare materials in nature, and a substantial amount of effort is required to discover them. Nonetheless, in 1996, Lakes et al. discovered a novel method of producing negative thermal expansion behavior primarily using structural architecture instead of material properties [12]. He designed an NTE strip by attaching two different materials with different positive coefficients of thermal expansion [12]. Due to its highly material-independent approach, this work spurred remarkable progress in the field of mechanically engineered negative-thermal-

expansion materials also called “negative thermal expansion mechanical metamaterials” [13–35]. A metamaterial (deriving from the Greek word μετά (meta), meaning “beyond” and the Latin word materia, meaning “matter”) is a material engineered to have a property rarely found in natural materials. Mechanical metamaterials are metamaterials with engineered architectures that exhibit exotic properties, primarily governed by their structure rather than their composition. The primary exotic property is thermal expansion in NTE metamaterials. These metamaterials have the potential to achieve the same effect as those produced by rare, naturally available NTE materials. In this article, we will discuss the state-of-the-art design of their architectures, the potential to fabricate them using metal additive manufacturing techniques, and their applications. Hence, the article layout is as follows. First, a comprehensive review of different NTE architectures is discussed. Afterwards, two cutting-edge metal additive manufacturing processes, powder bed fusion (PBF) and direct energy deposition (DED), are reviewed to evaluate their potential to fabricate metal-based NTE metamaterials. Finally, we list excellent current and potential applications of NTE metamaterials to gauge their transformative potential.

1.2 Design

Since the advent of NTE metamaterials by Lakes et al. in the 1990s, several designs and structures have been proposed for achieving negative thermal expansion. Although they differ in structural designs, the main principle involves joining two or more constituents with different coefficients of thermal expansion (CTE) to generate a structure with an overall NTE. In this section, we have classified and reviewed different design methodologies from the literature so far. Based on the mechanics and failure modes of these architectures, they can primarily be

categorized as bending-based or stretch-based with many sub-classifications.

1.2.1 Bending-Based Architectures

These types of NTE designs work based on the principle of bending. Bending caused in the structure due to the differential expansion of two different bonded materials leads to an overall contraction in one or more directions. These structural designs can be further classified into the following:

1. Bimaterial-strip-based designs;
2. Chirality-based designs;
3. Re-entrant designs;
4. Other designs.

1.2.1.1 Bimaterial-Strip-Based Designs

In 1996, Lakes et al. [12] proposed a novel method for producing a cellular NTE structure using bimaterial strips. The strips were made from two materials with different CTE values. During an increase in temperature, a differential strain produced at the perfectly bonded interface produces curvature in the strip, which brings the endpoints closer to each other, thereby causing a contraction and leading to an overall negative CTE.

The CTE of the bimaterial strip is given by [12] as follows:

$$\alpha = \frac{l_{\text{arc}}}{(h_1 + h_2)} \times \frac{6(\alpha_2 - \alpha_1) \left(1 + \frac{h_1}{h_2}\right)^2}{3 \left(1 + \frac{h_1}{h_2}\right)^2 + \left(1 + \frac{h_1 E_1}{h_2 E_2}\right) \left(\left(\frac{h_1}{h_2}\right)^2 + \frac{h_2 E_2}{h_1 E_1}\right)} \times \left[\frac{1}{2} \cot\left(\frac{\theta}{2}\right) - \frac{1}{\theta}\right]$$

where layers E_1 and E_2 denote Young's moduli, α_1 and α_2 are the CTE values of the two materials, θ is the initial curvature of the strip, and h_1 and h_2 denote the thicknesses of strips 1 and 2. If the high-expansion material is placed on the convex side with a slow expanding

material on the concave side, a temperature increase will lead to the increased curvature of the strip and negative thermal expansion. The magnitude of the CTE is highly dependent on the ratio of the length of the strip to its thickness, which implies that slender strips have higher magnitudes of expansion, which are negative or positive depending on constituent orientation. In later works, Lakes and his group suggested the use of these bimaterial strips as edges of two-dimensional and tridimensional lattices with pin joints and analytically achieved negative thermal expansion in these units [13,14]. The curvature of these structures was deliberately minimized to enhance their stiffness. Nevertheless, as their functionality relies on bending induced by the differential expansion of the ribs, we categorize them as architectures primarily governed by bending. Based on the triangular 2D design proposed by Lehman and Lakes, Ha et al. assumed bonded joints (instead of pin joints) as they are more practical and used a finite element analysis to conclude that the structure still showed tunable thermal expansion characteristics with possible overall negative CTE [36].

Along with bimaterial strips, layers of multiple materials have also been used to achieve anisotropic negative thermal expansion. A pioneering work by Grima et al. [19] describes the use of thick layers of materials with low moduli and CTE values and a high Poisson's ratio combined with thin layers of materials with high moduli and CTE values and a significantly lower Poisson's ratio.

1.2.1.2 Chirality-Based Designs

In a novel work, Ha et al. alternately oriented bimaterial strips as edges in a chiral structure and achieved negative expansion properties [16]. The expression is given as follows:

$$\alpha = \frac{r}{4\rho_s} \frac{1}{\sqrt{1 + \left(\frac{2r}{L_{\text{rib}}}\right)^2}}$$

where ρ_s is the specific curvature.

Wu et al. also used bimaterial strips in anti-chiral structures to achieve this objective [20]. He ran simulations as well as experiments for his anti-trichiral and anti-tetrachiral bidimensional (2D) designs and then extended his work to tridimensional (3D) structures. The extent of the negativity of overall CTE in his designs was dependent on the node radii, the difference in the thermal expansion of the component materials, and the length of the joining ligaments between the nodes.

1.2.1.3 Re-Entrant Designs

A re-entrant structure is derived from a honeycomb structure by directing two opposite vertices of its hexagon inwards. Taking inspiration from the use of re-entrant structures in the field of auxeticity, Ai et al. proposed a re-entrant unit cell-based structure with several designs using two different materials and achieved negative thermal expansion along with a negative Poisson's ratio in their simulations [26]. Such structures are termed doubly negative structures. In another work, they made several 3D structures also based on the 2D re-entrant design as it was found to be most optimal in terms of achieving both NTE and auxeticity [25]. Later, Raminhos et al. fabricated a 2D re-entrant NTE design using the additive manufacturing of polymers and experimentally verified its properties [27]. Recently, Peng et al. developed novel hybrid honeycomb designs with enhanced stiffness and tuneable thermal expansion as well as auxeticity [35]. For 2D structures, they merged hexagonal honeycomb unit cells and produced re-entrant, semi-re-entrant, and non-re-entrant designs. In another work, they orthogonally

assembled and merged these planar designs to generate 3D unit cells [34].

1.2.1.4 Other Designs

There are a few bending-dominated structural designs proposed in the literature that do not fit into the above sub-classifications. For instance, Jefferson et al. proposed a hexagonal grid with inner elements made of a higher-CTE material to achieve a bending-based negative CTE design. They analytically evaluated its performance with different beam element-based models and predicted overall negative thermal expansion properties for the structure [24]. Another design proposed by Lim et al. was also found in the literature, exhibiting tunable thermal expansion characteristics [37]. Figure 1.1 and Figure 1.2 depict the 2D and 3D architectures of various designs discussed in this section respectively.

1.2.2 Stretch-Based Architectures

The structures based on bimaterial strips tend to be less stiff at higher temperatures due to bending, which is a necessity for NTE performance. Avoiding bending-dependent NTE unit cells can increase the overall strength and stiffness of the resultant structure. For designs without bimaterial struts, Deshpande et al. provided a criterion for stretch-based architectures which requires a minimum node connectivity of six for 2D structures and twelve for 3D ones [38]. A design that has a combination of nodes satisfying and not satisfying this criterion would lead to a stiffness lower than a fully stretch-based design; however, the resultant structure can still be stretch-dominated. The stretch-dominated designs made for negative CTE can be classified as follows:

1. Triangle-based;
2. Tetrahedron-based;
3. Octahedron-based;

4. Other designs.

1.2.2.1 Triangle-based

Grima et al. proposed a triangular 2D grid with tuneable thermal expansion capable of achieving negative CTE. Unlike strips or layers, this structure only required vertex–vertex contact of edges made of dissimilar materials [17]. Steeves et al. also proposed pin-jointed stretch-dominated designs using triangles that do not undergo bending at higher temperatures and thus have much higher stiffness and thermal fatigue-resistant properties [21] (figure 1.1).

Wei et al. took a similar approach with biomaterial-triangle-based designs and proposed various structural shapes for applications [22]. They also fabricated and assembled their designs using various metals and alloys with a high CTE difference, like aluminium and invar, and experimentally investigated the CTE along with stiffness. Li et al. introduced a Hoberman-circle-based NTE system [23]. By attaching radially aligned high-thermal-expansion rods in the middle-to-low-thermal-expansion rods of the Hoberman sphere, the overall structure exhibits negative thermal expansion. Upon heating, the central rods experience a greater amount of expansion than the rods of the Hoberman circle, thereby causing a contraction.

1.2.2.2 Tetrahedron-based

In a pioneering work, Lim and coworkers introduced an NTE design using tetrahedrons. By carefully making the base of the tetrahedron with materials with higher CTE values and the rest with lower-CTE material, the tetrahedron exhibits negative CTE in the vertical direction as well as an overall negative volumetric CTE in various cases [29]. Their work led to further research by Xu et al. in the domain of tetrahedron-based NTE designs. They designed various lattice structures based on bimaterial tetrahedrons, particularly thermally negative octet lattice designs [31].

1.2.2.3 Octahedron-based

Jin et al. presented a micro-lattice design with a cubic unit cell consisting of twelve quarter-octahedra at the edges. With the material type differing between the octahedral edges and cubic edges, the structure performed well analytically, with promising negative and zero CTE values [32]. In one of their works, Xu et al. utilized octet truss-based architectures to come up with multiple highly tuneable stretch-based designs. Both numerical as well as experimental methods were used to assess the CTE performance of the designs with Al6061 (high CTE) and Ti6Al4V (low CTE) as the constituents, and the structures were manufactured via the snap-fit assembly of metal sheets cut using a laser from the two materials [30].

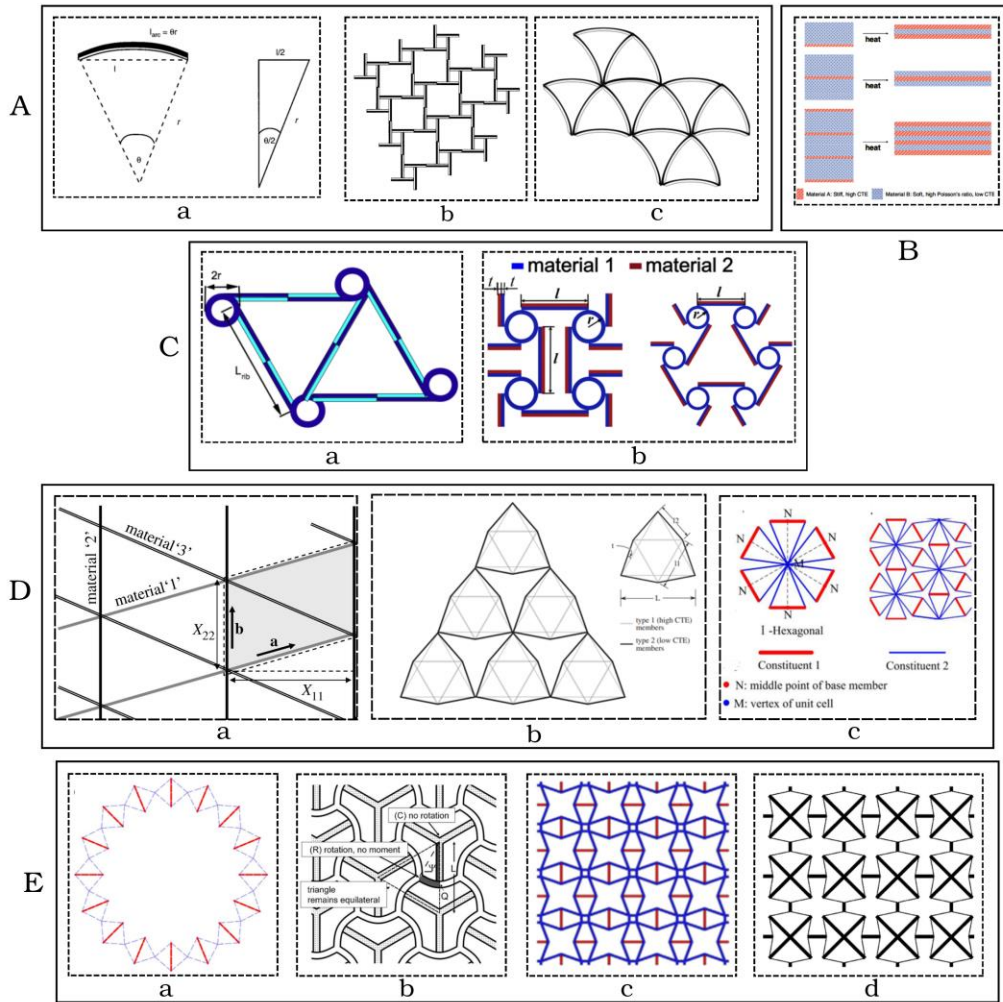


Figure 1.1 2D NTE metamaterials: (A) Bimaterial-strip-based: (a) Concept of bimaterial strip (Reprinted with permission from [12]; Copyright 1996 Springer Nature), (b) Cellular structure of bimaterial strips (Reprinted with permission from [12]; Copyright Springer Nature), and (c) Equilateral triangular lattice using curved bimaterial ribs [14]. (B) Multilayered strip with vertical NTE (Reprinted with permission from [19]; Copyright 2010 John Wiley and sons). (C) Chirality-based: (a) Chiral lattice with bimaterial strip ligaments where lighter blue and darker blue represent two different constituents (Reprinted with permission from [16]; Copyright 2015 John Wiley and sons), and (b) Bimaterial anti-tetrachiral and anti-trichiral lattice units (Reprinted with permission from [20]; Copyright

2016 American Chemical Society). (D) Stretch-based: (a) Triangular grid design (Reprinted with permission from [17]; Copyright 2007 The Royal Society (U.K.)), (b) Triangle lattice NTE (Reprinted with permission from [21]; Copyright 2007 Elsevier), and (c) Hexagonal lattice design (Reprinted with permission from [22]; Copyright 2016 Elsevier). (E) Others NTE designs: (a) Hoberman-circle-inspired design where red colour represents the constituent with larger CTE while blue represents constituent with lower CTE (Reprinted with permission from [23]; Copyright 2018 Elsevier), (b) Hexagonal grid design (Reprinted with permission from [24]; Copyright 2009 Elsevier), (c) Re-entrant structure where red colour represents the constituent with larger CTE while blue represents constituent with lower CTE (Reprinted with permission from [26]; Copyright 2017 Elsevier), and (d) X-shaped structure (Reprinted with permission from [37]; Copyright 2005 Springer Nature).

1.2.3 Other Designs

This section includes architectures that cannot be particularly classified as bending or stretch-based. In a related work, Lim et al. proposed ring rod assembly-based structures [28]. The unit cell of the design consists of a ring with two rods attached diametrically opposite to each other with each rod protruding out through a hole in the ring on the opposite side. Starting from a 2D structure, they developed 3D arrays of double rings as well. In addition to having thermally negative coefficients, his designs also showed auxetic behavior. Juasiripukdee et al. designed a tessellated cellular structure for a controlled thermal expansion frame for high-precision instruments. They used a high-expansion cylindrical part fitted inside an outer lattice part and numerically confirmed their results [33]. This is an example of a real-world use of controlled thermal expansion.

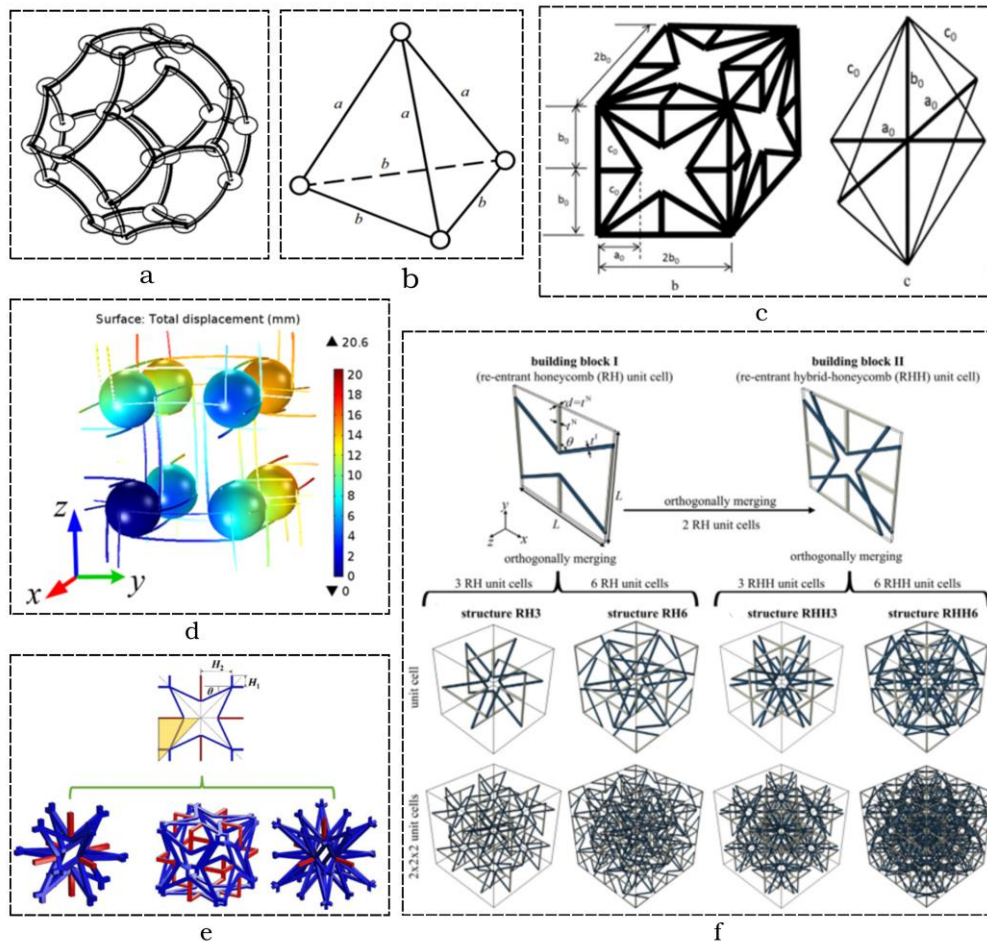


Figure 1.2 3D NTE Metamaterials: (a) Tetrakaidecahedral foam cell with bimaterial strips (Reprinted with permission from [13]; Copyright AIP Publishing), (b) Negative-CTE tetrahedron with material a having a low CTE and material b having a higher CTE (Reprinted with permission from [29]; Copyright 2007 AIP Publishing), (c) Cubic quarter octahedral structure (Reprinted with permission from [32]; Copyright 2017 Elsevier), (d) Anti-chiral 3D NTE structures (Reprinted with permission from [20]; Copyright 2016 ACS Publications), (e) Star-shaped structures based on 2D re-entrant designs [25]; Copyright 2018 Elsevier), and (f) Auxetic NTE structures (Reprinted with permission from [34]; Copyright 2021 Elsevier).

Along with a difference in their design and structures, these works also vary in terms of the constituent materials used, type of analysis, fabrication methods, and achievable CTE values. Initial works in the field tend to be analytical with mathematical derivations or computational using simulation programs; however, recent works also include fabricated models of proposed architectures. A comprehensive comparison of various designs is depicted in Table 1.1. The fabrication methods are diverse, ranging from a basic assembly to fully 3D-printed models while the materials vary from polymers to metals.

Table 1.1 A comparison of NTE architectures in the literature.

Classification	Design	Researchers	Constituent Materials	CTE ($\times 10^{-6}$ m/m°C)	Type of Analysis	Fabrication Method	Ref.
Bending-based Architectures							
Bimaterial-Strip-based	Single bimaterial strip	Lakes et al.	-	Unbounded	Analytical	-	[12]
	Honeycomb lattice using bimaterial strip	Lakes et al.	Steel, invar	-10^3 to 10^3	Analytical	-	[13]
	Triangular lattice using bimaterial strip	Lehman et al.	Steel, invar	Zero, tuneable as negative or positive	Analytical	-	[14]
	Triangular and square lattices using bimaterial strip	Ha et al.	Steel, invar	Triangular lattice: -0.03 to 6.67 ; Square lattice: Zero	Computational	-	[36]
	Multilayered strip (three or	Grima et al.	Polyvinylidene chloride,	Zero to -ve values (tuneable)	Analytical, Computational	-	[19]

	more layers)		silicone rubber				
Chirality-based	2D triangular chiral lattice	Ha et al.	Alloy 1 (72%Mn, 18%Cu, 10%Ni), Alloy 2 (invar)	-350	Experimental	Bonding glue: Loctite type 491 cement	[16]
	2D anti-tetrachiral and trichiral lattices, 3D anti-tetrachiral lattice	Wu et al.	2D lattices: Aluminium, copper; 3D lattice: VeroWhitePlus RGD835 and TangoPlus FLX930 polymers	2D anti-tetrachiral : -70 to -35; 2D anti-trichiral: -45 to zero; 3D anti-tetrachiral : -700 to -100	Computational, Experimental	2D lattices: Screwed fittings; 3D lattice: Multimaterial polymer 3D printing (Objet350 connex2, Stratasys Ltd., Eden Prairie, MN, USA)	[20]
Re-entrant-based	Re-entrant cell-based four different 2D lattices	Ai et al.	Aluminium, steel, and invar (any two constituents per lattice)	-41 to 14.4 (Highly tuneable)	Computational	-	[26]
	Basic re-entrant unit cell lattice	Raminhos et al.	Two combinations: Nylon, Polyvinyl alcohol compound (PVA); Polypropylene (PP), Copolyester (CPE+)	-1568 to 498 in different combinations	Experimental	Fused filament fabrication 3D printing (Ultimaker 3™)	[27]
	Modified re-entrant unit cell-based 2D and 3D lattices	Peng et al.	Al6061, invar	-75 to 23 for 2D; -368 to 575 for 3D; Tuneable	Analytical, Computational	-	[34,35]
	Hexagonal grid-	Jefferson et al.	-	Tuneable	Analytical, Computational	-	[24]

Other bending-based designs	shaped lattice						
	X-shaped 2D lattice	Lim et al.	-	Tuneable	Analytical	-	[37]
Stretch-based Architectures							
Triangle-based	2D triangular lattice	Grima et al.	-	Tuneable as +ve, zero or -ve	Analytical	-	[17]
	Triangular lattice with inscribed triangles	Steeves et al.	Al7075-T6, Ti6Al4V	0 to 42	Analytical, Computational, Experimental	Laser cutting from sheets, assembly using Brazing/laser welding	[21]
	2D Hexagonal lattices	Wei et al.	Al7075, SS431, invar (Any two in one lattice)	Al-invar: -5 to Zero; Al-SS: 30; Tuneable	Analytical, Experimental	Electric discharge machining of members from sheets; Interference fit assembly using grooves	[22]
	Hoberman-sphere-inspired lattice	Li et al.	Elastomer, glassy polymer	-1040 to 10	Analytical, Computational, Experimental	Multimaterial polymer 3D printing (Objet260 Connex, Stratasys Ltd.)	[23]
Tetrahedron-based	Tetrahedral lattice	Lim et al.	-	Tuneable	Analytical	-	[29]
	Tetrahedral lattices: Stationary/non-stationary concept-based line	Xu et al.	Al6061, Ti6Al4V, invar (Al6061-Ti6Al4V and Al6061-invar combinations)	-35 to 10, Tuneable	Analytical, Computational, Experimental	Pin-jointed interference fit metallic bars bonded using epoxy glue	[31]
Octahedron-based	Cubic cell	Jin et al.	-	Tuneable +ve, zero or -ve	Analytical	-	[32]
	Octet lattice	Xu et al.	Al6061, Ti6Al4V	Anisooctet design:	Computational, Experimental	Pretension snapping of laser-	[30]

				-366 to 10.9; Iso-octet design: 0.273 to 11.3		cut members using epoxy glue	
Other designs	Ring rod sliding structure	Lim et al.	-	Tunable as +ve, zero or -ve	Analytical	-	[28]
	Lattice-based machine frame design	Juasiripukdee et al.	Nylon 12, Ultra-high-molecular-weight polyethylene (UHMWPE)	0.001	Computational, Experimental	Nylon 12 outer part used polymer LPBF; Inner UHMWPE part used conventional manufacturing	[33]

1.3 Fabrication

From the previous section, it can be seen that the fabrication of negative thermal expansion materials requires two or more materials to be fused in a design. Multimaterial fabrication has been attempted successfully in the literature using diverse materials and various manufacturing methods, including additive and conventional manufacturing methods as well as materials like polymers and metals. This segment provides an extensive examination of diverse fabrication methods for multi-material applications in research, their advantages and limitations, and the essential characteristics needed in multimaterial combinations to effectively generate NTE architectures.

1.3.1 Metal Additive Manufacturing Techniques

In the field of metal additive manufacturing (AM), PBF (powder bed fusion) and the DED (direct energy deposition) techniques stand out as the most established manufacturing processes. These methods involve adding a powdered metal or occasionally other forms like wire in DED,

followed by melting using a focused thermal energy source, either simultaneously or sequentially. Unlike most additive manufacturing processes used for plastics or polymers, PBF and DED rely on electron beams, laser beams, or similar heat sources to achieve bonding between layers of metal. This is essential due to the high fusion enthalpy and melting temperatures of metals [39]. AM outperforms traditional manufacturing techniques when a high level of complexity or customization is required with a lower production volume [40]. Combined with their multimaterial fabrication capabilities, PBF and DED techniques are very promising in the fabrication of NTE metamaterials. A depiction of similarities and differences between the two processes is provided in Figure 1.3.

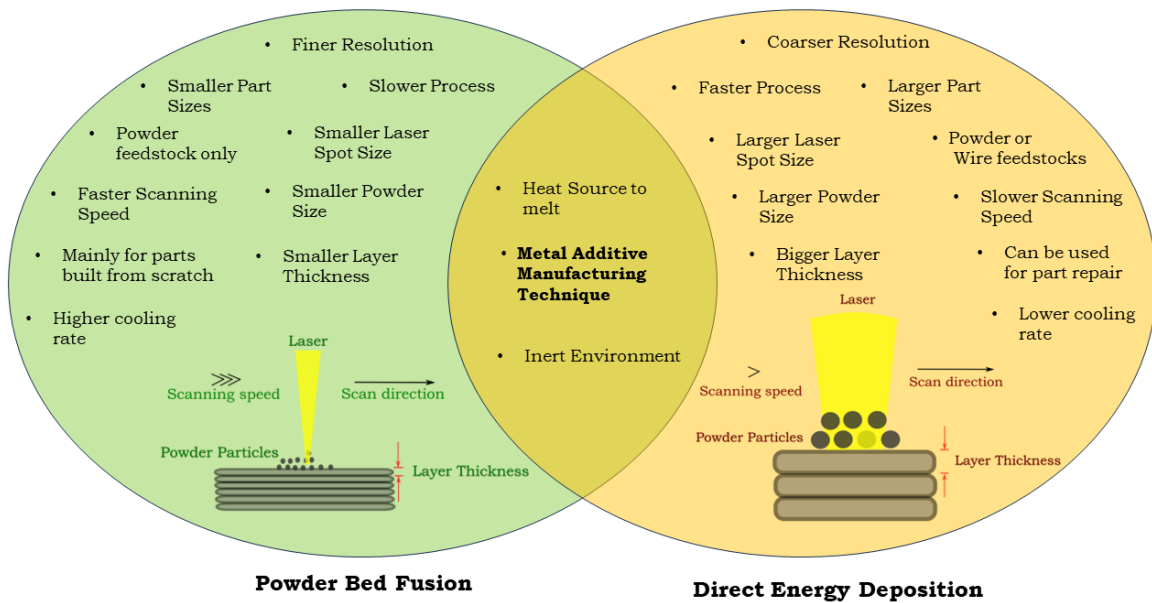


Figure 1.3 Comparison of powder bed fusion and direct energy deposition processes.

1.3.1.1 Laser Powder Bed Fusion

LPBF is an additive manufacturing technique employed to manufacture complex parts and components. A lot of metals and alloys have been successfully processed using this method. The layout of the machine usually consists of a heat source (laser or electron beam), a powder bed build platform, a powder storage system, a powder delivery system, and an overflow reservoir. Figure 1.4 depicts the layout of an LPBF machine. For fabrication, a substrate build plate is first fixed onto the machine's build platform and then the chamber environment is made inert primarily using nitrogen or argon.

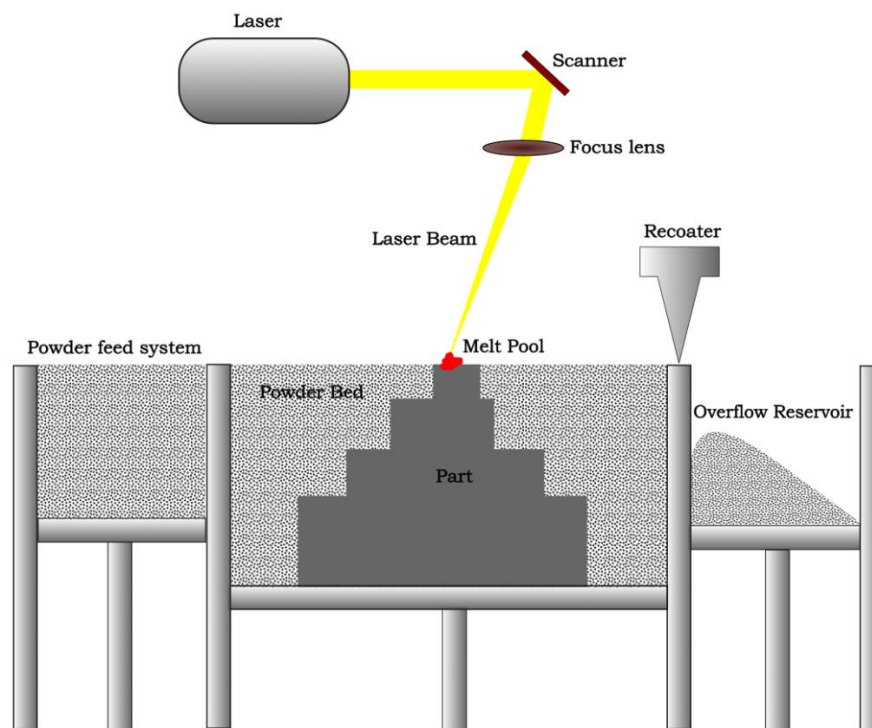


Figure 1.4 Laser powder bed fusion setup schematic.

After the first layer of powder is deposited based on a predefined layer thickness, the laser scans

the powder layer in a predetermined path, thereby melting and solidifying the selected areas. Afterwards, the build platform is lowered, a new layer is deposited, and the process repeats itself until the part is fully manufactured. Initially devised for single-material parts, modifications have been made by researchers in LPBF machines to attempt to produce parts made of more than one type of material. Table 1.2 provides a list of the metal–metal combinations that have been successfully fabricated and industrialized. Since almost all structure-based negative expansion metamaterial designs utilize multiple materials, LPBF provides an opportunity to manufacture negative thermal expansion metamaterials. Also, as a metal-based manufacturing technique, LPBF can open doors to the production of a wide variety of NTE structures using metals in industry. The interaction of laser beams with metal powder leads to the occurrence of complex thermal and physical phenomena in the melt pool [41].

The degree of melting and rate of solidification which directly affect the produced part depend upon various factors, such as the laser power, scanning speed, hatch spacing, layer thickness, and characteristics of the metal powder used [42,43]. A list of the critical parameters in LPBF is provided in Figure 1.5.

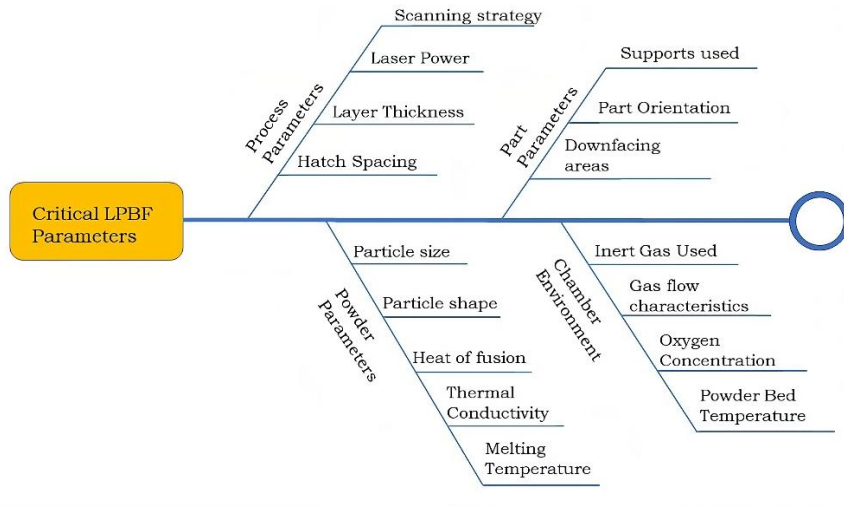


Figure 1.5 Critical parameters in laser powder bed fusion.

However, not all materials can be successfully printed together using LPBF. The interfacial bond strength is one of the primary factors to consider when trying to attach two dissimilar metals using this technique [44–49]. A useful parameter, energy density E , is used in LPBF to calculate the effect of these multiple factors and is defined as follows [50]:

$$E = \frac{P}{v \times h \times t}$$

where P is the laser power, v is the scanning speed, h is the hatch spacing, and t is the layer thickness. If the energy density is too high, it causes splashing in the melt pool, leading to a balling effect, which can increase roughness at the surface [51]. A high E can also cause keyhole porosity formation due to metal vaporization [52,53]. A low E causes insufficient powder melting, leading to the surrounding particles sticking to contour tracks.

In multi-metal parts fabricated using LPBF, the optimization of energy density can reduce defects. This has been successfully observed in maraging steel–copper bimetal parts [49]. Different CTE values and thermal conductivities of steel and copper cause residual stresses,

which cause weak bonding and hence induce cracking at the interface. A higher energy density tends to alleviate this problem. A decrease in residual stresses and thereby the balling effect can also be achieved by optimizing the scanning strategy. During the fabrication of SS316L and 18Ni300 bimetallic structures, island and interlayer staggered scanning strategies were found to be useful [46]. In a CuSn and 18Ni300 bimetal structure, remelting scanning achieved lower levels of elongation and tensile stress [54]. The ability of LPBF to produce multimaterial prints combined with ongoing research in this direction promises the success of this process in manufacturing negative-thermal-expansion metamaterials with the limitation of smaller part sizes. Figure 1.6 depicts these materials in their order of fabrication.

Table 1.2 Various metal–metal combinations printed using LPBF.

Metal–Metal Combinations	Powders Used	References
Iron–Iron	Maraging Steel, H13 Maraging Steel, 4Cr13 Steel	[55,56]
Aluminium–Aluminium	Al12Si, Al3.5Cu1.5Mg1Si	[57]
Titanium–Titanium	Ti6Al4V, Ti5Al2.5Sn	[58]
Titanium–Iron	Ti6Al4V, K220Cu, SS316L	[59]
Titanium–Nickel	Ti6Al4V, IN718	[60]
Iron–Nickel	SS316, IN718	[45]
Copper alloy–Iron	Cu10Sn, SS316L	[44,46,61]
Pure Copper–Iron	Cu, Maraging Steel	[49]
Aluminium–Copper	AlSi10Mg, C18400	[47]
Tungsten–Copper	Pure W, CuA	[62]

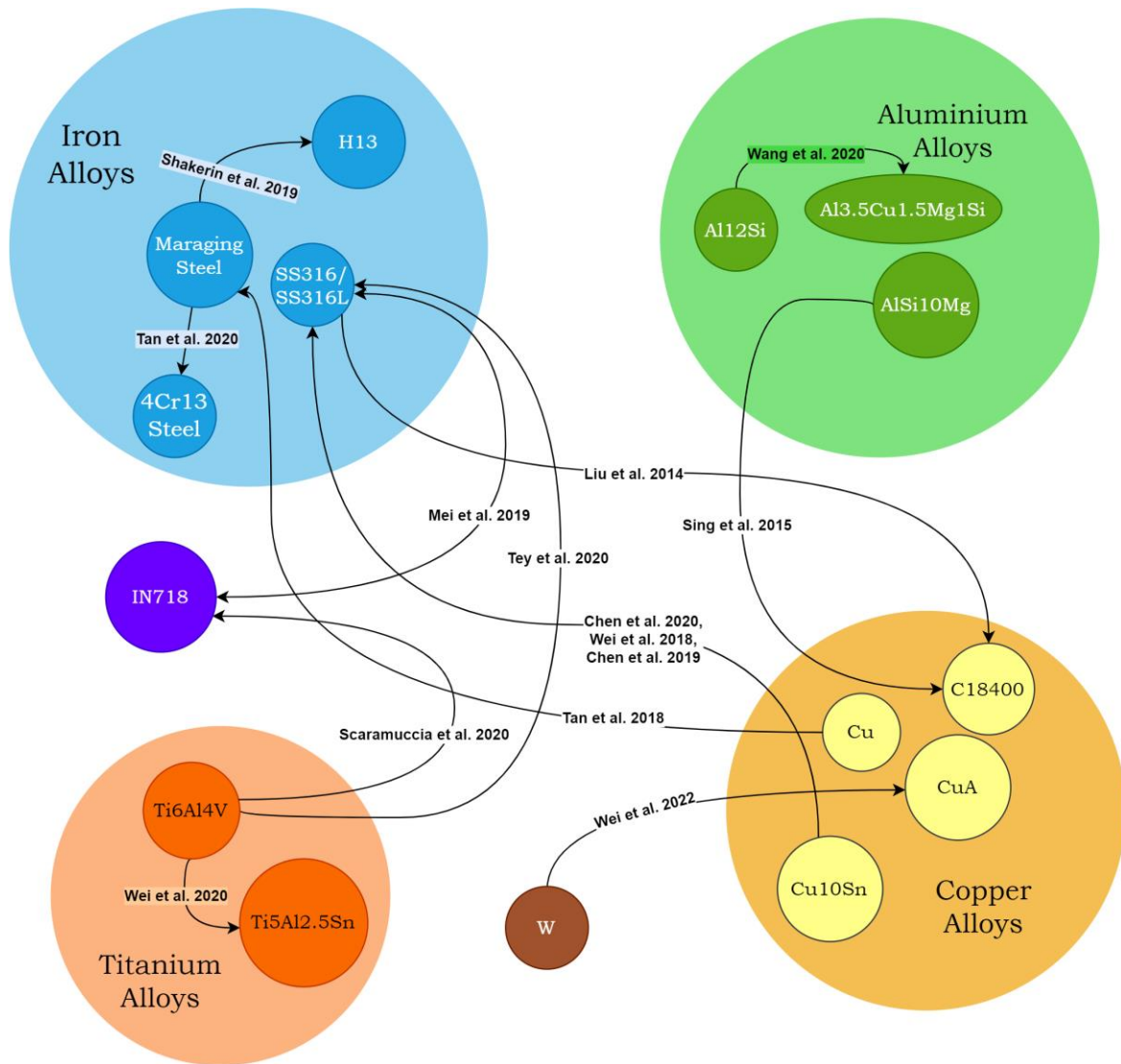


Figure 1.6 Multimaterial combinations fabricated using LPBF in research. The direction of arrows shows the order of fabrication of the parts (Information obtained from references [44-49, 55-62]).

1.3.1.2 Direct Energy Deposition

DED is an additive manufacturing process that utilizes focused thermal energy to fuse materials by melting as they are being deposited (Figure 1.7). A heat source, like a laser or electron beam, is focused on the material being deposited, which is supplied either in the form of a blown

powder or via a wire system [63,64]. Depending on the feedstock, DED processes can be classified as follows [65,66]:

1. Powder feeding;
2. Wire feeding.

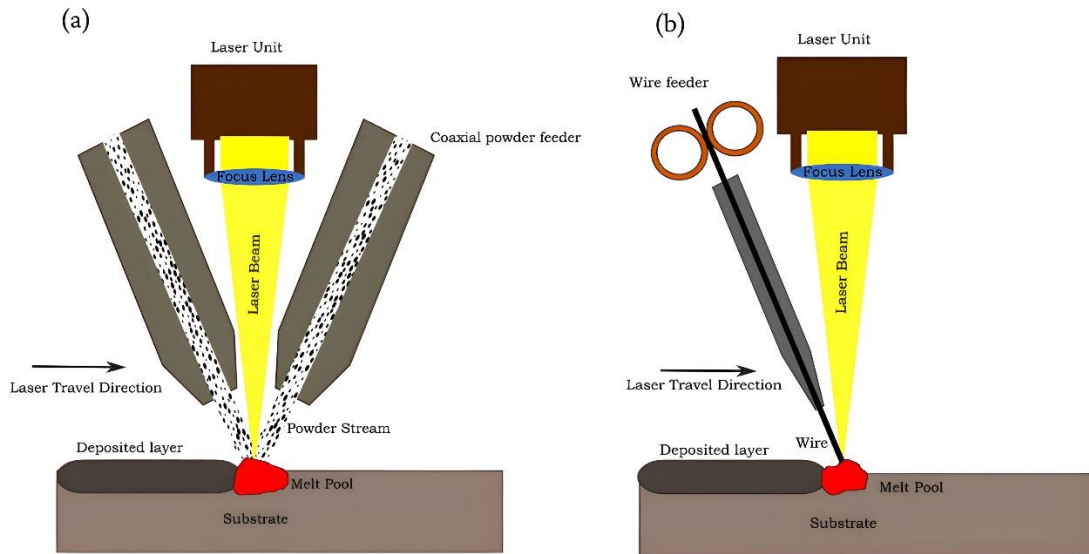


Figure 1.7 (a) Powder-based and (b) wire-based DED setups.

A powder feeder and a laser are used in the laser additive manufacturing (LAM)–DED process [67]. Wire-based DED techniques can be classified into wire arc additive manufacturing (WAAM), wire laser additive manufacturing (WLAM), and wire electron beam additive manufacturing (WEAM), with the primary difference being the thermal energy source used to melt the wire [68–70]. WAAM uses an electric arc, WLAM uses a laser source, and WEAM uses an electron beam for melting the wire [69,70]. Various factors affect the quality of parts in DED technology. These include the type of heat source, beam size, feedstock type, feed rate, machine parameters, layer thickness, etc. (Figure 1.8). DED provides many key advantages, including a high material deposition rate and the ability to produce bigger parts (several meters

in size) [71].

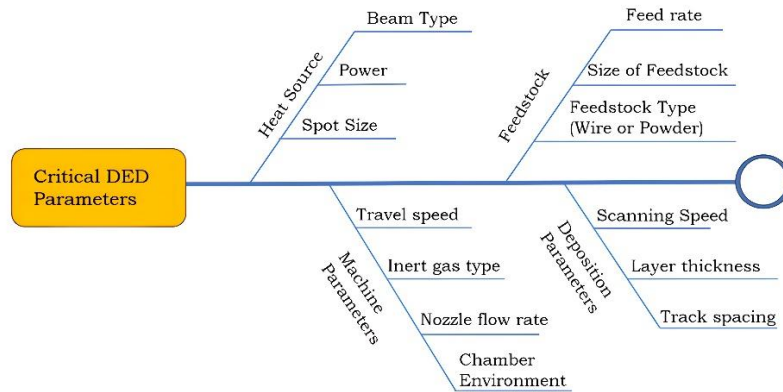


Figure 1.8 Critical parameters in direct energy deposition.

DED has been extensively used to produce multi-metal components in various research works [72,73]. It has been used to manufacture multimaterial structures made of Ti-alloys [74], Fe–Ni alloys [75–78], Co alloys [79], Cr alloys [80], steels [81,82] and Al-alloys [83–85]. During the fabrication of multimaterial structures, sudden transitions between material types tend to create issues. Rapid shifts in material types can pose challenges during the production of structures that use multimaterials. Issues such as the creation of fragile intermetallic phases [86], cracking during solidification [86], and elevated residual stresses due to differences in thermal expansion caused by material mismatch [87] can arise at the interfaces between materials. The problems caused by dissimilar metal bonding have been mitigated using gradient transitions between different materials, thereby forming functionally graded materials (FGMs) [88,89]. FGMs alleviate the problem of residual stresses; however, they fail to mitigate brittle intermetallic formation [76]. The technique of introducing an interfacial material at the joint of dissimilar materials has been successfully used in research to suppress intermetallic formation [90,91]. As compared to PBF, DED-manufactured parts have a coarser resolution but much bigger

achievable part sizes. This leads to inefficiency in producing intricate geometries, including lattice structures which are mostly used in industry [92]. It is difficult to manufacture small-scale multimaterial lattice unit cells in this process due to the lower level of accuracy, higher surface roughness, and larger surface waviness. The process also has a lower powder recyclability and efficiency when printing a mixture of powders as compared to PBF [93]. There have been many works on multimaterial printing using DED using a wide range of alloys [94-126]. This has been represented in figure 1.9.

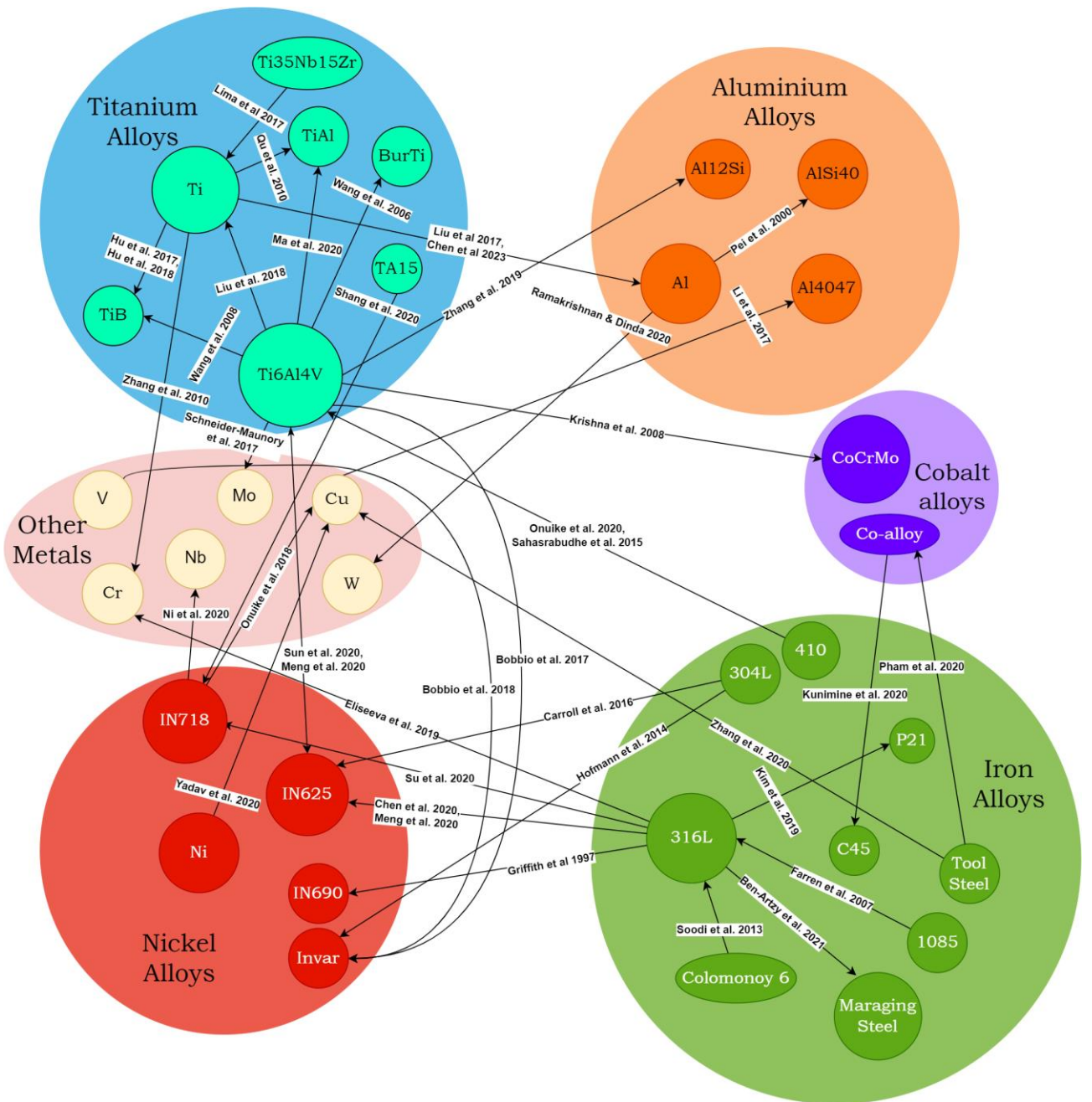


Figure 1.9 Multimaterial combinations fabricated using DED in research. The direction of arrows shows the order of fabrication (Information obtained from references [49, 76, 79, 82, 83, 85-87, 91, 94-126]).

1.3.1.3 Polymer AM and Multimaterial Fabrication

Multimaterial manufacturing has also been tested using polymer AM techniques, like stereolithography (SLA), fused filament fabrication (FFF), direct ink writing (DIW), and PolyJet, either individually or in a combined process. SLA was the first technology in this field, using multiple vats of photopolymers to achieve its objective [127, 128,129]. However, this approach requires a high process time [128]. Shortly afterwards, FFF, a widely used material extrusion-based technique using thermoplastic feedstock filaments, was employed for multimaterial applications by using multiple extrusion heads or nozzles [130,131]. Recently, DIW, which uses a viscoelastic ink solution using extruders, has been developed with three different apparatus modifications for multimaterial fabrication [132]. They include a single-cartridge system using a multimaterial ink with only one nozzle [133], a multi-cartridge system with different pastes and nozzles [134], and a concentric nozzle system with distinct filaments on core and shells [135]. A diverse array of polymers have also been considered in these studies. They include monomers; thermoplastic polymers like polyactic acid (PLA), acrylonitrile butadiene styrene (ABS), thermoplastic polyurethane (TPE), nylon, polycarbonate (PC), polycaprolactone (PCL), polyethylene terephthalate (PET) polyethylene glycol diacrylate (PEGDA), and high-impact polystyrene (HIPS); thermosetting polymers like silicones resins; and other materials like piezoelectrics, etc. (Table 1.3).

These processes can produce structures with multi-color regions or textures as well as spatial property variations including functional gradients. Mobilizing thermoplastic polymer chains through chemical reactions poses significant challenges, unlike thermoset plastics [136]. The prevalent use of thermoplastic polymers in hot-melt extrusion-based systems has propelled their expansion in research fields. This includes investigating the affinity between dissimilar

materials and studying their mechanical properties in the production of various structures.

The critical component in polymer multimaterials is the interface established at the geometric boundary of discrete materials. This interface's characteristics depend on the properties and printing conditions of the involved materials [130]. Significant research analysing the relationship between printing parameters and the multimaterial interface is scarce in polymer AM. Thus, the field remains a potential area of investigation for future work. Other challenges include the precise alignment of various extrusion heads during multimaterial deposition as well the intermittent stoppage of plastic in one extrusion system while another material is being deposited, leading to a rheology change in the plastic and difficulties in flow rate optimization [137].

Table 1.3 Different material combinations in polymer AM.

Researcher	Materials Used	Reference
<i>Stereolithography</i>		
Unkovskiy et al.	Silicones	[138]
Hu et al.	Monomers, PEGDA	[139]
Lu et al.	PET, Embedded piezoelectrics	[140]
Jiang et al.	Different resins	[141]
<i>Fused Filament Fabrication</i>		
Mansouri et al.	TPU, Bayblend	[142]
Yazdani et al.	Nylon, Carbon fibre	[143]
Lopes et al.	PLA, PET, TPU	[144]
Peng et al.	ABS, PE	
Yin et al.	ABS, TPU	[145]
Lin et al.	PLA, PCL	[146]
Mueller et al.	PET, PC	[147]
Khondoker et al.	PLA, ABS, HIPS	[148]
Ribeiro et al.	PLA, TPU	[149]
Khatri et al.	ABS, TPU	[150]
Singh et al.	ABS, HIPS	[151]
Mustafa et al.	ASA, PETG	[152]
Singh et al.	PLA, ABS, HIPS	[153]

Baca et al.	PLA, ABS, HIPS	[154]
<i>Direct Ink Writing</i>		
Yirmibesoglu et al.	Elastomers	[155]
Rocha et al.	Graphene electrodes	[134]

1.3.2 Conventional Manufacturing Techniques and Multimaterial Fabrication

Conventional manufacturing (CM) techniques have been employed in the literature to fabricate multimaterial parts. Several CM processes, like casting, forging, and machining, as well as joining methods, like welding and riveting, have been used to produce such structures (Figure 1.10) [156,157]. These methods are very different than AM processes due to their shaping methodologies, utilizing both additive and subtractive approaches of manufacturing. In this section, we explore the multimaterial fabrication capabilities of these methods and juxtapose each of them with additive manufacturing (AM) processes.

1.3.2.1 Casting

As one of the oldest CM techniques, casting processes produce near-net-shaped parts by filling a hollow mould of the required shape with molten metal and subsequently cooling it. It is still a widely used manufacturing technique due to its affordability in producing a large number of identical parts [158]. Multimaterial part casting has been performed in the literature using the in-mould assembly technique [159]. Casting is one of the few CM techniques with the potential to produce multimaterial parts without jointing methods like rivets, adhesives, welds, or fasteners. It was first proposed by Miller to manufacture a single cast made from two different metals [160]. Gouker et al. reviewed techniques for multimaterial moulding, including cavity transfer, removable core, and sliding core techniques, and successfully used mould piece combinations to fabricate multimaterial parts [161]. Recently, there has been particular interest

in producing aluminium–steel bimetallic cast parts in the literature with and without the use of coatings [162–164].

As compared to AM methods, this process is generally more affordable in producing large batch sizes of identical parts. Metal casting processes almost always require the removal of feed and filling systems from the output parts. However, parts manufactured by AM are generally closer to the final part shape with better levels of dimensional accuracy, surface finish, and customizability in terms of complexity and porosity.

1.3.2.2 Joining Processes

Joining processes are the primary CM methods used to join or fuse structures of different materials to fabricate multimaterial parts. Welding, a common permanent joining process, has been widely explored to fabricate multimaterial components [165]. Various welding techniques have been employed for manufacturing such components [166–168]. In particular, laser welding has several advantages, such as a high energy density and a high cooling rate with a smaller heat-affected zone [169,170]. Nevertheless, solid-state welding processes like friction and diffusion welding are better at suppressing holes and intermetallic compounds (IMCs) to generate better values of bond strength [166–168,171].

A simpler approach to joining different materials is a mechanical assembly operation. This includes processes like press fitting, shrink fitting, and even mechanical connections. Taniguchi et al. successfully used press fitting to assemble constituent parts of a bimaterial gear [172]. Shrink fitting has also been employed in research to assemble bimaterial parts [173,174].

Despite recent progress in manufacturing techniques, joining processes are still ubiquitous. AM processes are almost always more expensive than joining two components of different materials.

However, in the case of multimaterial complex structures with intricate joints like lattices and

gyroids, joining processes are not feasible. A similar argument exists for functionally graded multimaterial structures that have a gradual change in composition, which makes conventional joining processes redundant. Nonetheless, due to their ease of use, cost effectiveness, and versatility for simple components, these processes are widely employed in industry.

1.3.2.3 Forging

Forging is a manufacturing process that shapes metal using localized compressive forces to achieve the desired structure, size, and properties. These processes, broadly categorized as “hot forging”, “warm forging”, or “cold forging” have been used to produce multimaterial components [175–178]. Aluminium–steel combinations have been explored in existing studies, revealing the optimal processing conditions, with steel requiring temperatures above 900 °C and aluminium within the range of 400–500 °C. This ensures that the aluminium does not melt, and it allows for the assessment of the impact of varying values of the CTE of the two materials on their relative shrinkage [175]. Forging also has minimal feedstock waste, thereby reducing costs as compared to subtractive CM processes like machining.

In contrast to AM processes, forging has the advantage of producing larger objects more efficiently at a lower cost. The physical deformation involved in forging eliminates voids, making defects less of a concern for the mechanical performance of forged components compared to AM parts, which often exhibit some degree of porosity post-fabrication [179]. While specialized forging dies can be designed for intricate products, forging generally struggles with complex shapes. It is almost impossible to fabricate intricate designs like lattice-based structures which are generally required for metamaterials using forging. AM processes tend to perform better for relatively complex parts at a smaller production volume.

1.3.2.4 Machining

Machining is a subtractive manufacturing process in which a material is removed from feedstock to obtain the required shape. Currently, computer numeric control (CNC) machining is mainly used due to the high precision obtained from automation [180]. CNC machining can process a wide variety of materials, including metals, polymers, ceramics, composites, and many more. Due to the inherent subtractive nature of the process, the production of multimaterial parts generally requires the feedstock itself to be made of different materials. The multimaterial feedstock can be produced using casting, forging, or other techniques. Machining can then remove excess materials and impart the desired shape to the part.

Machining has a very prominent place in the manufacturing industry. When compared to AM, it is generally faster for not-too-complex parts at a higher volume of production. It also tends to consume comparatively less energy, although it is highly dependent on the shape and complexity of the part being manufactured. For example, the production of an aeronautical turbine using milling requires only 6 h as compared to around 16 h per part using PBF [181]. The feedstock used in machining is almost five to ten times less expensive than the metal powders used in metal AM [182]. Nonetheless, unlike metal AM, machining by itself is unable to produce multimaterial parts and requires multimaterial feedstock to be fed. Hence, it cannot be called a fully multimaterial manufacturing process. However, metal AM, as discussed before, can generate fully multimaterial products using single-material feedstocks or powders. Additionally, it is relatively easier to manufacture complex repeating-unit cell structures like lattices using metal AM, particularly PBF as compared to CNC machining [182].

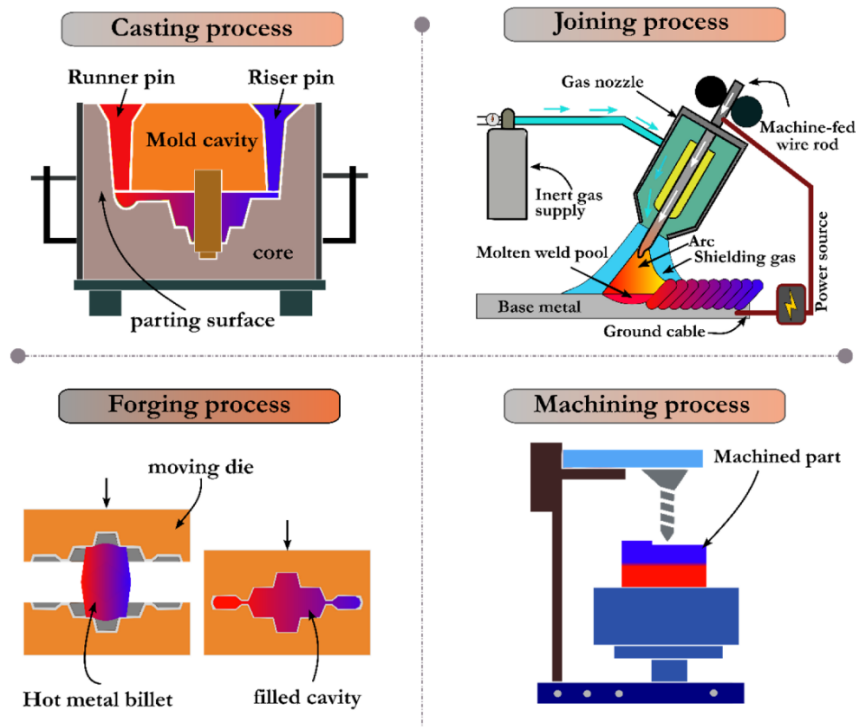


Figure 1.10 Schematic diagrams of various CM processes (Reprinted with permission from [179]; Copyright 2020 Hasanov et al.).

1.3.3 Comparison of Microstructural Properties in AM and CM Processes

In addition to the differences outlined in the preceding section, the variation in physical processes employed during production results in distinct mechanical and microstructural properties of the final parts produced through AM and CM processes. For instance, the interaction of a laser with the metallic powder in LPBF causes the formation of a tiny melt pool roughly 1 mm in length and 0.5 mm in width and depth [183,184]. Depending on various parameters, cooling rates can reach values as high as 10^3 – 10^8 K/s [185,186]. Based on the solidification theory for microstructure formation, grain nucleation begins at the solid–liquid interface between the base metal and melt pool [187,188]. Due to rapid solidification, homogeneous nucleation cannot take place because it usually requires a bigger time scale.

Therefore, heterogeneous nucleation and epitaxial grain growth take place in LPBF with a columnar solidification front [189,190]. The final microstructure is primarily dependent on the temperature gradient at the solid–liquid interface and solidification rate. The process generally induces extremely fine microstructures in alloys like steels leading to high values of mechanical strength and hardness in the resultant parts [191,192]. Nevertheless, the selection of optimum process parameters is crucial in LPBF; otherwise, defects like holes, inclusions, and warping can easily occur and deteriorate mechanical properties [193,194]. In his work on the Inconel 625 alloy, Marchese et al. observed that DED also provides a fine microstructure; however, it is around one order of magnitude larger than LPBF [195]. It has a multi-scale non-homogeneous microstructure with columnar grains; however, the characteristic sizes exceed those in LPBF [196,197]. It leads to surface hardness and mechanical strength values that are lower than those of parts made using LPBF, but they are higher than identical parts made of wrought alloys [198]. In addition to the dependence on processing parameters, the grains observed in DED also vary with the specimen's geometry and locations within it [196,199]. Additionally, due to the differential grain flow in resultant microstructures, both LPBF and DED parts tend to show anisotropic behaviour in terms of mechanical properties [200,201].

Conventionally manufactured parts have different microstructural and mechanical properties due to differing temperature and cooling rates than AM fabricated parts. Casting can have cooling rates of 5–100 K/s, which are well below those in LPBF [202,203]. The microstructure consists of columnar elongated grains near the mould walls as opposed to equiaxed uniform grains near the core of the casting [204]. Quicker cooling promotes faster solidification, leading to finer microstructures and enhanced mechanical properties, while slower cooling leads to

larger grain sizes and coarser microstructures [205,206]. However, cooling rates cannot be increased to very high values like those in AM processes because faster cooling rates can also lead to increased shrinkage and non-uniform solidification and cause voids in the final part [207]. Forging tends to elongate grains as well as defects like voids and inclusions in the direction of metal flow or plastic deformation [208]. This produces anisotropy in parts; however, the grain flow can improve properties like toughness and ductility if the crack propagation direction and grain flow directions are aligned [209]. Hot forging at high temperatures and cooling rates can also produce finer grain microstructures, thereby improving mechanical strength [210]. In fusion welding, the microstructure of the joint is predominantly determined by the filler metal's chemical composition and the amount of heat applied. A higher heat input results in a slower cooling rate, leading to larger grains, while a lower heat input speeds up cooling, producing a finer microstructure [211]. It has been observed that friction stir welding, a solid-state process, is better for hard metals like steel and titanium due to the control it provides for composition and temperature, thereby providing superior values of joint strength [212]. It directly helps to tune the microstructure and mechanical action in the form of stirring, modifying the microstructure from coarse grains to finer ones [213,214]. While in most traditional manufacturing techniques, the microstructure mainly depends on temperature history, severe plastic deformation during cutting also plays an important role in the resultant microstructure of machined parts [215]. The cutting parameters, like the depth of cut, feed rate, and cutting speed, play a huge role in microstructure development. In many works, these parameters have also been linked to phase transformation near the surface of machined parts [216–218]. The difference between AM and CM microstructures is shown in Figure 1.11 [219].

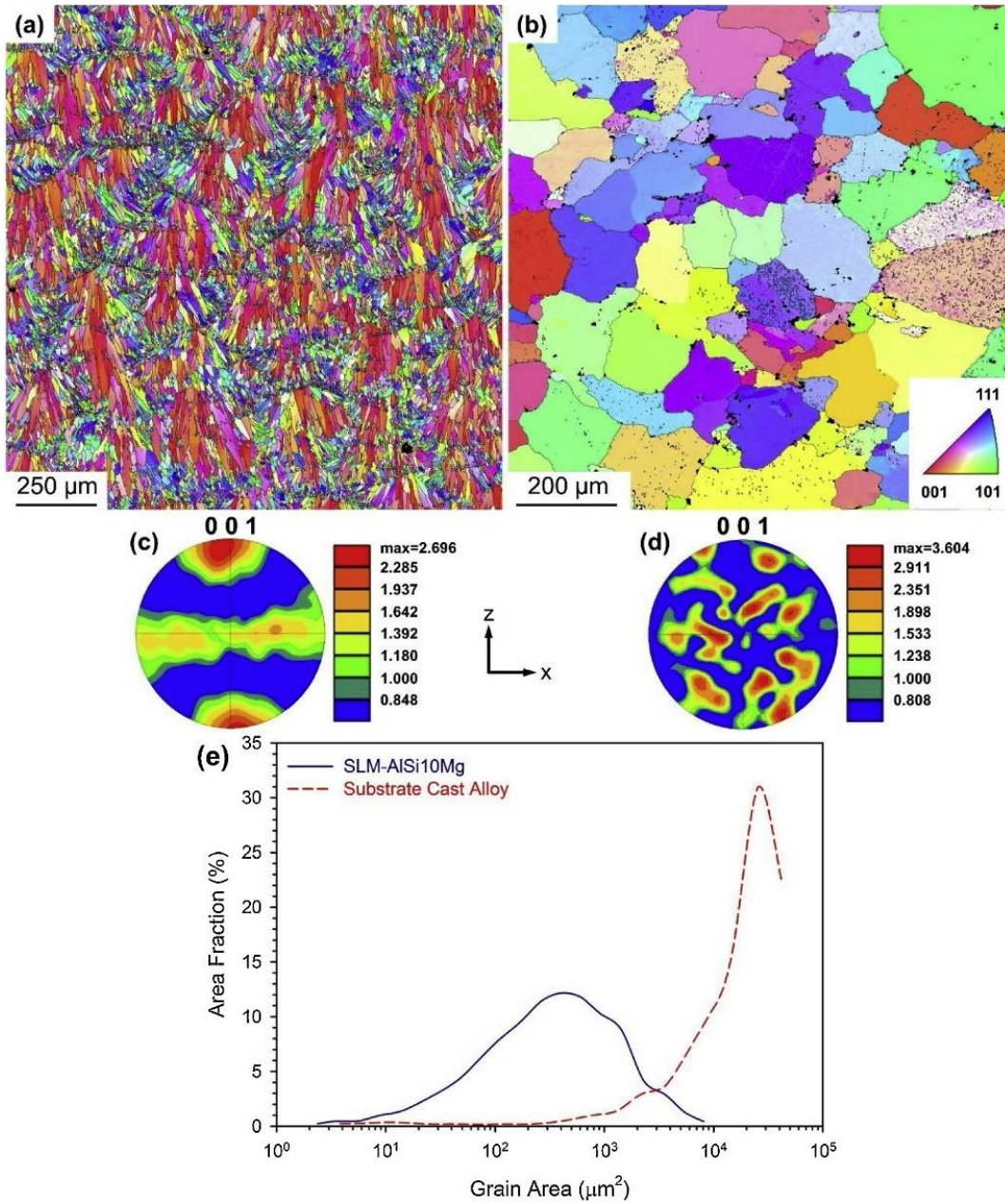


Figure 1.11 Electron backscatter diffraction (EBSD) maps of (a) LPBF-AlSi10Mg and (b) cast aluminium alloy. EBSD pole figures of (c) LPBF-AlSi10Mg and (d) cast aluminium alloy; (e) grain size area in LPBF-AlSi10Mg and the cast alloy (Reprinted with permission from [219]; Copyright 2020 Elsevier).

Clearly, these investigations establish a significant contrast in the microstructural development

and mechanical characteristics of parts produced through AM and CM fabrication. The exceptionally elevated temperatures and rapid cooling associated with AM techniques tend to yield extremely fine microstructures characterized by enhanced strength, toughness, and hardness values. In contrast, different CM methods exhibit varying cooling rates, which are generally lower than those of AM processes. This results in a diverse array of possible microstructures through CM procedures, which are contingent upon the specific process and parameters employed.

1.3.4 Material Selection for NTE Architectures

Although a multimaterial combination is necessary for NTE, this is not sufficient in itself to produce a functional NTE structure. Along with the design, an NTE metamaterial also requires the following:

1. A considerable difference in the CTE of the constituents;
2. A strong interface between different materials.

In most designs, the expansion of one material counteracts the expansion of the other to produce an overall NTE. For example, in a bimaterial strip, the material that is expanding less causes the one that is expanding more to bend, thereby leading to the shortening of the strip [12]. A high difference between the CTE values is ideal for a better NTE performance. In addition, the less-expanding material should ideally have as low a CTE value as possible for a better performance. The research conducted by Ai et al. demonstrated that all four of their NTE designs exhibited significantly lower CTE values when utilizing aluminium–invar combinations compared to steel–invar combinations, primarily due to a higher CTE difference. Conversely, the aluminium–steel combination resulted in even higher CTE values and, in some designs, an

overall positive thermal expansion [26]. This outcome can be attributed to the smaller CTE difference between aluminium and steel, coupled with the fact that steel, as a material with lower expansion in the design, inherently possesses a higher CTE value than invar. Similar results were obtained by Wei et al. in their works using different combinations of Al, steel, and invar [22]. Undoubtedly, the variation in NTE performance would be contingent on the specific design under consideration as well. Additionally, the change in CTE values for various materials with temperature could influence the performance, especially at elevated temperatures [220].

The strength of the bond at the interface is another crucial requirement in NTE metamaterials. Phase equilibrium diagrams provide essential information about stable phases under various temperatures and metallic element combinations and aid in exploring the compatibility of two metals or alloys [221]. They are helpful to evaluate the feasibility of the resultant interface strength of dissimilar alloys in different CM joining processes like welding as well as heating-based AM techniques like LPBF or DED. Not every alloy combination with a difference in CTE values and hence potential NTE fabrication capability can provide enough bond strength to the resultant interface. For instance, during the LPBF process of pure aluminium (Al) onto pure iron (Fe), an initial layer of Al powder is deposited onto the previously printed Fe. During the laser-powder interaction, not only the pure Al powder but also a portion of the solid Fe beneath it must melt to prevent cracks or a lack of fusion porosities at the Al/Fe interface. Consequently, the molten pure Al becomes diluted by Fe, and the proportion of Fe in the liquid Al depends on factors like the process parameters and powder layer thickness. Assuming 50 wt% Al and 50 wt% Fe at the interface, according to the equilibrium binary phase diagram of Fe–Al, this composition lies between the FeAl_2 and Fe_2Al_5 phase zones, resulting in a microstructure

consisting of these two phases at room temperature (Figure 1.12). As the 3D printing progresses, the Fe concentration in subsequent Al layers decreases. Layers 2 to 5 might have decreasing Fe concentrations of 30, 20, 10, and 0 wt%, respectively, leading to microstructures comprising FeAl₃ (layer 2), (Al) + FeAl₃ (layers 3 and 4), and (Al). These intermetallics (FeAl₂, Fe₂Al₅, and FeAl₃) are known to be hard and brittle [222].

The LPBF process generates thermal stresses/strains that these brittle phases cannot withstand, resulting in material cracking from the interface during printing. This illustrates why Al and Fe are considered incompatible and cannot be directly printed on top of each other. The same considerations apply to printing Al-based alloys on Fe-based alloys. This phenomenon of the non-satisfactory bonding of Al–Fe from phase diagrams has already been experimentally verified in other CM joining techniques, like various welding processes and roll bonding during the joining of aluminium and iron alloys [223–226]. Therefore, it is important to identify metal or alloy combinations without intermetallics or at least avoid brittle intermetallics in their phase diagrams for compatibility in different architectures.

Al-Fe

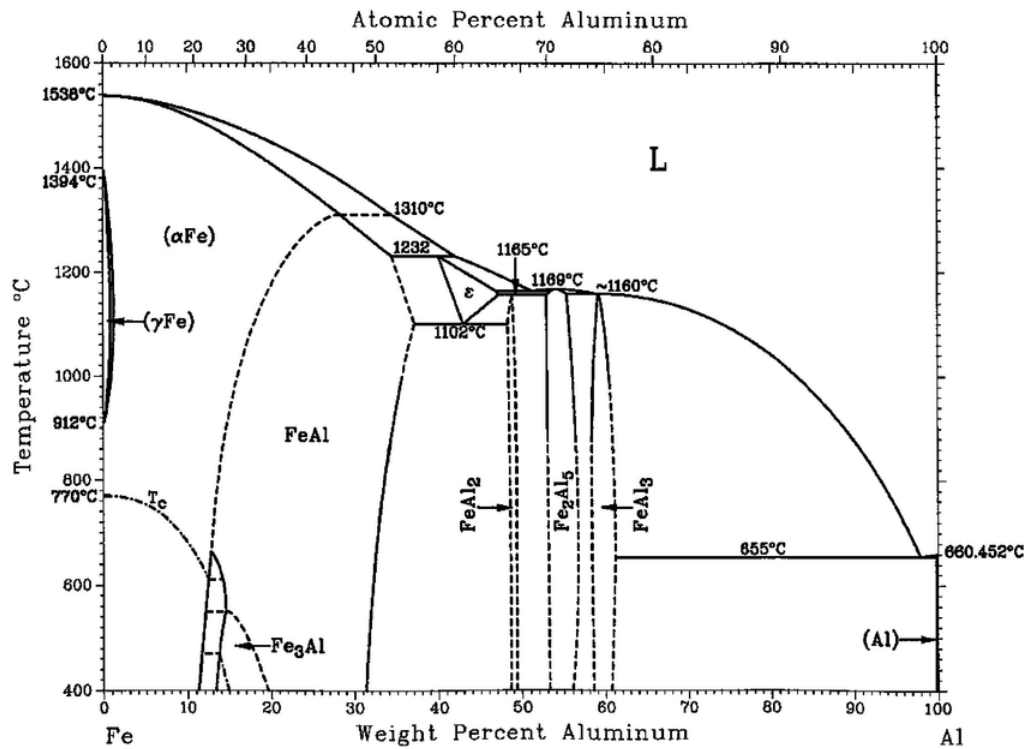


Figure 1.12 The iron–aluminium phase diagram (Reprinted with permission from [227]; Copyright 1990 ASM International).

On the other hand, metals like nickel (Ni) and copper (Cu) are compatible according to phase diagrams [227]. The equilibrium binary phase diagram of Ni–Cu is shown in Figure 1.13. As evident, no intermetallics are present in the Ni–Cu phase diagram, and these two metals can dissolve in one another at any concentration. Therefore, they are compatible and can be printed using AM processes on top of each other without any issues and even be joined using conventional joining processes like welding.

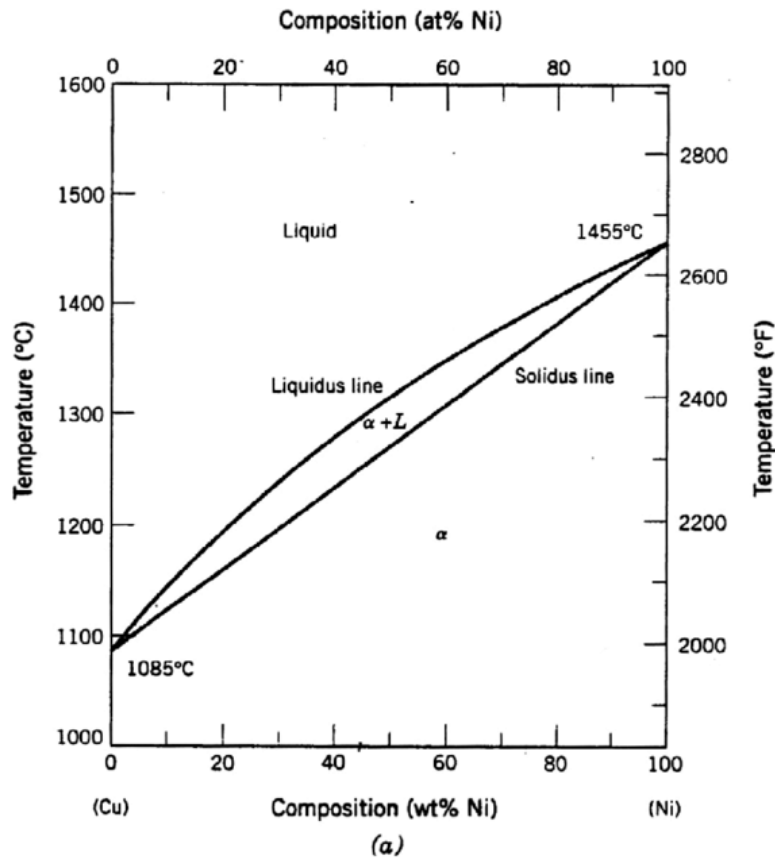


Figure 1.13 The copper–nickel phase diagram (Reprinted with permission from [227]; Copyright 1990 ASM International).

Nevertheless, in non-fusion joining processes like assemblies using bonding glues or riveting, this issue would not exist; however, careful attention is needed to evaluate the strength of such joints using other applicable parameters and experiments. Thus, CTE differences and material compatibility are very important requirements for the fabrication of NTE metamaterials.

1.4 Prospective Applications

Negative-thermal-expansion materials are in high demand for high-precision applications undergoing temperature changes. In such applications, even a minuscule dimensional change due to the expansion of their constituents can cause significant levels of inaccuracy. The

combination of negative expansion structures with positive expansion materials has the potential to produce zero thermal expansion overall, leading to a high dimensional accuracy and mitigating errors in such applications. Some of these applications include the following [228–230]:

- Electronic packaging;
- Fuel cells;
- Dental implants;
- Space structures.

The sub-sections below discuss these applications in detail.

1.4.1 Electronic Packaging

Electronic packaging refers to the design and fabrication of enclosures for electronic devices. It is a promising application for negative- and low-expansion thermal metamaterials due to the requirement of a low CTE value for packaging constituents. For optimal thermal management, the packaging material must have the following key attributes [231]:

- High thermal conductivity (TC) to minimize thermal resistance and increase heat dissipation.
- Low CTE to minimize thermal expansion mismatches and enhance thermal cycling performance.
- High manufacturability at the micro-level.
- High mechanical strength to support and stabilize fine microstructures at high operational pressures.

In packaging, it is vital to closely match the coefficients of thermal expansion of substrate materials to those of semiconductors, like gallium nitride and silicon carbide to avoid issues

caused by CTE mismatch (Figure 1.14).

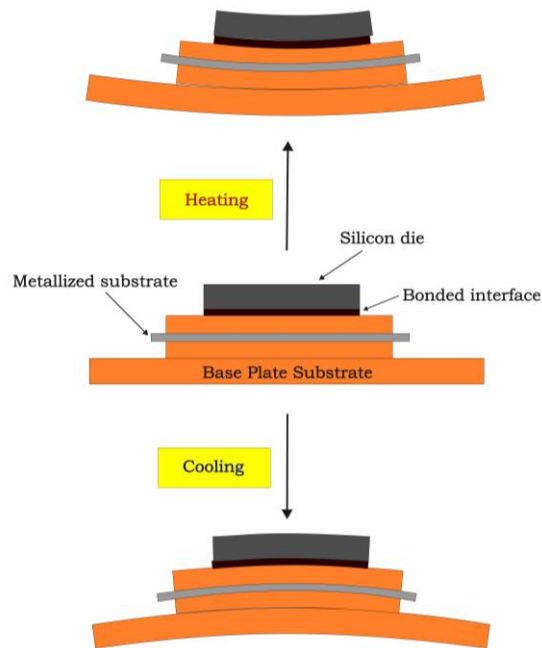


Figure 1.14 CTE mismatch in electronic packaging.

In order to have superior levels of heat dissipation, the substrates are also required to have high thermal conductivity values. Based on their composition, electronic packaging materials can be categorized into ceramic, plastic, and metal materials. The advantages and limitations of each are mentioned in Table 1.4.

Table 1.4 Material types used in electronic packaging.

Type of Packaging Material	Advantages	Limitations	References
Ceramic	Low CTE, low density	Low TC	[232,233]
Plastic	Small size, light weight, high impact resistance	Low TC caused by internal voids, easily corroded	[234,235]
Metal	High TC	High CTE leading to increased thermal stresses	[236,237]

A graph comparing the coefficients of the CTE values of various substrates and semiconductors

is shown in figure 1.15.

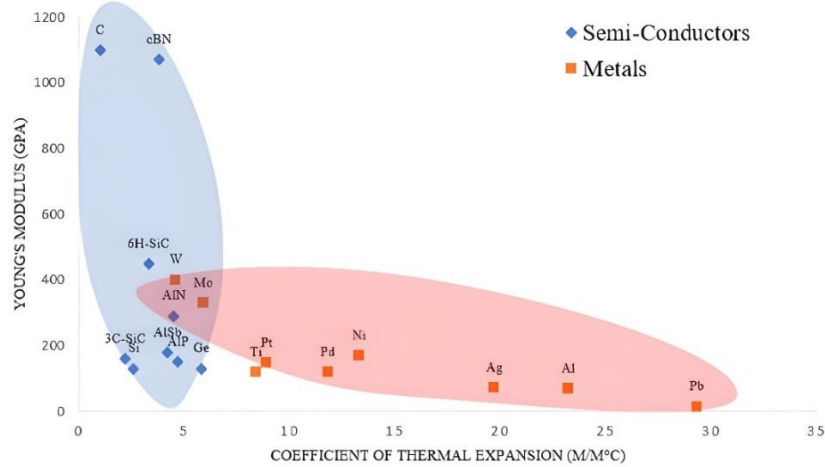


Figure 1.15 Young's modulus and thermal expansion coefficient of semi-conductors and metals (data obtained from [238–240]).

Unlike conventional substrates like plastics and polymers, metal substrates are particularly useful in high-temperature applications requiring higher thermal conductivity values since metals tend to have higher thermal conductivity values. Recently, thermal metamaterials have been considered for electronic packaging applications [241]. The various characteristics of thermal metamaterials' development relevant to electronic packaging applications are as follows:

- Anisotropic heat dissipation to minimize hot spots [242];
- Heat cloaking of thermally sensitive electronic components [243];
- Heat guiding in a defined path to reduce thermal interference between adjacent devices [244].

While previous research has focused mostly on inherent material properties, the architectural

property of the negative thermal expansion of thermal metamaterials can be combined with the abovementioned characteristics to reduce thermal mismatch and further increase the application of metamaterials in the electronic packaging industry.

1.4.2 Fuel Cells

Fuel cells are electrochemical conversion devices used to generate electrical energy from chemical potential (figure 1.16) [245]. Their low emission levels, silent operation, and environmentally friendly byproducts have generated interest in using them as potential replacements for fossil fuels in various applications. A summary is provided in Table 1.5.

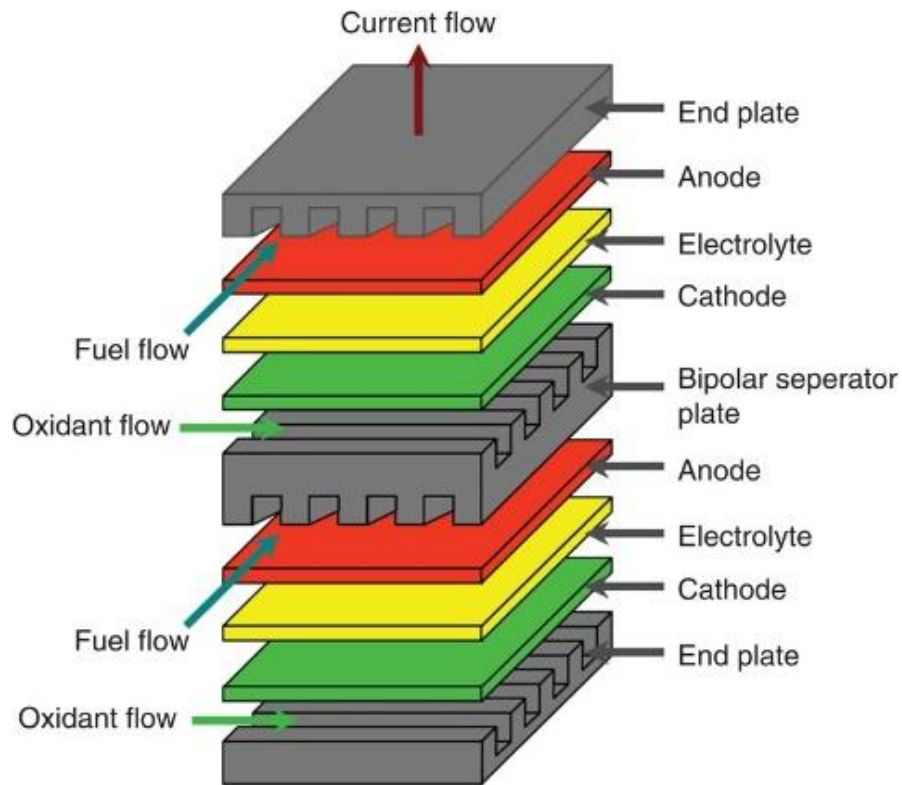


Figure 1.16 Design of fuel cell (Reprinted with permission from [245]; Copyright 2013 John Wiley and sons).

Table 1.5 Different types of fuel cells, their properties, and applications.

Type of Fuel Cell	Common Electrolyte	Operating Temperature	Efficiency	Applications	References
Proton Exchange Membrane (PEM)	Perfluoro sulfonic acid	50–100 °C	60%	Portable power, automobiles, backup power	[246]
Alkaline (AFC)	Aqueous potassium hydroxide in a matrix	90–100 °C	60%	Military, space	[247]
Phosphoric Acid (PAFC)	Phosphoric acid in a matrix	150–200 °C	40%	Distributed generation	[248]
Molten Carbonate (MCFC)	Lithium, sodium and/or potassium carbonates	600–700 °C	45–50%	Distributed generation	[249]
Solid Oxide (SOFC)	Ytria stabilized zirconia	700–1000 °C	60%	Auxiliary power, Electric utility, Distributed generation	[250,251]
Microbial Fuel Cell	Microbes	Ambient temperature	50%	Carbon capture, Wastewater treatment, Biowaste energy recovery	[252,253]

One of the emerging fuel cell types is the solid oxide fuel cell (SOFC) due to its high efficiency and diverse fuel alternatives, like carbon-based fuels. Solid oxide fuel cells (SOFCs), also known as high-temperature fuel cells, operate within the temperature range of 650°C to 1000°C. They use an oxygen ion conducting solid inorganic ceramic electrolyte, allowing for the utilization of a wide range of fuels. However, a significant issue with this technology is its incapacity to sustain intermittent operation. Any period of cessation and reactivation is harmful to the cell and can take several hours. One of the primary factors contributing to this problem is the varying CTE between its various components, like the electrodes, electrolyte, and

interconnect materials [254-263]. A brief overview of these CTE values is shown in Table 1.6 [264].

Table 1.6. CTE values of SOFC components (Reprinted with permission from [264]; Copyright 2020 Elsevier).

Anode	CTE ($\times 10^{-6}$ K $^{-1}$)	Electrolyte	CTE ($\times 10^{-6}$ K $^{-1}$)	Cathode	CTE ($\times 10^{-6}$ K $^{-1}$)	Inter-connect	CTE ($\times 10^{-6}$ K $^{-1}$)	Seals	CTE ($\times 10^{-6}$ K $^{-1}$)
Ni-YSZ	12.2 [254]	YSZ	12.9	LSM	11.7 [255]	LaCrO ₃	9.7 [256, 257]	Ag-Cuo	15.0 [258]
LST	10.8 [259]	-	-	LSF	16.3 [260]	-	-	Soda glass	9.0 [261]
SLC	8.6–11.5	-	-	LSC	20.5 [260]	-	-	-	
				LSCF	16.3 [260]				
				LSMF	19.3 [262]				
				SSC	19.9 [263]				
				PSM	11.6 [260]				

Thus, thermo-mechanical instability is an important obstacle in commercial fuel cell development. The difference in the thermal expansion of various components causes high internal stresses and strains, leading to reduced durability, delamination issues, and overall higher degradation rates [267]. One of the components which suffers the most from such problems is the cathode in solid oxide fuel cells (SOFCs). Highly conductive cobalt containing perovskites, which are generally used for manufacturing due to their high oxygen reduction activity, exhibits a much higher CTE value ($\sim 20\text{--}25 \times 10^{-6}/\text{K}$) as compared to its SOFC electrolyte counterparts ($\sim 11.2\text{--}12.3 \times 10^{-6}/\text{K}$). It leads to high thermal stresses and hence frequent degradation. Techniques are utilised including doping transition metals with d^0 orbitals, making composites of perovskite material with electrolyte material, incorporating A-site deficiencies in cathodes, and introducing thermal-expansion-restricting phases [268–271]. Zhang et al. came up with the novel approach of combining an NTE material, Y₂W₃O₁₂ oxide

(CTE $\sim -7 \times 10^{-6}/\text{K}$), with a Perovskite electrode material, $\text{SrNb}_{0.1}\text{Co}_{0.9}\text{O}_{3-\delta}$ (also called SNC, CTE $\sim 21 \times 10^{-6}$), which had a great electrochemical performance [267]. In another work, Jia et al. combined $\text{Sm}_{0.85}\text{Zn}_{0.15}\text{MnO}_3$ material exhibiting NTE with a $\text{Ba}_{0.5}\text{Sr}_{0.5}\text{Fe}_{0.8}\text{Cu}_{0.1}\text{Ti}_{0.1}\text{O}_{3-\delta}$ (BSFCT) cathode [272]. Instead of electrodes, Hayun et al. focused on altering the electrolyte's CTE by adding tungsten oxide (WO_3) powder to 8YSZ powder, which was sintered to form a tungsten-based multi-phased Ytria-stabilized zirconia (YSZ) ceramic electrolyte [266]. It has improved levels of thermal shock resistance and has the potential to reduce the problem of the lack of rapid restart in SOFCs. These multimaterial combinations show that combining different types of materials to mitigate thermal expansion issues is an emerging technique in the fuel cell industry to solve the problem of mismatch in thermal expansion. This idea is similar to the multi-material combination approach used in NTE metamaterials.

However, along with electrodes and electrolytes, the optimization of interconnects in SOFCs is also very important in fuel cells. Interconnects function as the linking components that connect the current collectors in various cells or electrical loads. The primary types of interconnects developed are (i) ceramic-based [271] and (ii) metal-based [272]. Due to the high cost and low electrical conductivity of oxide-based ceramic interconnects, recent progress has focused on metal-based interconnects. The thermal and chemical requirements of interconnect materials include the following [273]:

- Their CTE values should be similar to those of other SOFC components;
- High levels of thermal and electrical conductivity;
- High levels of mechanical strength at high temperatures;
- Chemical stability in both oxidizing and reducing environments;

- Excellent imperviousness to oxygen and hydrogen.

Metallic interconnects can be used at temperatures up to 800°C as compared to ceramic interconnects that can be used near 1000°C. Metallic interconnects have low material and production costs, can be easily shaped due to their high malleability, and exhibit high levels of thermal and electrical conductivity. However, they generally need protective oxide surface coatings against corrosion [274]. Ferritic stainless steels with high amounts of chromium have been extensively used due to the formation of a protective Cr_2O_3 layer at higher temperatures. Nonetheless, when exposed to elevated temperatures, chromium tends to vaporize and deposit at the cathode surface of the SOFC, thereby decreasing the life of the SOFC [272,275]. Alternative alloys with Al or Si that can create protective oxide layers like Al_2O_3 or SiO_2 are typically avoided because of their slow oxide layer development and the reason that chromium oxide (Cr_2O_3) functions as a semiconductor within the temperature range of the SOFC, therefore offering superior levels of conductivity compared to those of Al_2O_3 and SiO_2 , which are electrically insulating oxides [276,277]. Nickel-based superalloys (Haynes 230, Haynes 242, Hastelloy S) offer better oxidation behaviour under the SOFC temperature range than ferritic steels like Crofer22 APU, which are commonly used SOFCs. In addition, they do not suffer from the issue of chromium evaporation, unlike ferritic steels. However, at present, nickel-based superalloys are not used in SOFCs due to their higher CTE values relative to those of other SOFC components. Additionally, in the case of Haynes 242, its CTE behaviour is non-linear [278].

NTE metamaterials, as discussed in this paper, can be used to design artificial architectures in SOFCs' interconnect design to regulate their CTE. This has the potential to make the material

level CTE requirement less important and simultaneously avoid thermal stress development in SOFCs, thereby allowing researchers to use higher-CTE materials, like nickel superalloys, which offer better oxidation resistance without the chromium poisoning of the cathode.

1.4.3 Dental Implants

Dental implants are widely used these days to replace tooth loss caused by periodontitis, trauma, or genetic disorders [279]. Their ability to integrate with bone, also called osseointegration, gives them an edge over conventional replacements like dentures or bridges [280]. Also, dental implants are standalone tooth replacements and are not attached to other teeth.

As depicted in Figure 1.17, the structure of a dental implant consists of the following [281]:

- Crown;
- Abutment;
- Implant body (or implant)

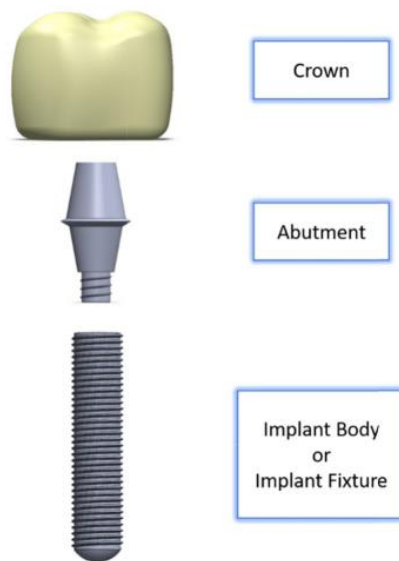


Figure 1.17 Structure of a general dental implant (Reprinted with permission from [281]; Copyright 2022 Elsevier).

Different types of materials have been tested for making implants. The ideal material is required to be chemically biocompatible with a fairly high mechanical strength, excellent corrosion resistance, and high wear resistance [281]. Titanium and its alloy Ti6Al4V have been widely used to manufacture these implants due to their excellent biocompatibility, lower density than that of most steels, and corrosion resistance due to the formation of oxide film TiO₂ as well as good osseointegration [282]. However, despite their advantages, these implants suffer from various issues.

- Titanium implants have a much higher Young's modulus (~120 GPa) than a typical human bone (~1 to 20 GPa). This results in the stress shielding of bone because most of the applied stress is loaded onto the implant. It can lead to lower than normal levels of stress on the surrounding bone, leading to less bone regeneration in that region and hence weaker surrounding bones over time, i.e., bone loss. This can cause the loosening of implants [283,284].
- The thermal conductivity of titanium implants is much higher than that of the human teeth they replace [285,286]. During the consumption of hot food and beverages, human teeth or dental implants undergo cyclic thermal loads. However, enamel and dentin layers in actual human teeth have low thermal conductivity, thereby protecting the sensitive inner pulp and bone inside gums from these temperature changes. However, this is not the case when dental implants are in use. These high food temperatures when transferred to alveolar bones in gums can cause permanent bone-death, also called necrosis, and the loss of bone regeneration and osseointegration. Necrosis can result from a thermal shock of 47°C over just a minute [287,288], which can be easily caused by the excellent thermal conductivity

of metal dental implants combined with intra-oral temperatures easily reaching 67–77 °C during day-to-day hot beverage consumption [289].

- Despite their biocompatibility advantages, titanium and its alloys tend to be more expensive than other implant alloy options like stainless steel [290].

NTE metamaterials have the potential to be used for dental implant applications:

- The problem of the high thermal conductivity of titanium implants can be alleviated by designing them with lattices, as used in mechanical metamaterials. Due to the porosity of lattices, the average thermal conductivity would be lower than that of a fully dense solid metal cross-section of the same size.
- The inner core of implant roots can be made of steel with a titanium covering on the outside if a negative- or low-expansion metamaterial lattice structure for a steel core is used. The low CTE of the lattice metamaterial structure would mitigate the problem of the high expansion of steels as compared to the CTE of human bone. Also, the overall cost of implants would decrease due to the lower use of titanium.

1.4.4 Space Structures

The fluctuating temperatures in outer space make space structures undergo thermal expansion and contraction [291]. A satellite's orbit and design, among other things, can have an impact on the severe temperature conditions that exist in space. Spacecraft materials and structures are subjected to temperatures ranging from roughly –180 °C to +180 °C during different orbital phases around Earth (Figure 1.18) [292]. The materials experience thermal stresses as a result of these large temperature swings, which total a 360 °C change. Differential coefficients of thermal expansion can cause issues, such as surface treatments and electronic components

flaking off, as well as diminished adhesion and cracking. Other missions, such as those that investigate extra-terrestrial worlds, which may experience extended temperature ranges as well as extremely cold or high temperatures, must also consider similar concerns. Therefore, achieving almost net-zero thermal expansion is necessary for sensitive large-scale space structures, like telescopes and reflector antennas, to maintain their spatial resolution and accuracy [293,294].

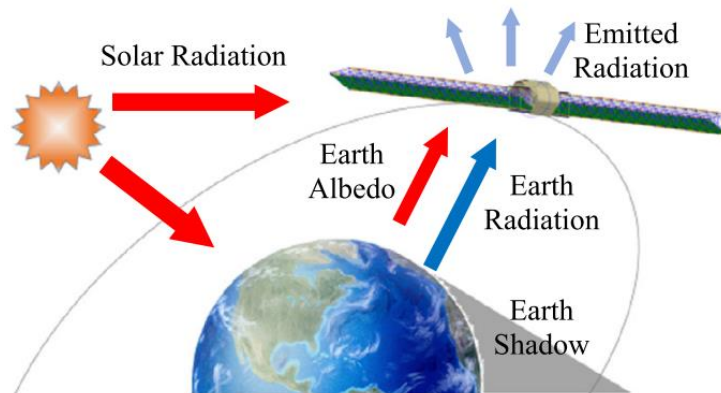


Figure 1.18 Fluctuating thermal environment in Earth's orbit (Reprinted with permission from [295]; Copyright 2023 Yu et al., Licensee MDPI).

Recently, thermomechanical metamaterials with tailorable low-thermal-expansion properties have garnered interest in controlling thermal expansion in space structures. Yu et al. designed two near-zero thermal expansion lattice structures using structural optimization with a negligible thermal expansion of 10^{-9} m/m.K, achieving almost zero thermal deformation. The structure also had the potential to be fabricated in orbit using additive manufacturing (Figure 1.19) [295]. In another work, a negative-CTE lattice structure was designed for a high-precision optical system that could be manufactured using metal additive manufacturing using invar and titanium (Figure 1.20) [296]. These works make a strong case for the usage of NTE metamaterials in

space to mitigate thermal mismatches in various components as well as overall structure.

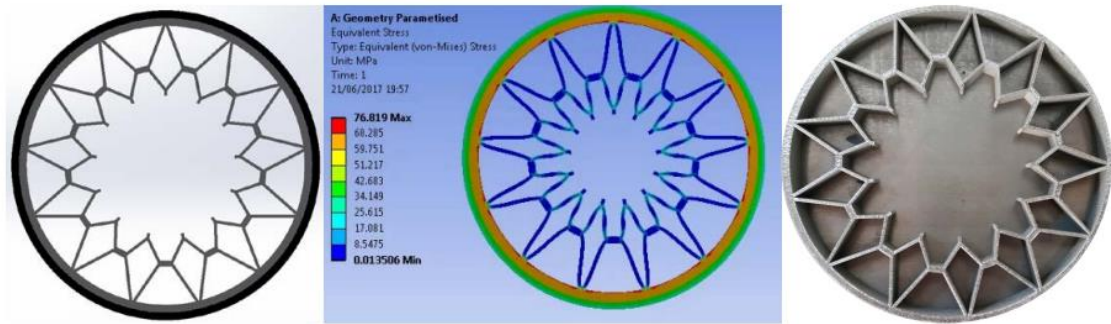


Figure 1.19 Negative expansion design by Milward et al. for cylindrical lens system meant for space applications (Reprinted with permission from [296]; Copyright 2017 Milward et al.).

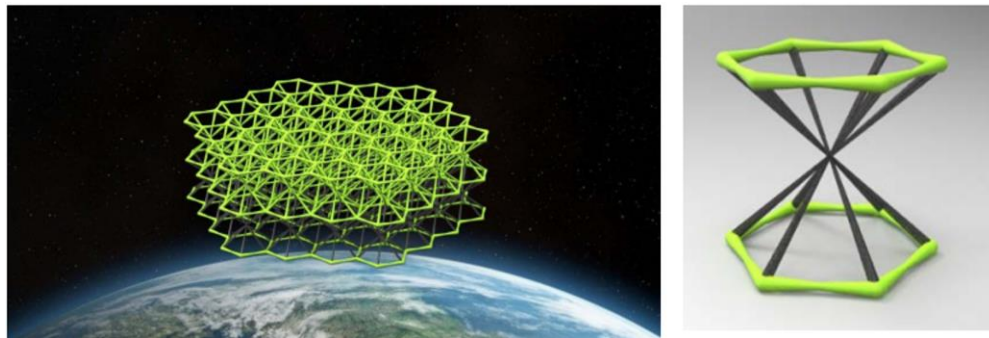


Figure 1.20 Bimaterial hourglass hexagonal negative expansion design by Yu et al. (Reprinted with permission from [295]; Copyright 2023 Yu et al., Licensee MDPI).

1.5 Conclusions

In this paper, we delved into the thriving research within the NTE metamaterials field, which has seen significant growth over the past decade. Various researchers have created numerous designs, both theoretical and experimental. Based on these findings, we can formulate the following conclusions:

- The difference between constituents directly affects the NTE performance of the design

along with the CTE of lower-thermal-expansion materials. A higher difference and a lower CTE of a low-expansion material tend to decrease the overall NTE. This is a general trend with the actual performance increase varying between different architectures.

- NTE designs have been manufactured using both AM and CM processes. In contrast to traditional manufacturing techniques, AM processes can create multimetal structures in a single machine with intricate details.
- The production of these structures has been explored using both polymers and metals. Fabrication using polymers offers the advantage of creating a greater difference in CTE between constituents, as some polymers have inherently higher CTE values than metals. On the other hand, metals provided greater stiffness values to the designs because of their higher strengths.
- The properties of multimaterial structures vary depending on the processes used in their production. AM techniques, characterized by rapid cooling rates, typically yield microstructures with fine grains and high strengths. In contrast, subtractive manufacturing CM methods exhibit lower cooling rates, resulting in coarser microstructures and other distinct differences.
- Achieving strong interfacial bonds is essential when constructing practical NTE systems. In processes that involve the application of heat to join diverse materials, the bond strength relies on the miscibility of the constituents and the formation of intermediate compounds. The use of equilibrium phase diagrams plays a crucial role in understanding the resultant bond strengths in combinations of multiple materials.
- Finally, we explored the diverse applications of NTE architectures across a range of fields,

including biomedicine and energy production, highlighting their versatility and the specific needs.

In summary, the ability to produce thermally tuned structures is a key milestone in solving the problem of mismatched thermal expansion without sacrificing mechanical strength. To achieve this, future research works are required to mainly focus on three attributes: (a) material-to-material bonding compatibility; (b) metamaterial design-to-manufacturing process compatibility; and (c) application-specific metamaterial design. Further investigations are necessary in the domain of NTE metamaterials for their successful design, production, and application. Furthermore, with the rise of AM, the utilization of metals in the creation of designs is promising, and manufacturing methods emerge as promising approaches for crafting NTE architectures with metal components. The key factor contributing to this potential is the capability of these processes to fabricate multimaterial structures with high strength values and customizable properties. PBF and DED are suitable AM techniques to produce these structures, making this a promising avenue for future research

References

1. Takenaka, K. Progress of research in negative thermal expansion materials: Paradigm shift in the control of thermal expansion. *Front. Chem.* **2018**, *6*, 267. <https://doi.org/10.3389/fchem.2018.00267>.
2. Takenaka, K. Negative thermal expansion materials: Technological key for control of thermal expansion. *Sci. Technol. Adv. Mater.* **2012**, *13*, 13001. <https://doi.org/10.1088/1468-6996/13/1/013001>.
3. Devoto, D.; Paret, P.; Narumanchi S.; Mihalic M. Reliability of Bonded Interfaces for Automotive Power Electronics. 2013. In Proceedings of the ASME 2013 International Technical Conference and Exhibition on Packaging and Integration of Electronic and Photonic Microsystems. Volume 1: Advanced Packaging; Emerging Technologies; Modeling and Simulation; Multi-Physics Based Reliability; MEMS and NEMS; Materials and Processes. Burlingame, California, USA. July 16–18, 2013. <https://doi.org/10.1115/IPACK2013-73143>
4. Chen, J.; Hu, L.; Deng, J.; Xing, X. Negative thermal expansion in functional materials: Controllable thermal expansion by chemical modifications. *Chem. Soc. Rev.* **2015**, *44*, 3522–3567. <https://doi.org/10.1039/c4cs00461b>.
5. J. S. O. Evans, “Negative thermal expansion materials †,” *Journal of the Chemical Society, Dalton Transactions*, no. 19, pp. 3317–3326, 1999, doi: 10.1039/A904297K.
6. Chu, C.N.; Saka, N.; Suh, N.P. Negative thermal expansion ceramics: A review. *Mater. Sci. Eng.* **1987**, *95*, 303–308. [https://doi.org/10.1016/0025-5416\(87\)90523-4](https://doi.org/10.1016/0025-5416(87)90523-4).

7. Mary, T.A.; Evans, J.S.O.; Vogt, T.; Sleight, A.W. Negative Thermal Expansion from 0.3 to 1050 Kelvin in ZrW₂O₈. *Science* **1996**, *272*, 90–92. <https://doi.org/10.1126/science.272.5258.90>.
8. Takenaka, K.; Takagi, H. Giant negative thermal expansion in Ge-doped anti-perovskite manganese nitrides. *Appl. Phys. Lett.* **2005**, *87*, 261902. <https://doi.org/10.1063/1.2147726>.
9. Greve, B.K.; Martin, K.L.; Lee, P.L.; Chupas, P.J.; Chapman, K.W.; Wilkinson, A.P. Pronounced negative thermal expansion from a simple structure: Cubic ScF₃. *J. Am. Chem. Soc.* **2010**, *132*, 15496–15498. <https://doi.org/10.1021/ja106711v>.
10. Evans, J.S.O.; Mary, T.A.; Sleight, A.W. Negative Thermal Expansion in a Large Molybdate and Tungstate Family. *J. Solid State Chem.* **1997**, *133*, 580–583. <https://doi.org/10.1006/jssc.1997.7605>.
11. Chapman, K.W.; Chupas, P.J.; Kepert, C.J. Compositional Dependence of Negative Thermal Expansion in the Prussian Blue Analogues MIIIPtIV(CN)₆ (M = Mn, Fe, Co, Ni, Cu, Zn, Cd). *J. Am. Chem. Soc.* **2006**, *128*, 7009–7014. <https://doi.org/10.1021/ja060916r>.
12. Lakes, R. Cellular solid structures with unbounded thermal expansion. *J. Mater. Sci. Lett.* **1996**, *15*, 475–477.
13. Lakes, R. Cellular solids with tunable positive or negative thermal expansion of unbounded magnitude. *Appl. Phys. Lett.* **2007**, *90*, 221905. <https://doi.org/10.1063/1.2743951>.
14. Lehman, J.; Lakes, R. Stiff lattices with zero thermal expansion. *J. Intell. Mater. Syst. Struct.* **2012**, *23*, 1263–1268. <https://doi.org/10.1177/1045389X12445647>.
15. Lehman, J.; Lakes, R. Stiff, strong zero thermal expansion lattices via the Poisson effect. *J. Mater. Res.* **2013**, *28*, 2499–2508. <https://doi.org/10.1557/jmr.2013.154>.

16. Ha, C.S.; Hestekin, E.; Li, J.; Plesha, M.E.; Lakes, R.S. Controllable thermal expansion of large magnitude in chiral negative Poisson's ratio lattices. *Phys. Status Solidi B Basic Res.* **2015**, *252*, 1431–1434. <https://doi.org/10.1002/pssb.201552158>.
17. Grima, J.N.; Farrugia, P.S.; Gatt, R.; Zammit, V. A system with adjustable positive or negative thermal expansion. *Proc. R. Soc. A Math. Phys. Eng. Sci.* **2007**, *463*, 1585–1596. <https://doi.org/10.1098/rspa.2007.1841>.
18. Grima, J.N.; Bajada, M.; Scerri, S.; Attard, D.; Dudek, K.K.; Gatt, R. Maximizing negative thermal expansion via rigid unit modes: A geometry-based approach. *Proc. R. Soc. A Math. Phys. Eng. Sci.* **2015**, *471*, 20150188. <https://doi.org/10.1098/rspa.2015.0188>.
19. Grima, J.N.; Oliveri, L.; Ellul, B.; Gatt, R.; Attard, D.; Cicala, G.; Recca, G. Adjustable and negative thermal expansion from multilayered systems. *Phys. Status Solidi Rapid Res. Lett.* **2010**, *4*, 133–135. <https://doi.org/10.1002/pssr.201004076>.
20. Wu, L.; Li, B.; Zhou, J. Isotropic Negative Thermal Expansion Metamaterials. *ACS Appl. Mater. Interfaces* **2016**, *8*, 17721–17727. <https://doi.org/10.1021/acsami.6b05717>.
21. Steeves, C.A.; Lucato, S.L.D.S.E.; He, M.; Antinucci, E.; Hutchinson, J.W.; Evans, A.G. Concepts for structurally robust materials that combine low thermal expansion with high stiffness. *J. Mech. Phys. Solids* **2007**, *55*, 1803–1822. <https://doi.org/10.1016/j.jmps.2007.02.009>.
22. Wei, K.; Chen, H.; Pei, Y.; Fang, D. Planar lattices with tailorable coefficient of thermal expansion and high stiffness based on dual-material triangle unit. *J. Mech. Phys. Solids* **2016**, *86*, 173–191. <https://doi.org/10.1016/j.jmps.2015.10.004>.

23. Li, Y.; Chen, Y.; Li, T.; Cao, S.; Wang, L. Hoberman-sphere-inspired lattice metamaterials with tunable negative thermal expansion. *Compos. Struct.* **2018**, *189*, 586–597. <https://doi.org/10.1016/j.compstruct.2018.01.108>.
24. Jefferson, G.; Parthasarathy, T.A.; Kerans, R.J. Tailorable thermal expansion hybrid structures. *Int. J. Solids Struct.* **2009**, *46*, 2372–2387. <https://doi.org/10.1016/j.ijsolstr.2009.01.023>.
25. Ai, L.; Gao, X.L. Three-dimensional metamaterials with a negative Poisson's ratio and a non-positive coefficient of thermal expansion. *Int. J. Mech. Sci.* **2018**, *135*, 101–113. <https://doi.org/10.1016/j.ijmecsci.2017.10.042>.
26. Ai, L.; Gao, X.L. Metamaterials with negative Poisson's ratio and non-positive thermal expansion. *Compos. Struct.* **2017**, *162*, 70–84. <https://doi.org/10.1016/j.compstruct.2016.11.056>.
27. Raminhos, J.S.; Borges, J.P.; Velhinho, A. Development of polymeric anepectic meshes: Auxetic metamaterials with negative thermal expansion. *Smart Mater. Struct.* **2019**, *28*, 45010. <https://doi.org/10.1088/1361-665X/ab034b>.
28. Lim, T.C. Auxetic and Negative Thermal Expansion Structure Based on Interconnected Array of Rings and Sliding Rods. *Phys. Status Solidi B Basic Res.* **2017**, *254*, 1600775. <https://doi.org/10.1002/pssb.201600775>.
29. Lim, T.C. Negative thermal expansion structures constructed from positive thermal expansion trusses. *J. Mater. Sci.* **2012**, *47*, 368–373. <https://doi.org/10.1007/s10853-011-5806-z>.

30. Xu, H.; Pasini, D. Structurally efficient three-dimensional metamaterials with controllable thermal expansion. *Sci. Rep.* **2016**, *6*, 34924. <https://doi.org/10.1038/srep34924>.
31. Xu, H.; Farag, A.; Pasini, D. Routes to program thermal expansion in three-dimensional lattice metamaterials built from tetrahedral building blocks. *J. Mech. Phys. Solids* **2018**, *117*, 54–87. <https://doi.org/10.1016/j.jmps.2018.04.012>.
32. Jin, Z.H. A microlattice material with negative or zero thermal expansion. *Compos. Commun.* **2017**, *6*, 48–51. <https://doi.org/10.1016/j.coco.2017.08.005>.
33. Juasiripukdee, P.; Maskery, I.; Ashcroft, I.; Leach, R. Low thermal expansion machine frame designs using lattice structures. *Appl. Sci.* **2021**, *11*, 9135. <https://doi.org/10.3390/app11199135>.
34. Peng, X.L.; Bargmann, S. Tunable auxeticity and isotropic negative thermal expansion in three-dimensional lattice structures of cubic symmetry. *Extreme Mech. Lett.* **2021**, *43*, 101201. <https://doi.org/10.1016/j.eml.2021.101201>.
35. Peng, X.L.; Bargmann, S. A novel hybrid-honeycomb structure: Enhanced stiffness, tunable auxeticity and negative thermal expansion. *Int. J. Mech. Sci.* **2021**, *190*, 106021. <https://doi.org/10.1016/j.ijmecsci.2020.106021>.
36. Ha, C.S.; Plesha, M.E.; Lakes, R.S. Simulations of thermoelastic triangular cell lattices with bonded joints by finite element analysis. *Extrem. Mech. Lett.* **2017**, *12*, 101–107. <https://doi.org/10.1016/j.eml.2016.10.013>.
37. Lim, T.-C. Anisotropic and negative thermal expansion behavior in a cellular microstructure. *J. Mater. Sci.* **2005**, *40*, 3275–3277. <https://doi.org/10.1007/s10853-005-2700-6>.

38. Deshpande, V.S.; Ashby, M.F.; Fleck, N.A. Foam topology: Bending versus stretching dominated architectures. *Acta Mater.* **2001**, *49*, 1035–1040. [https://doi.org/10.1016/S1359-6454\(00\)00379-7](https://doi.org/10.1016/S1359-6454(00)00379-7).
39. Thompson, S.M.; Bian, L.; Shamsaei, N.; Yadollahi, A. An overview of Direct Laser Deposition for additive manufacturing; Part I: Transport phenomena, modeling and diagnostics. *Addit. Manuf.* **2015**, *8*, 36–62. <https://doi.org/10.1016/j.addma.2015.07.001>.
40. Pereira, T.; Kennedy, J.V.; Potgieter, J. A comparison of traditional manufacturing vs additive manufacturing, the best method for the job. In *Procedia Manufacturing*; Elsevier B.V.: Amsterdam, The Netherlands, 2019; pp. 11–18. <https://doi.org/10.1016/j.promfg.2019.02.003>.
41. Ding, X.; Wang, L. Heat transfer and fluid flow of molten pool during selective laser melting of AlSi10Mg powder: Simulation and experiment. *J. Manuf. Process.* **2017**, *26*, 280–289. <https://doi.org/10.1016/j.jmapro.2017.02.009>.
42. Zhang, B.; Li, Y.; Bai, Q. Defect Formation Mechanisms in Selective Laser Melting: A Review. *Chin. J. Mech. Eng. Engl. Ed.* **2017**, *30*, 515–527. <https://doi.org/10.1007/s10033-017-0121-5>.
43. Cao, L. Mesoscopic-scale numerical investigation including the influence of scanning strategy on selective laser melting process. *Comput. Mater. Sci.* **2021**, *189*, 110263. <https://doi.org/10.1016/j.commatsci.2020.110263>.
44. Chen, K.; Wang, C.; Hong, Q.; Wen, S.; Zhou, Y.; Yan, C.; Shi, Y. Selective laser melting 316L/CuSn10 multi-materials: Processing optimization, interfacial characterization and

- mechanical property. *J. Mater. Process. Technol.* **2020**, 283, 116701.
<https://doi.org/10.1016/j.jmatprotec.2020.116701>.
45. Mei, X.; Wang, X.; Peng, Y.; Gu, H.; Zhong, G.; Yang, S. Interfacial characterization and mechanical properties of 316L stainless steel/inconel 718 manufactured by selective laser melting. *Mater. Sci. Eng. A* **2019**, 758, 185–191.
<https://doi.org/10.1016/j.msea.2019.05.011>.
46. Chen, J.; Yang, Y.; Song, C.; Zhang, M.; Wu, S.; Wang, D. Interfacial microstructure and mechanical properties of 316L /CuSn10 multi-material bimetallic structure fabricated by selective laser melting. *Mater. Sci. Eng. A* **2019**, 752, 75–85.
<https://doi.org/10.1016/j.msea.2019.02.097>.
47. Sing, S.L.; Lam, L.P.; Zhang, D.Q.; Liu, Z.H.; Chua, C.K. Interfacial characterization of SLM parts in multi-material processing: Intermetallic phase formation between AlSi10Mg and C18400 copper alloy. *Mater. Charact.* **2015**, 107, 220–227.
<https://doi.org/10.1016/j.matchar.2015.07.007>.
48. Liu, Z.H.; Zhang, D.Q.; Sing, S.L.; Chua, C.K.; Loh, L.E. Interfacial characterization of SLM parts in multi-material processing: Metallurgical diffusion between 316L stainless steel and C18400 copper alloy. *Mater. Charact.* **2014**, 94, 116–125.
<https://doi.org/10.1016/j.matchar.2014.05.001>.
49. Tan, C.; Zhou, K.; Ma, W.; Min, L. Interfacial characteristic and mechanical performance of maraging steel-copper functional bimetal produced by selective laser melting based hybrid manufacture. *Mater. Des.* **2018**, 155, 77–85.
<https://doi.org/10.1016/j.matdes.2018.05.064>.

50. Thijs, L.; Verhaeghe, F.; Craeghs, T.; Van Humbeeck, J.; Kruth, J.-P. A study of the microstructural evolution during selective laser melting of Ti-6Al-4V. *Acta Mater.* **2010**, *58*, 3303–3312. <https://doi.org/10.1016/j.actamat.2010.02.004>.
51. Anwar, A.B.; Pham, Q.-C. Study of the spatter distribution on the powder bed during selective laser melting. *Addit. Manuf.* **2018**, *22*, 86–97. <https://doi.org/10.1016/j.addma.2018.04.036>.
52. Kasperovich, G.; Haubrich, J.; Gussone, J.; Requena, G. Correlation between porosity and processing parameters in TiAl6V4 produced by selective laser melting. *Mater. Des.* **2016**, *105*, 160–170. <https://doi.org/10.1016/j.matdes.2016.05.070>.
53. King, W.E.; Barth, H.; Castillo, V.; Gallegos, G.; Gibbs, J.; Hahn, D.; Kamath, C.; Rubenchik, A. Observation of keyhole-mode laser melting in laser powder-bed fusion additive manufacturing. *J. Mater. Process. Technol.* **2014**, *214*, 2915–2925. <https://doi.org/10.1016/j.jmatprotec.2014.06.005>.
54. Zhang, M.; Yang, Y.; Wang, D.; Song, C.; Chen, J. Microstructure and mechanical properties of CuSn/18Ni300 bimetallic porous structures manufactured by selective laser melting. *Mater. Des.* **2019**, *165*, 107583. <https://doi.org/10.1016/j.matdes.2019.107583>.
55. Shakerin, S.; Hadadzadeh, A.; Amirkhiz, B.S.; Shamsdini, S.; Li, J.; Mohammadi, M. Additive manufacturing of maraging steel-H13 bimetals using laser powder bed fusion technique. *Addit. Manuf.* **2019**, *29*, 100797. <https://doi.org/10.1016/j.addma.2019.100797>.
56. Tan, C.; Zhang, X.; Dong, D.; Attard, B.; Wang, D.; Kuang, M.; Ma, W.; Zhou, K. In-situ synthesised interlayer enhances bonding strength in additively manufactured multi-material

- hybrid tooling. *Int. J. Mach. Tools Manuf.* **2020**, 155, 103592. <https://doi.org/10.1016/j.ijmachtools.2020.103592>.
57. Wang, P.; Lao, C.; Chen, Z.; Liu, Y.; Wang, H.; Wendrock, H.; Eckert, J.; Scudino, S. Microstructure and mechanical properties of Al-12Si and Al-3.5Cu-1.5Mg-1Si bimetal fabricated by selective laser melting. *J. Mater. Sci. Technol.* **2020**, 36, 18–26. <https://doi.org/10.1016/j.jmst.2019.03.047>.
58. Wei, K.; Zeng, X.; Li, F.; Liu, M.; Deng, J. Microstructure and Mechanical Property of Ti-5Al-2.5Sn/Ti-6Al-4V Dissimilar Titanium Alloys Integrally Fabricated by Selective Laser Melting. *JOM* **2020**, 72, 1031–1038. <https://doi.org/10.1007/s11837-019-03988-6>.
59. Tey, C.F.; Tan, X.; Sing, S.L.; Yeong, W.Y. Additive manufacturing of multiple materials by selective laser melting: Ti-alloy to stainless steel via a Cu-alloy interlayer. *Addit. Manuf.* **2020**, 31, 100970. <https://doi.org/10.1016/j.addma.2019.100970>.
60. Scaramuccia, M.G.; Demir, A.G.; Caprio, L.; Tassa, O.; Previtali, B. Development of processing strategies for multigraded selective laser melting of Ti6Al4V and IN718. *Powder Technol.* **2020**, 367, 376–389. <https://doi.org/10.1016/J.POWTEC.2020.04.010>.
61. Wei, C.; Li, L.; Zhang, X.; Chueh, Y.H. 3D printing of multiple metallic materials via modified selective laser melting. *CIRP Ann.* **2018**, 67, 245–248. <https://doi.org/10.1016/j.cirp.2018.04.096>.
62. Wei, C.; Liu, L.; Gu, Y.; Huang, Y.; Chen, Q.; Li, Z.; Li, L. Multi-material additive-manufacturing of tungsten–copper alloy bimetallic structure with a stainless-steel interlayer and associated bonding mechanisms. *Addit. Manuf.* **2022**, 50, 102574. <https://doi.org/10.1016/j.addma.2021.102574>.

63. Frazier, W.E. Metal additive manufacturing: A review. *J. Mater. Eng. Perform.* **2014**, 23, 1917–1928. <https://doi.org/10.1007/s11665-014-0958-z>.
64. Ahn, D.G. Direct metal additive manufacturing processes and their sustainable applications for green technology: A review. *Int. J. Precis. Eng. Manuf. Green Technol.* **2016**, 3, 381–395. <https://doi.org/10.1007/s40684-016-0048-9>.
65. Dass, A.; Moridi, A. State of the art in directed energy deposition: From additive manufacturing to materials design. *Coatings* **2019**, 9, 418. <https://doi.org/10.3390/COATINGS9070418>.
66. Ding, D.; Pan, Z.; Cuiuri, D.; Li, H. Wire-feed additive manufacturing of metal components: Technologies, developments and future interests. *Int. J. Adv. Manuf. Technol.* **2015**, 81, 465–481. <https://doi.org/10.1007/s00170-015-7077-3>.
67. Sibisi, T.H.; Shongwe, M.B.; Tshabalala, L.C.; Mathoho, I. LAM additive manufacturing: A fundamental review on mechanical properties, common defects, dominant processing variables, and its applications. *Int. J. Adv. Manuf. Technol.* **2023**, 128, 2847–2861. <https://doi.org/10.1007/s00170-023-12139-w>.
68. Williams, S.W.; Martina, F.; Addison, A.C.; Ding, J.; Pardal, G.; Colegrove, P. Wire + Arc additive manufacturing. *Mater. Sci. Technol.* **2016**, 32, 641–647. <https://doi.org/10.1179/1743284715Y.0000000073>.
69. Casalino, G.; Karamimoghadam, M.; Contuzzi, N. Metal Wire Additive Manufacturing: A Comparison between Arc Laser and Laser/Arc Heat Sources. *Inventions* **2023**, 8, 52. <https://doi.org/10.3390/inventions8020052>.

70. Osipovich, K.; Kalashnikov, K.; Chumaevskii, A.; Gurianov, D.; Kalashnikova, T.; Vorontsov, A.; Zykova, A.; Utyaganova, V.; Panfilov, A.; Nikolaeva, A.; Dobrovolskii, A.; Rubtsov, V.; Kolubaev, E. Wire-Feed Electron Beam Additive Manufacturing: A Review. *Metals* **2023**, *13*, 279. <https://doi.org/10.3390/met13020279>.
71. Feenstra, D.R.; Banerjee, R.; Fraser, H.L.; Huang, A.; Molotnikov, A.; Birbilis, N. Critical review of the state of the art in multi-material fabrication via directed energy deposition. *Curr. Opin. Solid State Mater. Sci.* **2021**, *25*, 100924. <https://doi.org/10.1016/j.cossms.2021.100924>.
72. Zhang, Y.; Bandyopadhyay, A. Direct fabrication of bimetallic Ti6Al4V+Al12Si structures via additive manufacturing. *Addit. Manuf.* **2019**, *29*, 100783. <https://doi.org/10.1016/j.addma.2019.100783>.
73. Thiriet, A.; Schneider-Maunoury, C.; Laheurte, P.; Boisselier, D.; Weiss, L. Multiscale study of different types of interface of a buffer material in powder-based directed energy deposition: Example of Ti6Al4V/Ti6Al4V—Mo/Mo—Inconel 718. *Addit. Manuf.* **2019**, *27*, 118–130. <https://doi.org/10.1016/j.addma.2019.02.007>.
74. Zhang, J.; Zhang, Y.; Li, W.; Karnati, S.; Liou, F.; Newkirk, J.W. Microstructure and properties of functionally graded materials Ti6Al4V/TiC fabricated by direct laser deposition. *Rapid Prototyp. J.* **2018**, *24*, 677–687. <https://doi.org/10.1108/RPJ-12-2016-0215>.
75. Li, X.C., J. Stampfl, and F.B. Prinz. 2000. Mechanical and Thermal Expansion Behavior of Laser Deposited Metal Matrix Composites of Invar and TiC. *Materials Science and Engineering: A* **2000**, 282, no. 1: 86–90. [https://doi.org/10.1016/S0921-5093\(99\)00781-9](https://doi.org/10.1016/S0921-5093(99)00781-9).

76. Bobbio, L.D.; Bocklund, B.; Otis, R.; Borgonia, J.; Dillon, R.; Shapiro, A.; McEnerney, B.; Liu, Z.; Beese, A. Experimental analysis and thermodynamic calculations of an additively manufactured functionally graded material of v to Invar 36. *J. Mater. Res.* **2018**, *33*, 1642–1649. <https://doi.org/10.1557/jmr.2018.92>.
77. Zuback, J.S.; Palmer, T.A.; DebRoy, T. Additive manufacturing of functionally graded transition joints between ferritic and austenitic alloys. *J. Alloys Compd.* **2019**, *770*, 995–1003. <https://doi.org/10.1016/j.jallcom.2018.08.197>.
78. Li, W.; Chen, X.; Yan, L.; Zhang, J.; Zhang, X.; Liou, F. Additive manufacturing of a new Fe-Cr-Ni alloy with gradually changing compositions with elemental powder mixes and thermodynamic calculation. *Int. J. Adv. Manuf. Technol.* **2018**, *95*, 1013–1023. <https://doi.org/10.1007/s00170-017-1302-1>.
79. Kunimine, T.; Miyazaki, R.; Yamashita, Y.; Funada, Y. Effects of Laser-Beam Defocus on Microstructural Features of Compositionally Graded WC/Co-Alloy Composites Additively Manufactured by Multi-Beam Laser Directed Energy Deposition. *Sci. Rep.* **2020**, *10*, 8975. <https://doi.org/10.1038/s41598-020-65429-8>.
80. Wang, X.; Zhang, Z.; Men, Y.; Li, X.; Liang, Y.; Ren, L. Fabrication of nano-TiC functional gradient wear-resistant composite coating on 40Cr gear steel using laser cladding under starved lubrication conditions. *Opt. Laser Technol.* **2020**, *126*, 106136. <https://doi.org/10.1016/j.optlastec.2020.106136>.
81. Lin, X.; Yue, T.M.; Yang, H.O.; Huang, W.D. Laser rapid forming of SS316L/Rene88DT graded material. *Mater. Sci. Eng. A* **2005**, *391*, 325–336. <https://doi.org/10.1016/j.msea.2004.08.072>.

82. Ben-Artzy, A.; Reichardt, A.; Borgonia, J.; Dillon, R.; McEnerney, B.; Shapiro, A.; Hosemann, P. Compositionally graded SS316 to C300 Maraging steel using additive manufacturing. *Mater. Des.* **2021**, *201*, 109500. <https://doi.org/10.1016/j.matdes.2021.109500>.
83. Ramakrishnan, A.; Dinda, G.P. Microstructural control of an Al–W aluminum matrix composite during direct laser metal deposition. *J. Alloys Compd.* **2020**, *813*, 152208. <https://doi.org/10.1016/j.jallcom.2019.152208>.
84. Li, J.C.; Lin, X.; Kang, N.; Lu, J.L.; Wang, Q.Z.; Huang, W.D. Microstructure, tensile and wear properties of a novel graded Al matrix composite prepared by direct energy deposition. *J. Alloys Compd.* **2020**, *826*, 154077. <https://doi.org/10.1016/j.jallcom.2020.154077>.
85. Pei, Y.T.; De Hosson, J.T.M. Functionally graded materials produced by laser cladding. *Acta Mater.* **2000**, *48*, 2617–2624. [https://doi.org/10.1016/S1359-6454\(00\)00065-3](https://doi.org/10.1016/S1359-6454(00)00065-3).
86. Chen, N.; Khan, H.; Wan, Z.; Lippert, J.; Sun, H.; Shang, S.; Liu, Z.; Li, J. Microstructural characteristics and crack formation in additively manufactured bimetal material of 316L stainless steel and Inconel 625. *Addit. Manuf.* **2020**, *32*, 101037. <https://doi.org/10.1016/j.addma.2020.101037>.
87. Zhang, X.; Sun, C.; Pan, T.; Flood, A.; Zhang, Y.; Li, L.; Liou, F. Additive manufacturing of copper—H13 tool steel bi-metallic structures via Ni-based multi-interlayer. *Addit. Manuf.* **2020**, *36*, 101474. <https://doi.org/10.1016/j.addma.2020.101474>.
88. Liu, W.; DuPont, J.N. Fabrication of functionally graded TiC/Ti composites by laser engineered net shaping. *Scr. Mater.* **2003**, *48*, 1337–1342. [https://doi.org/10.1016/S1359-6462\(03\)00020-4](https://doi.org/10.1016/S1359-6462(03)00020-4).

89. Feenstra, D.R.; Molotnikov, A.; Birbilis, N. Effect of energy density on the interface evolution of stainless steel 316L deposited upon IN625 via directed energy deposition. *J. Mater. Sci.* **2020**, *55*, 13314–13328. <https://doi.org/10.1007/s10853-020-04913-y>.
90. Li, W.; Karnati, S.; Kriewall, C.; Liou, F.; Newkirk, J.; Brown, Taminger, K.; Seufzer, W. Fabrication and characterization of a functionally graded material from Ti-6Al-4V to SS316 by laser metal deposition. *Addit. Manuf.* **2017**, *14*, 95–104. <https://doi.org/10.1016/j.addma.2016.12.006>.
91. Onuikwe, B.; Bandyopadhyay, A. Functional bimetallic joints of Ti6Al4V to SS410. *Addit. Manuf.* **2020**, *31*, 100931. <https://doi.org/10.1016/j.addma.2019.100931>.
92. Babuska, T.F.; Krick, B.A.; Susan, D.F.; Kustas, A.B. Comparison of powder bed fusion and directed energy deposition for tailoring mechanical properties of traditionally brittle alloys. *Manuf. Lett.* **2021**, *28*, 30–34. <https://doi.org/10.1016/j.mfglet.2021.02.003>.
93. Svetlizky, D.; Das, M.; Zheng, B.; Vyatskikh, A.; Bose, S.; Bandyopadhyay, A.; Schoenung, J.; Lavernia, E.; Eliaz, N. Directed energy deposition (DED) additive manufacturing: Physical characteristics, defects, challenges and applications. *Mater. Today* **2021**, *49*, 271–295. <https://doi.org/10.1016/j.mattod.2021.03.020>.
94. Pham, N.T.-H.; Nguyen, V.-T. Wear Properties of TiC-Reinforced Co50 Composite Coatings from Room Temperature to High Temperature. *Adv. Mater. Sci. Eng.* **2020**, *2020*, 6849081. <https://doi.org/10.1155/2020/6849081>.
95. Farren, J.D.; DuPont, J.N.; Noecker, F.F. Fabrication of a carbon steel-to-stainless steel transition joint using direct laser deposition-A feasibility study. *Weld. J.* **2007**, *86*, 55.

96. Kim, D.K.; Woo, W.; Kim, E.Y.; Choi, S.H. Microstructure and mechanical characteristics of multi-layered materials composed of 316L stainless steel and ferritic steel produced by direct energy deposition. *J. Alloys Compd.* **2019**, *774*, 896–907. <https://doi.org/10.1016/J.JALLCOM.2018.09.390>.
97. Soodi, M.; Masood, S.H.; Brandt, M. Thermal expansion of functionally graded and wafer-layered structures produced by laser direct metal deposition. *Int. J. Adv. Manuf. Technol.* **2013**, *69*, 2011–2018. <https://doi.org/10.1007/S00170-013-5157-9/METRICS>.
98. Eliseeva, O.V.; Kirk, T.; Samimi, P.; Malak, R.; Arróyave, R.; Elwany, A.; Karaman, I. Functionally Graded Materials through robotics-inspired path planning. *Mater. Des.* **2019**, *182*, 107975. <https://doi.org/10.1016/J.MATDES.2019.107975>.
99. Su, Y.; Chen, B.; Tan, C.; Song, X.; Feng, J. Influence of composition gradient variation on the microstructure and mechanical properties of 316 L/Inconel718 functionally graded material fabricated by laser additive manufacturing. *J. Mater. Process. Technol.* **2020**, *283*, 116702. <https://doi.org/10.1016/J.JMATPROTEC.2020.116702>.
100. Yadav, S.; Jinoop, A.N.; Sinha, N.; Paul, C.P.; Bindra, K.S. Parametric investigation and characterization of laser directed energy deposited copper-nickel graded layers. *Int. J. Adv. Manuf. Technol.* **2020**, *108*, 3779–3791. <https://doi.org/10.1007/S00170-020-05644-9/FIGURES/12>.
101. Griffith, M.L.; Harwell, L.D.; Romero, J.T.; Schlienger, E.; Atwood, C.L.; Smugeresky, J.E. Multi-Material Processing by Lens. In Proceedings of the International Solid Freeform Fabrication Symposium, Austin, TX, USA, 11–13 August 1997. <https://doi.org/10.15781/T21J97T99>.

102. Meng, W.; Zhang, W.; Zhang, W.; Yin, X.; Cui, B. Fabrication of steel-Inconel functionally graded materials by laser melting deposition integrating with laser synchronous preheating. *Opt. Laser Technol.* **2020**, *131*, 106451. <https://doi.org/10.1016/J.OPTLASTEC.2020.106451>.
103. Carroll, B.E.; Otis, R.; Borgonia, J.; Suh, J.; Dillon, R.; Shapiro, A.; Hofmann, D.; Liu, Z.; Beese, A. Functionally graded material of 304L stainless steel and inconel 625 fabricated by directed energy deposition: Characterization and thermodynamic modeling. *Acta Mater.* **2016**, *108*, 46–54. <https://doi.org/10.1016/J.ACTAMAT.2016.02.019>.
104. Ni, X.; Zhang, L.; Wu, W.; Zhu, D.; Kong, D.; Dong, C.; Zhu, G. Functionally Nb graded inconel 718 alloys fabricated by laser melting deposition: Mechanical properties and corrosion behavior. *Anti-Corros. Methods Mater.* **2020**, *67*, 16–23. <https://doi.org/10.1108/ACMM-06-2019-2131/FULL/PDF>.
105. Onuike, B.; Heer, B.; Bandyopadhyay, A. Additive manufacturing of Inconel 718—Copper alloy bimetallic structure using laser engineered net shaping (LENS™). *Addit. Manuf.* **2018**, *21*, 133–140. <https://doi.org/10.1016/J.ADDMA.2018.02.007>.
106. Chen, B.; Wang, T.; Xi, X.; Tan, C.; Song, X. Additive manufacturing of Ti-Al functionally graded material by laser based directed energy deposition. *Rapid. Prototyp. J.* **2023**, *29*, 558–568. <https://doi.org/10.1108/RPJ-04-2022-0117/FULL/PDF>.
107. Schneider-Maunoury, C.; Weiss, L.; Acquier, P.; Boisselier, D.; Laheurte, P. Functionally graded Ti6Al4V-Mo alloy manufactured with DED-CLAD® process. *Addit. Manuf.* **2017**, *17*, 55–66. <https://doi.org/10.1016/J.ADDMA.2017.07.008>.

108. Meng, W.; Xiaohui, Y.; Zhang, W.; Junfei, F.; Lijie, G.; Qunshuang, M.; Bing, C. Additive manufacturing of a functionally graded material from Inconel625 to Ti6Al4V by laser synchronous preheating. *J. Mater. Process. Technol.* **2020**, *275*, 116368. <https://doi.org/10.1016/J.JMATPROTEC.2019.116368>.
109. Sun, Z.; Ji, X.; Zhang, W.; Chang, L.; Xie, G.; Chang, H.; Zhou, L. Microstructure evolution and high temperature resistance of Ti6Al4V/Inconel625 gradient coating fabricated by laser melting deposition. *Mater. Des.* **2020**, *191*, 108644. <https://doi.org/10.1016/J.MATDES.2020.108644>.
110. Sahasrabudhe, H.; Harrison, R.; Carpenter, C.; Bandyopadhyay, A. Stainless steel to titanium bimetallic structure using LENSTM. *Addit. Manuf.* **2015**, *5*, 1–8. <https://doi.org/10.1016/J.ADDMA.2014.10.002>.
111. Bobbio, L.D.; Otis, R.; Borgonia, J.; Dillon, R.; Shapiro, A.; Liu, Z.; Beese, A. Additive manufacturing of a functionally graded material from Ti-6Al-4V to Invar: Experimental characterization and thermodynamic calculations. *Acta Mater.* **2017**, *127*, 133–142. <https://doi.org/10.1016/J.ACTAMAT.2016.12.070>.
112. Krishna, B.V.; Xue, W.; Bose, S.; Bandyopadhyay, A. Functionally graded Co–Cr–Mo coating on Ti–6Al–4V alloy structures. *Acta Biomater.* **2008**, *4*, 697–706. <https://doi.org/10.1016/J.ACTBIO.2007.10.005>.
113. Li, W.; Zhang, J.; Zhang, X.; Liou, F. Effect of optimizing particle size on directed energy deposition of Functionally Graded Material with blown Pre-Mixed Multi-Powder. *Manuf. Lett.* **2017**, *13*, 39–43. <https://doi.org/10.1016/J.MFGLET.2017.07.001>.

114. Shang, C.; Wang, C.; Li, C.; Yang, G.; Xu, G.; You, J. Eliminating the crack of laser 3D printed functionally graded material from TA15 to Inconel718 by base preheating. *Opt. Laser Technol.* **2020**, *126*, 106100. <https://doi.org/10.1016/j.optlastec.2020.106100>.
115. Wang, F.; Mei, J.; Wu, X. Direct laser fabrication of Ti6Al4V/TiB. *J. Mater. Process. Technol.* **2008**, *195*, 321–326. <https://doi.org/10.1016/J.JMATPROTEC.2007.05.024>.
116. Wang, F.; Mei, J.; Wu, X. Microstructure study of direct laser fabricated Ti alloys using powder and wire. *Appl. Surf. Sci.* **2006**, *253*, 1424–1430. <https://doi.org/10.1016/J.APSUSC.2006.02.028>.
117. Ma, R.; Liu, Z.; Wang, W.; Xu, G.; Wang, W. Laser deposition melting of TC4/TiAl functionally graded material. *Vacuum* **2020**, *177*, 109349. <https://doi.org/10.1016/J.VACUUM.2020.109349>.
118. Qu, H.P.; Li, P.; Zhang, S.Q.; Li, A.; Wang, H.M. Microstructure and mechanical property of laser melting deposition (LMD) Ti/TiAl structural gradient material. *Mater. Des.* **2010**, *31*, 574–582. <https://doi.org/10.1016/J.MATDES.2009.07.004>.
119. Liu, Y.; Liu, C.; Liu, W.; Ma, Y.; Zhang, C.; Cai, Q.; Liu, B. Microstructure and properties of Ti/Al lightweight graded material by direct laser deposition. *Mater. Sci. Technol.* **2018**, *34*, 945–951. <https://doi.org/10.1080/02670836.2017.1412042>.
120. Schneider-Maunoury, C.; Weiss, L.; Perroud, O.; Joguet, D.; Boisselier, D.; Laheurte, P. An application of differential injection to fabricate functionally graded Ti-Nb alloys using DED-CLAD® process. *J. Mater. Process. Technol.* **2019**, *268*, 171–180. <https://doi.org/10.1016/J.JMATPROTEC.2019.01.018>.

121. Zhang, Y.Z.; Meacock, C.; Vilar, R. Laser powder micro-deposition of compositional gradient Ti–Cr alloy. *Mater. Des.* **2010**, *31*, 3891–3895. <https://doi.org/10.1016/J.MATDES.2010.02.052>.
122. Liu, Y.; Liang, C.; Liu, W.; Ma, Y.; Liu, C.; Zhang, C. Dilution of Al and V through laser powder deposition enables a continuously compositionally Ti/Ti6Al4V graded structure. *J. Alloys Compd.* **2018**, *763*, 376–383. <https://doi.org/10.1016/J.JALLCOM.2018.05.289>.
123. Hu, Y.; Ning, F.; Wang, H.; Cong, W.; Zhao, B. Laser engineered net shaping of quasi-continuous network microstructural TiB reinforced titanium matrix bulk composites: Microstructure and wear performance. *Opt. Laser Technol.* **2018**, *99*, 174–183. <https://doi.org/10.1016/J.OPTLASTEC.2017.08.032>.
124. Hu, Y.; Zhao, B.; Ning, F.; Wang, H.; Cong, W. In-situ ultrafine three-dimensional quasi-continuous network microstructural TiB reinforced titanium matrix composites fabrication using laser engineered net shaping. *Mater. Lett.* **2017**, *195*, 116–119. <https://doi.org/10.1016/J.MATLET.2017.02.112>.
125. Lima, D.D.; Mantri, S.; Mikler, C.; Contieri, R.; Yannetta, C.; Campo, K.; Lopes, E.; Styles, M.; Borkar, T.; Caram, R.; Banerjee, R. Laser additive processing of a functionally graded internal fracture fixation plate. *Mater. Des.* **2017**, *130*, 8–15. <https://doi.org/10.1016/j.matdes.2017.05.034>.
126. Hofmann, D.C.; Roberts, S.; Otis, R.; Kolodziejska, J.; Dillon, R.; Suh, J.; Shapiro, A.A.; Liu, Z.; Borgonia, J. “Developing Gradient Metal Alloys through Radial Deposition Additive Manufacturing,” *Sci Rep*, vol. 4, no. 1, p. 5357, 2014, doi: 10.1038/srep05357.

127. Choi, J.-W.; Kim, H.-C.; Wicker, R. Multi-material stereolithography. *J. Mater. Process. Technol.* **2011**, 211, 318–328. <https://doi.org/10.1016/j.jmatprotec.2010.10.003>.
128. Wicker, R.; Medina F.; Elkins C. Muti-material Stereolithography. US Patent US7556490B2, filed 30 July 2004 and issued 07 July 2009.
129. Inamdar, A.; Magana, M.; Medina, F.; Grajeda, Y.; Wicker, R. Development of an automated multiple material stereolithography machine. In Proceedings of the 2006 International Solid Freeform Fabrication Symposium, Austin, TX, USA, 14–16 August 2006.
130. Espalin, D.; Ramirez, J.A.; Medina, F.; Wicker, R. Multi-material, multi-technology FDM: Exploring build process variations. *Rapid Prototyp. J.* **2014**, 20, 236–244. <https://doi.org/10.1108/RPJ-12-2012-0112>.
131. Ali, M.H.; Mir-Nasiri, N.; Ko, W.L. Multi-nozzle extrusion system for 3D printer and its control mechanism. *Int. J. Adv. Manuf. Technol.* **2016**, 86, 999–1010. <https://doi.org/10.1007/s00170-015-8205-9>.
132. Rocha, V.G.; Saiz, E.; Tirichenko, I.S.; García-Tuñón, E. Direct ink writing advances in multi-material structures for a sustainable future. *J. Mater. Chem. A Mater.* **2020**, 8, 15646–15657.
133. Compton, B.G.; Lewis, J.A. 3D-Printing of Lightweight Cellular Composites. *Adv. Mater.* **2014**, 26, 5930–5935. <https://doi.org/10.1002/adma.201401804>.
134. Rocha, V.G.; et al. Multimaterial 3D Printing of Graphene-Based Electrodes for Electrochemical Energy Storage Using Thermoresponsive Inks. *ACS Appl. Mater. Interfaces* **2017**, 9, 37136–37145. <https://doi.org/10.1021/acsami.7b10285>.

135. Mueller, J.; Raney, J.R.; Shea, K.; Lewis, J.A. Architected Lattices with High Stiffness and Toughness via Multicore–Shell 3D Printing. *Adv. Mater.* **2018**, *30*, 1705001. <https://doi.org/10.1002/adma.201705001>.
136. Nazir, A.; Gokcekaya, O.; Md Masum Billah, K.; Ertugrul, O.; Jiang, J.; Sun, J.; Hussain, S. Multi-material additive manufacturing: A systematic review of design, properties, applications, challenges, and 3D printing of materials and cellular metamaterials. *Mater. Des.* **2023**, *226*, 111661. <https://doi.org/10.1016/j.matdes.2023.111661>.
137. Gander, J.D.; Giacomini, A.J. Review of die lip buildup in plastics extrusion. *Polym. Eng. Sci.* **1997**, *37*, 1113–1126. <https://doi.org/10.1002/pen.11756>.
138. Unkovskiy, A.; Wahl, E.; Huettig, F.; Keutel, C.; Spintzyk, S. Multimaterial 3D printing of a definitive silicone auricular prosthesis: An improved technique. *J. Prosthet. Dent.* **2021**, *125*, 946–950. <https://doi.org/10.1016/j.prosdent.2020.02.021>.
139. Hu, Q.; Rance, G.; Trindade, G.; Pervan, D.; Jiang, L.; Foerster, A.; Turyanska, L.; Tuck, C.; Irvine, D.; Hague, R.; Wildman, R. The influence of printing parameters on multi-material two-photon polymerisation based micro additive manufacturing. *Addit. Manuf.* **2022**, *51*, 102575. <https://doi.org/10.1016/j.addma.2021.102575>.
140. Lu, L.; Tang, X.; Hu, S.; Pan, Y. Acoustic Field-Assisted Particle Patterning for Smart Polymer Composite Fabrication in Stereolithography. *3D Print Addit. Manuf.* **2018**, *5*, 151–159. <https://doi.org/10.1089/3dp.2017.0157>.
141. Jiang, C.-P.; Hentihu, M.F.R.; Lee, S.-Y.; Lin, R. Multiresin Additive Manufacturing Process for Printing a Complete Denture and an Analysis of Accuracy. *3D Print Addit. Manuf.* **2022**, *9*, 511–519.

142. Mansouri, M.R.; Montazerian, H.; Schmauder, S.; Kadkhodapour, J. 3D-printed multimaterial composites tailored for compliancy and strain recovery. *Compos. Struct.* **2018**, *184*, 11–17. <https://doi.org/10.1016/j.compstruct.2017.09.049>.
143. Sarvestani, H.Y.; Akbarzadeh, A.H.; Therriault, D.; Lévesque, M. Engineered bi-material lattices with thermo-mechanical programmability. *Compos. Struct.* **2021**, *263*, 113705. <https://doi.org/10.1016/j.compstruct.2021.113705>.
144. Lopes, L.R.; Silva, A.F.; Carneiro, O.S. Multi-material 3D printing: The relevance of materials affinity on the boundary interface performance. *Addit. Manuf.* **2018**, *23*, 45–52. <https://doi.org/10.1016/j.addma.2018.06.027>.
145. Yin, J.; Lu, C.; Fu, J.; Huang, Y.; Zheng, Y. Interfacial bonding during multi-material fused deposition modeling (FDM) process due to inter-molecular diffusion. *Mater. Des.* **2018**, *150*, 104–112. <https://doi.org/10.1016/j.matdes.2018.04.029>.
146. Lin, W.; Shen, H.; Xu, G.; Zhang, L.; Fu, J.; Deng, X. Single-layer temperature-adjusting transition method to improve the bond strength of 3D-printed PCL/PLA parts. *Compos Part A Appl. Sci. Manuf.* **2018**, *115*, 22–30. <https://doi.org/10.1016/j.compositesa.2018.09.008>.
147. Mueller, J.; Lewis, J.A.; Bertoldi, K. Architected Multimaterial Lattices with Thermally Programmable Mechanical Response. *Adv. Funct. Mater.* **2022**, *32*, 2105128. <https://doi.org/10.1002/adfm.202105128>.
148. Khondoker, M.A.H.; Asad, A.; Sameoto, D. Printing with mechanically interlocked extrudates using a custom bi-extruder for fused deposition modelling. *Rapid Prototyp. J.* **2018**, *24*, 921–934.

- 149.Ribeiro, M.; Carneiro, O.S.; da Silva, A.F. Interface geometries in 3D multi-material prints by fused filament fabrication. *Rapid Prototyp. J.* **2019**, *25*, 38–46.
- 150.Khatri, N.; Egan, P. Tailored Energy Absorption for 3D Printed Multi-Material Cellular Structures Using ABS and TPU. In Proceedings of the ASME International Mechanical Engineering Congress and Exposition, Virtual, 1–5 November 2021. <https://doi.org/10.1115/IMECE2021-73699>.
- 151.Singh, S.; Singh, N.; Gupta, M.; Prakash, C.; Singh, R. Mechanical feasibility of ABS/HIPS-based multi-material structures primed by low-cost polymer printer. *Rapid Prototyp. J.* **2019**, *25*, 152–161.
- 152.Mustafa, I.; Kwok, T.-H. Development of Intertwined Infills to Improve Multi-Material Interfacial Bond Strength. *J. Manuf. Sci. Eng.* **2021**, *144*, 31009. <https://doi.org/10.1115/1.4051884>.
- 153.Singh, R.; Kumar, R.; Farina, I.; Colangelo, F.; Feo, L.; Fraternali, F. Multi-material additive manufacturing of sustainable innovative materials and structures. *Polymers* **2019**, *11*, 62. <https://doi.org/10.3390/polym11010062>.
- 154.Baca, D.; Ahmad, R. The impact on the mechanical properties of multi-material polymers fabricated with a single mixing nozzle and multi-nozzle systems via fused deposition modeling. *Int. J. Adv. Manuf. Technol.* **2020**, *106*, 4509–4520. <https://doi.org/10.1007/s00170-020-04937-3>.
- 155.Yirmibesoglu, O.D.; Simonsen, L.; Manson, R.; Davidson, J.; Healy, K.; Menguc, Y.; Wallin, T. Multi-material direct ink writing of photocurable elastomeric foams. *Commun. Mater.* **2021**, *2*, 82. <https://doi.org/10.1038/s43246-021-00186-3>.

156. Politis, D.J.; Politis, N.J.; Lin, J. Review of recent developments in manufacturing lightweight multi-metal gears. *Prod. Eng.* **2021**, *15*, 235–262. <https://doi.org/10.1007/s11740-020-01011-5>.
157. Chastel, Y.; Passemard, L. Joining Technologies for Future Automobile Multi-material Modules. *Procedia Eng.* **2014**, *81*, 2104–2110. <https://doi.org/10.1016/j.proeng.2014.10.293>.
158. Pattnaik, S.; Karunakar, D.B.; Jha, P.K. Developments in investment casting process—A review. *J. Mater. Process. Technol.* **2012**, *212*, 2332–2348. <https://doi.org/10.1016/j.jmatprotec.2012.06.003>.
159. Priyadarshi, A.K.; Gupta, S.K.; Gouker, R.; Krebs, F.; Shroeder, M.; Warth, S. Manufacturing multi-material articulated plastic products using in-mold assembly. *Int. J. Adv. Manuf. Technol.* **2007**, *32*, 350–365. <https://doi.org/10.1007/s00170-005-0343-z>.
160. Miller, W.H. Gear Blanks. US Patent 3847557, filed 20 Aug 1973 and issued 12 Nov 1974.
161. Gouker, R.M.; Gupta, S.K.; Bruck, H.A.; Holzschuh, T. Manufacturing of multi-material compliant mechanisms using multi-material molding. *Int. J. Adv. Manuf. Technol.* **2006**, *30*, 1049–1075. <https://doi.org/10.1007/s00170-005-0152-4>.
162. Bakke, A.O.; Nordmark, A.; Arnberg, L.; Li, Y. Sn-Aided Joining of Cast Aluminum and Steel Through a Compound Casting Process. *Metall. Mater. Trans. B* **2022**, *53*, 60–70. <https://doi.org/10.1007/s11663-021-02329-w>.
163. Locke, C.; Guggemos, M.; Gruber, M.; Maier, L.; Mayr, L.; Weiß, T.; Volk, W.; Günther, D. Compound Casting of Aluminum with Sheet Steel in 3D Sand Casting Using an Inductive Heating System. *Metals* **2023**, *13*, 354. <https://doi.org/10.3390/met13020354>.

164. Moodispaw, M.P.; Chen, B.; Luo, A.A.; Wang, Q. Achieving Metallurgical Bonding in Aluminum/Steel Bimetallic Castings. *Int. J. Met.* **2024**. <https://doi.org/10.1007/s40962-023-01241-0>.
165. Fang, Y.; Jiang, X.; Mo, D.; Zhu, D.; Luo, Z. A review on dissimilar metals' welding methods and mechanisms with interlayer. *Int. J. Adv. Manuf. Technol.* **2019**, 102, 2845–2863. <https://doi.org/10.1007/s00170-019-03353-6>.
166. Kuang, B.; Shen, Y.; Chen, W.; Yao, X.; Xu, H.; Gao, J.; Zhang, J. The dissimilar friction stir lap welding of 1A99 Al to pure Cu using Zn as filler metal with 'pinless' tool configuration. *Mater. Des.* **2015**, 68, 54–62. <https://doi.org/10.1016/j.matdes.2014.12.008>.
167. Liu, L.; Ren, D.; Liu, F. A review of dissimilar welding techniques for magnesium alloys to aluminum alloys. *Materials* **2014**, 7, 3735–3757. <https://doi.org/10.3390/ma7053735>.
168. Yu, W.; Zhao, H.; Huang, Z.; Chen, X.; Aman, Y.; Li, S.; Zhai, H.; Guo, Z.; Xiong, S. Microstructure evolution and bonding mechanism of Ti₂SnC-Ti6Al4V joint by using Cu pure foil interlayer. *Mater. Charact.* **2017**, 127, 53–59. <https://doi.org/10.1016/j.matchar.2017.01.035>.
169. Peyre, P.; Berthe, L.; Dal, M.; Pouzet, S.; Sallamand, P.; Tomashchuk, I. Generation and characterization of T40/A5754 interfaces with lasers. *J. Mater. Process. Technol.* **2014**, 214, 1946–1953. <https://doi.org/10.1016/j.jmatprotec.2014.04.019>.
170. Li, L.; Tan, C.; Chen, Y.; Guo, W.; Song, F. Comparative study on microstructure and mechanical properties of laser welded–braze Mg/mild steel and Mg/stainless steel joints. *Mater. Des.* **2013**, 43, 59–65. <https://doi.org/10.1016/j.matdes.2012.06.057>.

- 171.Hossain, M.A.M.; Hasan, M.T.; Hong, S.-T.; Miles, M.; Cho, H.-H.; Han, H.N. Mechanical Behaviors of Friction Stir Spot Welded Joints of Dissimilar Ferrous Alloys under Opening-Dominant Combined Loads. *Adv. Mater. Sci. Eng.* **2014**, 2014, 572970. <https://doi.org/10.1155/2014/572970>.
- 172.Taniguchi, M.; Ukai, Y.; Tsunekawa, H.; Shioiri, H. Structure for Fastening Ring Gear to Differential Case, and Differential Device Employing Same. U.S. Patent US2013/0074649 A1, filed 04 June 2010 and issued 28 March 2013.
- 173.Matsumoto, R.; Hanami, S.; Ogura, A.; Yoshimura, H.; Osakada, K. New plastic joining method using indentation of cold bar to hot forged part. *CIRP Ann.* **2008**, 57, 279–282. <https://doi.org/10.1016/j.cirp.2008.03.126>.
- 174.Qiao, J.; Kou, S.Q.; He, D.Y.; Yang, S.H. Torque Strength and Influencing Factors Analysis for Assembled Camshaft by Knurling Joining. *Mater. Sci. For.* **2008**, 575–578, 216–221. <https://doi.org/10.4028/www.scientific.net/MSF.575-578.216>.
- 175.Wohletz, S.; Groche, P. Temperature Influence on Bond Formation in Multi-material Joining by Forging. *Procedia Eng.* **2014**, 81, 2000–2005. <https://doi.org/10.1016/j.proeng.2014.10.271>.
- 176.Meng, Z.; Jia, X.; Feng, W.; Zhuang, W.; Wu, M. Investigation on Interfacial Bonding Characteristics of Steel/Aluminum Bi-Metal Gears by Hot Forging Processing. *Metals* **2022**, 12, 1244. <https://doi.org/10.3390/met12081244>.
- 177.Behrens, B.-A.; Kosch, K.-G. Development of the heating and forming strategy in compound forging of hybrid steel-aluminum parts. *Mater. Werkst.* **2011**, 42, 973–978. <https://doi.org/10.1002/mawe.201100795>.

- 178.Kriwall, M.; Stonis, M.; Bick, T.; Treutler, K.; Wesling, V. Dependence of the Joint Strength on Different Forming Steps and Geometry in Hybrid Compound Forging of Bulk Aluminum Parts and Steel Sheets. *Procedia Manuf.* **2020**, *47*, 356–361. <https://doi.org/10.1016/j.promfg.2020.04.282>.
- 179.Hasanov, S.; Alkunte, S.; Rajeshirke, M.; Gupta, A.; Huseynov, O.; Fidan, I.; Alifui-Segbaya, F.; Rennie, A. Review on additive manufacturing of multi-material parts: Progress and challenges. *J. Manuf. Mater. Process.* **2022**, *6*, 4. <https://doi.org/10.3390/jmmp6010004>.
- 180.Okokpujie, I.P.; Bolu, C.A.; Ohunakin, O.S.; Akinlabi, E.T.; Adelekan, D.S. A Review of Recent Application of Machining Techniques, based on the Phenomena of CNC Machining Operations. *Procedia Manuf.* **2019**, *35*, 1054–1060. <https://doi.org/10.1016/j.promfg.2019.06.056>.
- 181.Paris, H.; Mokhtarian, H.; Coatanéa, E.; Museau, M.; Ituarte, I.F. Comparative environmental impacts of additive and subtractive manufacturing technologies. *CIRP Ann.* **2016**, *65*, 29–32. <https://doi.org/10.1016/j.cirp.2016.04.036>.
- 182.Laureijs, R.E.; Roca, J.B.; Narra, S.P.; Montgomery, C.; Beuth, J.L.; Fuchs, E.R.H. Metal Additive Manufacturing: Cost Competitive Beyond Low Volumes. *J. Manuf. Sci. Eng.* **2017**, *139*, 81010. <https://doi.org/10.1115/1.4035420>.
- 183.Ilin, A.; Logvinov, R.; Kulikov, A.; Prihodovsky, A.; Xu, H.; Ploshikhin, V.; Günther, B.; Bechmann, F. Computer Aided Optimisation of the Thermal Management During Laser Beam Melting Process. *Phys. Procedia* **2014**, *56*, 390–399. <https://doi.org/10.1016/j.phpro.2014.08.142>.

- 184.Hussein, A.; Hao, L.; Yan, C.; Everson, R. Finite element simulation of the temperature and stress fields in single layers built without-support in selective laser melting. *Mater. Des.* **2013**, *52*, 638–647. <https://doi.org/10.1016/j.matdes.2013.05.070>.
- 185.Gu, D.D.; Meiners, W.; Wissenbach, K.; Poprawe, R. Laser additive manufacturing of metallic components: Materials, processes and mechanisms. *Int. Mater. Rev.* **2012**, *57*, 133–164. <https://doi.org/10.1179/1743280411Y.0000000014>.
- 186.Jung, H.Y.; Choi, S.; Prashanth, K.; Stoica, M.; Scudino, S.; Yi, S.; Kühn, U.; Kim, D.; Kim, K.; Eckert, J. Fabrication of Fe-based bulk metallic glass by selective laser melting: A parameter study. *Mater. Des.* **2015**, *86*, 703–708. <https://doi.org/10.1016/j.matdes.2015.07.145>.
- 187.Gäumann, M.; Henry, S.; Cléton, F.; Wagnière, J.-D.; Kurz, W. Epitaxial laser metal forming: Analysis of microstructure formation. *Mater. Sci. Eng. A* **1999**, *271*, 232–241. [https://doi.org/10.1016/S0921-5093\(99\)00202-6](https://doi.org/10.1016/S0921-5093(99)00202-6).
- 188.Wang, C.; Zhang, J.; Liu, L.; Fu, H. Effect of Melt Superheating Treatment on Directional Solidification Interface Morphology of Multi-component Alloy. *J. Mater. Sci. Technol.* **2011**, *27*, 668–672. [https://doi.org/10.1016/S1005-0302\(11\)60123-0](https://doi.org/10.1016/S1005-0302(11)60123-0).
- 189.Shi, Q.; Gu, D.; Xia, M.; Cao, S.; Rong, T. Effects of laser processing parameters on thermal behavior and melting/solidification mechanism during selective laser melting of TiC/Inconel 718 composites. *Opt. Laser Technol.* **2016**, *84*, 9–22. <https://doi.org/10.1016/j.optlastec.2016.04.009>.

190. Garibaldi, M.; Ashcroft, I.; Simonelli, M.; Hague, R. Metallurgy of high-silicon steel parts produced using Selective Laser Melting. *Acta Mater.* **2016**, *110*, 207–216. <https://doi.org/10.1016/j.actamat.2016.03.037>.
191. Deng, Q.L.; Xie, A.N.; Ge, Z.J.; Song, J.L. Experimental Researches on Rapid Forming Full Compacted Metal Parts by Selective Laser Melting. *Mater. Sci. For.* **2006**, *532–533*, 428–431. <https://doi.org/10.4028/www.scientific.net/MSF.532-533.428>.
192. Cherry, J.A.; Davies, H.M.; Mehmood, S.; Lavery, N.P.; Brown, S.G.R.; Sienz, J. Investigation into the effect of process parameters on microstructural and physical properties of 316L stainless steel parts by selective laser melting. *Int. J. Adv. Manuf. Technol.* **2015**, *76*, 869–879. <https://doi.org/10.1007/s00170-014-6297-2>.
193. Narasimharaju, S.R.; Liu, W.; Zeng, W.; See, T.; Scott, P.; Jiang, X.; Lou, S. Surface Texture Characterization of Metal Selective Laser Melted Part with Varying Surface Inclinations. *J. Tribol.* **2021**, *143*, 51106. <https://doi.org/10.1115/1.4050455>.
194. Kadkhodapour, J.; Mirhakimi, A.S.; Montazerian, H. Chapter Four—Structural defects and mechanical properties of additively manufactured parts. In *Quality Analysis of Additively Manufactured Metals*; Kadkhodapour, J., Schmauder, S., Sajadi, F., Eds.; Elsevier: Amsterdam, The Netherlands, 2023; pp. 119–172. <https://doi.org/10.1016/B978-0-323-88664-2.00006-3>.
195. Marchese, G.; Garmendia Colera, X.; Calignano, F.; Lorusso, M.; Biamino, S.; Minetola, P.; Manfredi, D. Characterization and Comparison of Inconel 625 Processed by Selective Laser Melting and Laser Metal Deposition. *Adv. Eng. Mater.* **2017**, *19*, 1600635. <https://doi.org/10.1002/adem.201600635>.

- 196.Dinda, G.P.; Dasgupta, A.K.; Mazumder, J. Laser aided direct metal deposition of Inconel 625 superalloy: Microstructural evolution and thermal stability. *Mater. Sci. Eng. A* **2009**, *509*, 98–104. <https://doi.org/10.1016/j.msea.2009.01.009>.
- 197.Sateesh, N.H.; Kumar, G.C.M.; Prasad, K.; Srinivasa, C.K.; Vinod, A.R. Microstructure and Mechanical Characterization of Laser Sintered Inconel-625 Superalloy. *Procedia Mater. Sci.* **2014**, *5*, 772–779. <https://doi.org/10.1016/j.mspro.2014.07.327>.
- 198.Martin, N.; Hor, A.; Copin, E.; Lours, P.; Ratsifandrihana, L. Correlation between microstructure heterogeneity and multi-scale mechanical behavior of hybrid LPBF-DED Inconel 625. *J. Mater. Process. Technol.* **2022**, *303*, 117542. <https://doi.org/10.1016/j.jmatprotec.2022.117542>.
- 199.Ma, D.; Stoica, A.D.; Wang, Z.; Beese, A.M. Crystallographic texture in an additively manufactured nickel-base superalloy. *Mater. Sci. Eng. A* **2017**, *684*, 47–53. <https://doi.org/10.1016/j.msea.2016.12.028>.
- 200.Dixit, S.; Liu, S.; Murdoch, H.A.; Smith, P.M. Investigating build orientation-induced mechanical anisotropy in additive manufacturing 316L stainless steel. *Mater. Sci. Eng. A* **2023**, *880*, 145308. <https://doi.org/10.1016/j.msea.2023.145308>.
- 201.Wolff, S.; Lee, T.; Faierson, E.; Ehmman, K.; Cao, J. Anisotropic properties of directed energy deposition (DED)-processed Ti–6Al–4V. *J. Manuf. Process.* **2016**, *24*, 397–405. <https://doi.org/10.1016/j.jmapro.2016.06.020>.
- 202.Žbontar, M.; Petrič, M.; Mrvar, P. The influence of cooling rate on microstructure and mechanical properties of alsi9cu3. *Metals* **2021**, *11*, 186. <https://doi.org/10.3390/met11020186>.

203. Górný, M.; Tyrała, E. Effect of Cooling Rate on Microstructure and Mechanical Properties of Thin-Walled Ductile Iron Castings. *J. Mater. Eng. Perform.* **2013**, *22*, 300–305. <https://doi.org/10.1007/s11665-012-0233-0>.
204. Mouritz, A.P. (Ed.) 6—Production and casting of aerospace metals. In *Introduction to Aerospace Materials*; Woodhead Publishing: Sawston, UK, 2012; pp. 128–153. <https://doi.org/10.1533/9780857095152.128>.
205. Pang, S.; Wu, G.; Liu, W.; Sun, M.; Zhang, Y.; Liu, Z.; Ding, W. Effect of cooling rate on the microstructure and mechanical properties of sand-casting Mg–10Gd–3Y–0.5Zr magnesium alloy. *Mater. Sci. Eng. A* **2013**, *562*, 152–160. <https://doi.org/10.1016/j.msea.2012.11.016>.
206. Gong, L.; Chen, B.; Zhang, L.; Ma, Y.; Liu, K. Effect of cooling rate on microstructure, microsegregation and mechanical properties of cast Ni-based superalloy K417G. *J. Mater. Sci. Technol.* **2018**, *34*, 811–820. <https://doi.org/10.1016/j.jmst.2017.03.023>.
207. Papanikolaou, M.; Saxena, P. Chapter 7—Sustainable casting processes through simulation-driven optimization. In *Sustainable Manufacturing*; Gupta, K., Salonitis, K., Eds.; Elsevier: Amsterdam, The Netherlands, 2021; pp. 165–198. <https://doi.org/10.1016/B978-0-12-818115-7.00003-1>.
208. Yamabe-Mitarai, Y.; Kuroda, S.; Motohashi, N.; Matsumoto, H.; Miyamoto, G.; Chandiran, E.; Yoshida, Y.; Itsumi, Y. Effect of Forging Temperature on Microstructure Evolution and Tensile Properties of Ti-17 Alloys. *Mater. Trans* **2019**, *60*, 1733–1739. <https://doi.org/10.2320/matertrans.ME201911>.

209. Suris, J.A.; Yurgel, C.C.; de Sousa, R.A. Influence of the Grain-Flow Orientation after Hot Forging Process Evaluated through Rotational Flexing Fatigue Test. *Metals* **2023**, *13*, 187. <https://doi.org/10.3390/met13020187>.
210. Zhou, J.; Liao, H.; Chen, H.; Huang, A. Effects of hot-forging and subsequent annealing on microstructure and mechanical behaviors of Fe₃₅Ni₃₅Cr₂₀Mn₁₀ high-entropy alloy. *Mater. Charact.* **2021**, *178*, 111251. <https://doi.org/10.1016/j.matchar.2021.111251>.
211. ZHANG, Y.; ZHANG, H.; LI, J.; LIU, W. Effect of Heat Input on Microstructure and Toughness of Coarse Grain Heat Affected Zone in Nb Microalloyed HSLA Steels. *J. Iron Steel Res. Int.* **2009**, *16*, 73–80. [https://doi.org/10.1016/S1006-706X\(10\)60014-3](https://doi.org/10.1016/S1006-706X(10)60014-3).
212. Fujii, H.; Cui, L.; Tsuji, N.; Maeda, M.; Nakata, K.; Nogi, K. Friction stir welding of carbon steels. *Mater. Sci. Eng. A* **2006**, *429*, 50–57. <https://doi.org/10.1016/j.msea.2006.04.118>.
213. Zhu, X.K.; Chao, Y.J. Numerical simulation of transient temperature and residual stresses in friction stir welding of 304L stainless steel. *J. Mater. Process. Technol.* **2004**, *146*, 263–272. <https://doi.org/10.1016/j.jmatprotec.2003.10.025>.
214. Park, S.H.C.; Sato, Y.S.; Kokawa, H.; Okamoto, K.; Hirano, S.; Inagaki, M. Boride Formation Induced by pcBN Tool Wear in Friction-Stir-Welded Stainless Steels. *Metall. Mater. Trans. A* **2009**, *40*, 625–636. <https://doi.org/10.1007/s11661-008-9709-9>.
215. Pan, Z.; Feng, Y.; Liang, S.Y. Material microstructure affected machining: A review. *Manuf. Rev.* **2017**, *4*, 5. <https://doi.org/10.1051/mfreview/2017004>.
216. Meyers, M.A.; Xu, Y.B.; Xue, Q.; Pérez-Prado, M.T.; McNelley, T.R. Microstructural evolution in adiabatic shear localization in stainless steel. *Acta Mater.* **2003**, *51*, 1307–1325. [https://doi.org/10.1016/S1359-6454\(02\)00526-8](https://doi.org/10.1016/S1359-6454(02)00526-8).

- 217.Chuzhoy, L.; DeVor, R.E.; Kapoor, S.G.; Bammann, D.J. Microstructure-Level Modeling of Ductile Iron Machining. *J. Manuf. Sci. Eng.* **2002**, *124*, 162–169. <https://doi.org/10.1115/1.1455642>.
- 218.Xu, Y.; Zhang, J.; Bai, Y.; Meyers, M.A. Shear Localization in Dynamic Deformation: Microstructural Evolution. *Metall. Mater. Trans. A* **2008**, *39*, 811–843. <https://doi.org/10.1007/s11661-007-9431-z>.
- 219.Hadadzadeh, A.; Amirkhiz, B.S.; Shakerin, S.; Kelly, J.; Li, J.; Mohammadi, M. Microstructural investigation and mechanical behavior of a two-material component fabricated through selective laser melting of AlSi10Mg on an Al-Cu-Ni-Fe-Mg cast alloy substrate. *Addit. Manuf.* **2020**, *31*, 100937. <https://doi.org/10.1016/j.addma.2019.100937>.
- 220.Kanagaraj, S.; Pattanayak, S. Measurement of the thermal expansion of metal and FRPs. *Cryogenics* **2003**, *43*, 399–424. [https://doi.org/10.1016/S0011-2275\(03\)00096-1](https://doi.org/10.1016/S0011-2275(03)00096-1).
- 221.Wang, F.E. Chapter 2—Phase Equilibrium Diagrams. In *Bonding Theory for Metals and Alloys*, 2nd ed.; Wang, F.E., Ed.; Elsevier: Amsterdam, The Netherlands, 2019; pp. 5–41. <https://doi.org/10.1016/B978-0-444-64201-1.00002-6>.
- 222.Springer, H.; Kostka, A.; Santos, J.F.D.; Raabe, D. Influence of intermetallic phases and Kirkendall-porosity on the mechanical properties of joints between steel and aluminium alloys. *Mater. Sci. Eng. A* **2011**, *528*, 4630–4642. <https://doi.org/10.1016/j.msea.2011.02.057>.
- 223.Bergh, T.; Arbo, S.; Hagen, A.; Blindheim, J.; Friis, J.; Khalid, M.; Ringdalen, I.; Holmestad, R.; Westermann, I.; Vullum, P. On intermetallic phases formed during

- interdiffusion between aluminium alloys and stainless steel. *Intermetallics* **2022**, 142, 107443. <https://doi.org/10.1016/j.intermet.2021.107443>.
224. Chen, N.; Wang, M.; Wang, H.-P.; Wan, Z.; Carlson, B.E. Microstructural and mechanical evolution of Al/steel interface with Fe₂Al₅ growth in resistance spot welding of aluminum to steel. *J. Manuf. Process* **2018**, 34, 424–434. <https://doi.org/10.1016/j.jmapro.2018.06.024>.
225. Borrisutthekul, R.; Yachi, T.; Miyashita, Y.; Mutoh, Y. Suppression of intermetallic reaction layer formation by controlling heat flow in dissimilar joining of steel and aluminum alloy. *Mater. Sci. Eng. A* **2007**, 467, 108–113. <https://doi.org/10.1016/j.msea.2007.03.049>.
226. Hatano, R.; Ogura, T.; Matsuda, T.; Sano, T.; Hirose, A. Relationship between intermetallic compound layer thickness with deviation and interfacial strength for dissimilar joints of aluminum alloy and stainless steel. *Mater. Sci. Eng. A* **2018**, 735, 361–366. <https://doi.org/10.1016/j.msea.2018.08.065>.
227. Massalski, T.B.; Murray, J.L.; Bennett, L.H.; Baker, H. *Binary Alloy Phase Diagrams*; American Society for Metals: Metals Park, OH, USA, 1986.
228. Werner, M.R.; Fahrner, W.R. Review on Materials, Microsensors, Systems, and Devices for High-Temperature and Harsh-Environment Applications. *IEEE Trans. Ind. Electron.* **2001**, 48, 249–257.
229. Toropova, M. Bimaterial Lattices with Anisotropic Thermal Expansion. *J. Mech. Mater. Struct.* **2014**, 9, 227–244.

230. Yamamoto, N.; Gdoutos, E.; Toda, R.; White, V.; Manohara, H.; Daraio, C. Thin films with ultra-low thermal expansion. *Adv. Mater.* **2014**, *26*, 3076–3080. <https://doi.org/10.1002/adma.201304997>.
231. Zweben, C. Advances in composite materials for thermal management in electronic packaging. *JOM* **1998**, *50*, 47–51. <https://doi.org/10.1007/s11837-998-0128-6>.
232. Lu, D.D.; Wong, C.P. *Materials for Advanced Packaging*; Springer: New York, NY, USA, 2009. <https://doi.org/10.1007/978-0-387-78219-5>.
233. Bartnitzek, T.; Thelemann, T.; Apel, S.; Suphan, K.-H. Advantages and Limitations of Ceramic Packaging Technologies in Harsh Applications. **2016**. Available online: <http://meridian.allenpress.com/ism/article-pdf/2016/1/000581/2253545/isom-2016-thp23.pdf>. Accessed: 10 November 2023
234. Ju, H.; Liu, S. Damage Degree analysis of storage failure modes for plastic encapsulated microelectronic devices. *J. Phys. Conf. Ser.* **2021**, *2132*, 12048. <https://doi.org/10.1088/1742-6596/2132/1/012048>.
235. Wan, Y.J.; Li, G.; Yao, Y.M.; Zeng, X.L.; Zhu, P.L.; Sun, R. Recent advances in polymer-based electronic packaging materials. *Compos. Commun.* **2020**, *19*, 154–167. <https://doi.org/10.1016/j.coco.2020.03.011>.
236. Lai, L.; Niu, B.; Bi, Y.; Li, Y.; Yang, Z. Advancements in SiC-Reinforced Metal Matrix Composites for High-Performance Electronic Packaging: A Review of Thermo-Mechanical Properties and Future Trends. *Micromachines* **2023**, *14*, 1491. <https://doi.org/10.3390/mi14081491>.

237. Tong, X.C. *Electronic Packaging Materials and Their Functions in Thermal Managements*. In *Advanced Materials for Thermal Management of Electronic Packaging*; Springer Series in Advanced Microelectronics; Springer Science and Business Media Deutschland GmbH: Berlin/Heidelberg, Germany, 2011; Volume 30, pp. 131–167. https://doi.org/10.1007/978-1-4419-7759-5_3.
238. Adachi, S. *Handbook on Physical Properties of Semiconductors*; Springer Science & Business Media: Berlin/Heidelberg, Germany, 2004.
239. Gale, W.F.; Totemeier, T.C. (Eds.). 15—Elastic properties, damping capacity and shape memory alloys. In *Smithells Metals Reference Book*, 8th ed.; Butterworth-Heinemann: Oxford, UK 2004; pp. 1–45. <https://doi.org/10.1016/B978-075067509-3/50018-X>.
240. Gale, W.F.; Totemeier, T.C. (Eds.). 14—General physical properties. In *Smithells Metals Reference Book*, 8th ed.; Butterworth-Heinemann: Oxford, UK, 2004; pp. 1–45. <https://doi.org/10.1016/B978-075067509-3/50017-8>.
241. Kim, J.C.; Ren, Z.; Yuksel, A.; Dede, E. M.; Bandaru, P. R.; Oh, D.; Lee, J. Recent Advances in Thermal Metamaterials and Their Future Applications for Electronics Packaging. *J. Electron. Packag. Trans. ASME* **2021**, 143, 10801. <https://doi.org/10.1115/1.4047414>.
242. Vemuri, K.P.; Bandaru, P.R. An approach towards a perfect thermal diffuser. *Sci. Rep.* **2016**, 6, 29649. <https://doi.org/10.1038/srep29649>.
243. Narayana, S.; Sato, Y. Heat Flux Manipulation with Engineered Thermal Materials. *Phys. Rev. Lett.* **2012**, 108, 214303. <https://doi.org/10.1103/PhysRevLett.108.214303>.

244. Park, G.; Kang, S.; Lee, H.; Choi, W. Tunable multifunctional thermal metamaterials: Manipulation of local heat flux via assembly of unit-cell thermal shifters. *Sci. Rep.* **2017**, *7*, srep41000. <https://doi.org/10.1038/srep41000>.
245. Singhal, S.C. Solid oxide fuel cells for power generation. *WIREs Energy Environ.* **2014**, *3*, 179–194. <https://doi.org/10.1002/wene.96>.
246. Wee, J.H. Applications of proton exchange membrane fuel cell systems. *Renew. Sustain. Energy Rev.* **2007**, *11*, 1720–1738. <https://doi.org/10.1016/j.rser.2006.01.005>.
247. Ferriday, T.B.; Middleton, P.H. Alkaline fuel cell technology—A review. *Int. J. Hydrogen Energy* **2021**, *46*, 18489–18510. <https://doi.org/10.1016/j.ijhydene.2021.02.203>.
248. Sammes, N.; Bove, R.; Stahl, K. Phosphoric acid fuel cells: Fundamentals and applications. *Curr. Opin. Solid State Mater. Sci.* **2004**, *8*, 372–378. <https://doi.org/10.1016/j.cossms.2005.01.001>.
249. Contreras, R.R.; Almarza, J.; Rincón, L. Molten carbonate fuel cells: A technological perspective and review. In *Energy Sources, Part A Recovery, Utilization and Environmental Effects*; Taylor and Francis Ltd.: Abingdon, UK, 2021. <https://doi.org/10.1080/15567036.2021.2013346>.
250. Hussain, S.; Yangping, L. Review of solid oxide fuel cell materials: Cathode, anode, and electrolyte. *Energy Transit.* **2020**, *4*, 113–126. <https://doi.org/10.1007/s41825-020-00029-8>.
251. Golkhatmi, S.Z.; Asghar, M.I.; Lund, P.D. A review on solid oxide fuel cell durability: Latest progress, mechanisms, and study tools. *Renew. Sustain. Energy Rev.* **2022**, *161*, 112339. <https://doi.org/10.1016/j.rser.2022.112339>.

252. Vishwanathan, A.S. Microbial fuel cells: A comprehensive review for beginners. *3 Biotech* **2021**, 11, 248. <https://doi.org/10.1007/s13205-021-02802-y>.
253. Choudhury, A.; Chandra, H.; Arora, A. Application of solid oxide fuel cell technology for power generation—A review. *Renew. Sustain. Energy Rev.* **2013**, 20, 430–442. <https://doi.org/10.1016/j.rser.2012.11.031>.
254. Minh, N.Q.; Takahashi, T. Chapter 6—Anode. In *Science and Technology of Ceramic Fuel Cells*; Minh, N.Q., Takahashi, T., Eds.; Elsevier Science Ltd: Oxford, UK, 1995; pp. 147–164. <https://doi.org/10.1016/B978-044489568-4/50007-4>.
255. Minh, N.Q.; Takahashi, T. Chapter 5—Cathode. In *Science and Technology of Ceramic Fuel Cells*; Minh, N.Q., Takahashi, T., Eds.; Elsevier Science Ltd: Oxford, UK, 1995; pp. 117–146. <https://doi.org/10.1016/B978-044489568-4/50006-2>.
256. Wu, J.; Liu, X. Recent Development of SOFC Metallic Interconnect. *J. Mater. Sci. Technol.* **2010**, 26, 293–305. [https://doi.org/10.1016/S1005-0302\(10\)60049-7](https://doi.org/10.1016/S1005-0302(10)60049-7).
257. Sakai, N.; Stølen, S. Heat capacity and thermodynamic properties of lanthanum(III) chromate(III): LaCrO_3 , at temperatures from 298.15 K. Evaluation of the thermal conductivity. *J. Chem. Thermodyn.* **1995**, 27, 493–506. <https://doi.org/10.1006/jcht.1995.0051>.
258. Jiang, W.; Zhang, Y.; Woo, W.; Tu, S.T. Three-dimensional simulation to study the influence of foil thickness on residual stress in the bonded compliant seal design of planar solid oxide fuel cell. *J. Power Sources* **2012**, 209, 65–71. <https://doi.org/10.1016/j.jpowsour.2012.02.060>.

259. Marina, O.A.; Canfield, N.L.; Stevenson, J.W. Thermal, electrical, and electrocatalytic properties of lanthanum-doped strontium titanate. *Solid State Ion.* **2002**, 149, 21–28. [https://doi.org/10.1016/S0167-2738\(02\)00140-6](https://doi.org/10.1016/S0167-2738(02)00140-6).
260. Ullmann, H.; Trofimenko, N.; Tietz, F.; Stöver, D.; Ahmad-Khanlou, A. Correlation between thermal expansion and oxide ion transport in mixed conducting perovskite-type oxides for SOFC cathodes. *Solid State Ion.* **2000**, 138, 79–90. [https://doi.org/10.1016/S0167-2738\(00\)00770-0](https://doi.org/10.1016/S0167-2738(00)00770-0).
261. Abdin, Z.; Khalilpour, K.R. Chapter 4—Single and Polystorage Technologies for Renewable-Based Hybrid Energy Systems. In *Polygeneration with Polystorage for Chemical and Energy Hubs*; Khalilpour, K.R., Ed.; Academic Press: Cambridge, MA, USA, 2019; pp. 77–131. <https://doi.org/10.1016/B978-0-12-813306-4.00004-5>.
262. Petric, A.; Huang, P.; Tietz, F. Evaluation of La–Sr–Co–Fe–O perovskites for solid oxide fuel cells and gas separation membranes. *Solid State Ion.* **2000**, 135, 719–725. [https://doi.org/10.1016/S0167-2738\(00\)00394-5](https://doi.org/10.1016/S0167-2738(00)00394-5).
263. Ni, Q.; Chen, H.; Ge, L.; Yu, S.; Guo, L. Investigation of $\text{La}_{1-x}\text{Sm}_x\text{-ySr}_y\text{CoO}_{3-\delta}$ cathode for intermediate temperature solid oxide fuel cells. *J. Power Sources* **2017**, 349, 130–137. <https://doi.org/10.1016/j.jpowsour.2017.03.037>.
264. Hayun, H.; Wolf, R.; Barad, C.; Gelbstein, Y. Thermal shock resistant solid oxide fuel cell ceramic composite electrolytes. *J. Alloys Compd.* **2020**, 821, 153490. <https://doi.org/10.1016/j.jallcom.2019.153490>.

265. Zhang, Y.; Chen, B.; Guan, D.; Xu, M.; Ran, R.; Ni, M.; Zhou, W.; O'Hayre, R.; Shao, Z. Thermal-expansion offset for high-performance fuel cell cathodes. *Nature* **2021**, 591, 246–251. <https://doi.org/10.1038/s41586-021-03264-1>.
266. Zhou, W.; Shao, Z.; Ran, R.; Cai, R. Novel SrSc_{0.2}Co_{0.8}O_{3-δ} as a cathode material for low temperature solid-oxide fuel cell. *Electrochem. Commun.* **2008**, 10, 1647–1651. <https://doi.org/10.1016/j.elecom.2008.08.033>.
267. Zhou, W.; Ran, R.; Shao, Z.; Jin, W.; Xu, N. Evaluation of A-site cation-deficient (Ba_{0.5}Sr_{0.5})_{1-x}Co_{0.8}Fe_{0.2}O_{3-δ} (x > 0) perovskite as a solid-oxide fuel cell cathode. *J. Power Sources* **2008**, 182, 24–31. <https://doi.org/10.1016/j.jpowsour.2008.04.012>.
268. Ding, X.; Cui, C.; Guo, L. Thermal expansion and electrochemical performance of La_{0.7}Sr_{0.3}CuO_{3-δ}-Sm_{0.2}Ce_{0.8}O_{2-δ} composite cathode for IT-SOFCs. *J. Alloys Compd.* **2009**, 481, 845–850. <https://doi.org/10.1016/j.jallcom.2009.03.132>.
269. Song, Y.; Chen, Y.; Xu, M.; Wang, W.; Zhang, Y.; Yang, G.; Ran, R.; Zhou, W.; Shao, Z. A Cobalt-Free Multi-Phase Nanocomposite as Near-Ideal Cathode of Intermediate-Temperature Solid Oxide Fuel Cells Developed by Smart Self-Assembly. *Adv. Mater.* **2020**, 32, e1906979. <https://doi.org/10.1002/adma.201906979>.
270. Jia, X.; Lu, F.; Liu, K.; Han, M.; Su, J.; He, H.; Cai, B. Improved performance of IT-SOFC by negative thermal expansion Sm_{0.85}Zn_{0.15}MnO₃ addition in Ba_{0.5}Sr_{0.5}Fe_{0.8}Cu_{0.1}Ti_{0.1}O_{3-δ} cathode. *J. Phys. Cond. Matter* **2022**, 34, 184001. <https://doi.org/10.1088/1361-648X/ac4fe7>.
271. Minh, N.Q. Ceramic Fuel Cells. *J. Am. Ceram. Soc.* **1993**, 76, 563–588. <https://doi.org/10.1111/j.1151-2916.1993.tb03645.x>.

272. Fergus, J.W. Metallic interconnects for solid oxide fuel cells. *Mater. Sci. Eng. A* **2005**, 397, 271–283. <https://doi.org/10.1016/j.msea.2005.02.047>.
273. Hodjati-Pugh, O.; Dhir, A.; Steinberger-Wilckens, R. The development of current collection in micro-tubular solid oxide fuel cells—A review. *Appl. Sci.* **2021**, 11, 1077. <https://doi.org/10.3390/app11031077>.
274. Niewolak, L.; Tietz, F.; Quadackers, W.J. Interconnects. In *High-Temperature Solid Oxide Fuel Cells for the 21st Century: Fundamentals, Design and Applications*; Elsevier: Amsterdam, The Netherlands, 2015; pp. 195–254. <https://doi.org/10.1016/B978-0-12-410453-2.00007-5>.
275. Horita, T.; Xiong, Y.; Kishimoto, H.; Yamaji, K.; Brito, M.E.; Yokokawa, H. Chromium Poisoning and Degradation at (La,Sr)MnO₃ and (La,Sr)FeO₃ Cathodes for Solid Oxide Fuel Cells. *J. Electrochem. Soc.* **2010**, 157, B614. <https://doi.org/10.1149/1.3322103>.
276. Yang, Z.; Weil, K.S.; Paxton, D.M.; Stevenson, J.W. Selection and Evaluation of Heat-Resistant Alloys for SOFC Interconnect Applications. *J. Electrochem. Soc.* **2003**, 150, A1188. <https://doi.org/10.1149/1.1595659>.
277. Kofstad, P.; Bredesen, R. High temperature corrosion in SOFC environments. *Solid State Ion.* **1992**, 52, 69–75. [https://doi.org/10.1016/0167-2738\(92\)90092-4](https://doi.org/10.1016/0167-2738(92)90092-4).
278. Yang, Z.; Xia, G.G.; Stevenson, J.W. Evaluation of Ni-Cr-base alloys for SOFC interconnect applications. *J. Power Sources* **2006**, 160, 1104–1110. <https://doi.org/10.1016/j.jpowsour.2006.02.099>.

- 279.Zohrabian, V.M.; Sonick, M.; Hwang, D.; Abrahams, J.J. Dental Implants. Semin. Ultrasound CT MRI **2015**, 36, 415–426. <https://doi.org/10.1053/j.sult.2015.09.002>.
- 280.Hao, C.P.; Cao, N.J.; Zhu, Y.H.; Wang, W. The osseointegration and stability of dental implants with different surface treatments in animal models: A network meta-analysis. Sci. Rep. **2021**, 11, 13849. <https://doi.org/10.1038/s41598-021-93307-4>.
- 281.Panchal, M.; Khare, S.; Khamkar, P.; Bhole, K.S. Dental implants: A review of types, design analysis, materials, additive manufacturing methods, and future scope. Mater. Today Proc. **2022**, 68, 1860–1867. <https://doi.org/10.1016/j.matpr.2022.08.049>.
- 282.Nicholson, J.W. Titanium Alloys for Dental Implants: A Review. Prosthesis **2020**, 2, 100–116. <https://doi.org/10.3390/prosthesis2020011>.
- 283.Prathapachandran, J.; Suresh, N. Management of peri-implantitis. Dent. Res. J. **2012**, 9, 516. Available online: www.drj.ir (accessed on 13 November 2023).
- 284.Noyama, Y.; Miura, T.; Ishimoto, T.; Itaya, T.; Niinomi, M.; Nakano, T. Bone loss and reduced bone quality of the human femur after total hip arthroplasty under stress-shielding effects by titanium-based implant. Mater. Trans. **2012**, 53, 565–570. <https://doi.org/10.2320/matertrans.M2011358>.
- 285.Niu, L.; Dong, S.J.; Kong, T.T.; Wang, R.; Zou, R.; Da Liu, Q. Heat transfer behavior across the dentino-enamel junction in the human tooth. PLoS ONE **2016**, 11, e0158233. <https://doi.org/10.1371/journal.pone.0158233>.
- 286.Jacobs, H.R.; Thompson, R.E.; Brown, W.S. Heat Transfer in Teeth. J. Dent. Res. **1973**, 52, 248–252. <https://doi.org/10.1177/00220345730520021101>.

- 287.Li, S.; Chien, S.; Brånemark, P.I. Heat shock-induced necrosis and apoptosis in osteoblasts. *J. Orthop. Res.* **1999**, *17*, 891–899. <https://doi.org/10.1002/jor.1100170614>.
- 288.Eriksson, A.R.; Albrektsson, T. Temperature threshold levels for heat-induced bone tissue injury: A vital-microscopic study in the rabbit. *J. Prosthet. Dent.* **1983**, *50*, 101–107. [https://doi.org/10.1016/0022-3913\(83\)90174-9](https://doi.org/10.1016/0022-3913(83)90174-9).
- 289.Ormianer, Z.; Feuerstein, O.; Assad, R.; Samet, N.; Weiss, E.I. In vivo changes in dental implant temperatures during hot beverage intake: A pilot study. *Implant Dent.* **2009**, *18*, 38–45. <https://doi.org/10.1097/ID.0b013e318192e143>.
- 290.Froes, F.; Gungor, M.N.; Imam, M.A. Overview Titanium’s Expanding Market Cost-Affordable Titanium: The Component Fabrication Perspective. *JOM* **2007**, *59*, 28–31.
- 291.Anderson, B.J.; Justus, C.G.; Batts, G.W. Guidelines for the Selection of Near-Earth Thermal Environment Parameters for Spacecraft Design. **2001**. Available online: <http://www.sti.nasa.gov>. Accessed: 15 November 2023.
- 292.Ghidini, T. Materials for space exploration and settlement. *Nat. Mater.* **2018**, *17*, 846–850. <https://doi.org/10.1038/s41563-018-0184-4>.
- 293.Lu, G.Y.; Zhou, J.Y.; Cai, G.P.; Fang, G.Q.; Lv, L.L.; Peng, F.J. Studies of thermal deformation and shape control of a space planar phased array antenna. *Aerosp. Sci. Technol.* **2019**, *93*, 105311. <https://doi.org/10.1016/j.ast.2019.105311>.
- 294.Bhundiya, H.G.; Royer, F.; Cordero, Z. Engineering Framework for Assessing Materials and Processes for In-Space Manufacturing. *J. Mater. Eng. Perform.* **2022**, *31*, 6045–6059. <https://doi.org/10.1007/s11665-022-06755-y>.

295. Yu, B.; Xu, Z.; Mu, R.; Wang, A.; Zhao, H. Design of Large-Scale Space Lattice Structure with Near-Zero Thermal Expansion Metamaterials. *Aerospace* **2023**, *10*, 294. <https://doi.org/10.3390/aerospace10030294>.
296. Milward, S.S. Controlling Thermal Expansion with Lattice Structures Using Laser Powder Bed Fusion Laser Powder Bed Fusion Process Development. **2017**. Available online: <http://www.swansea.ac.uk/library/researchsupport/ris-support/>. Accessed: 18 November 2023.

2 Chapter 2 Additive Manufacturing of Steel Metamaterials with Low and Negative Thermal Expansion

Abstract

Steel is the most widely used alloy globally, and the development of negative thermal expansion (NTE) structures using steel could revolutionize industries by reducing dependence on rare naturally occurring low expansion materials, expensive low expansion alloys as well as reducing the need of heat shielding techniques in thermally intense applications. In this study, a thorough investigation was carried out on the material characterization, mechanical testing, structural design, numerical simulation, fabrication, and thermal assessment of NTE metamaterials produced through laser powder bed fusion (LPBF) of steel. The materials used for fabrication were AISI 304L Steel and SAE grade 300 Maraging Steel. The research began with an examination of the process-structure-property relationship to optimize processing parameters for improved interfacial strength between the two steels, assessing the microstructure, mechanical properties, and interfacial behavior. A series of uniaxial tensile tests, nano-hardness and scratch resistance measurements were conducted to evaluate mechanical properties across the interface, while scanning electron microscopy, energy-dispersive X-ray spectroscopy, and electron backscatter diffraction were utilized to explore interface formation mechanisms. Subsequently, various bimaterial NTE lattice structures were designed with a focus on thermal expansion performance and manufacturability using LPBF. Finite element simulations informed the selection of lattice designs, which were successfully fabricated via LPBF using the experimentally optimized interfacial process parameters. Finally, the thermal expansion performance of these metamaterials was evaluated using digital image correlation analysis, revealing eight different lattices exhibiting anisotropic contraction with increasing temperature, with dodecagonal bipyramid-based lattices achieving the best NTE performance.

Keywords: Steel; Additive Manufacturing; Negative Thermal Expansion; Lattice Structures;

Metamaterial.

2.1 Introduction

Materials and structures with negative and low thermal expansion are highly sought after in various cutting edge applications including precision instruments [1], biomedical [2], electronics [3], energy [4], and space [5]. Negative thermal expansion (NTE) mechanical metamaterials are structures which primarily utilize their architecture for achieving low coefficient of thermal expansion (CTE) rather than being fully dependent on compositional properties. This reduces dependence on materials with inherently low CTE like Invar and Kovar which are generally expensive and complicated to use in manufacturing processes e.g. machining [6], [7]. The architecture of NTE metamaterials usually incorporates at least two materials with significantly different CTEs. These materials are strategically arranged so that the expansion of one material counteracts the expansion of the other. NTE mechanisms can be categorized into bending-based and stretch-based systems. In bending-based architectures, differential expansion between the materials induces bending within the structure, resulting in overall contraction in one or more directions. Examples of such architectures include bimaterial strips, chiral structures, and re-entrant cells. However, bending-dominated designs tend to lose stiffness at elevated temperatures due to the bending of structural elements. To enhance the strength and stiffness of NTE structures, it is advantageous to avoid bending-dependent unit cells. Stretch-based architectures, which avoid bending, function based on the expansion of the compositional struts. In their work on foam topology, Deshpande et al. established a criterion for stretch-based designs, specifying that a minimum node connectivity of six is required for 2D structures and twelve for 3D structures [8]. Lattices that combine nodes satisfying and not satisfying this criterion may exhibit lower stiffness than fully stretch-based designs; however,

the resulting structure can still be classified as stretch-dominated. Therefore, stretch-dominated unit cells have been designed for consideration in this study.

Modern advances in multi-material metal additive manufacturing (AM) have tremendously increased the feasibility of producing these complex structures. Nevertheless, most of the NTE structures so far have been fabricated and tested using polymers and non-metallic materials [9], [10]. Despite primarily being a single material manufacturing technique, Laser Powder Bed Fusion (LPBF) has the potential to produce multimaterial metallic components [11], [12]. LPBF is a metal AM technology which utilizes laser power to selectively melt powder particles on a powder bed. In contrast to conventional manufacturing techniques, it offers greater flexibility in overcoming manufacturing challenges including shape complexity [13], material diversity [14], functional gradience [15] and thin wall fabrication [16]. In addition, LPBF provides higher resolution and shape accuracy when compared to other additive manufacturing techniques like directed energy deposition [17].

Limits also coexist in LPBF technology with abovementioned advantages, mainly slower production rates [18] and need for support structures in architectures with long overhangs and shallow angles [19]. Multimaterial fabrication using metal additive manufacturing introduces new challenges that must be addressed to achieve optimal parts. These include mutual insolubility of constituents [20], [21], significant differences in melting temperatures [21], [22], differential thermal stresses [23], [24], and formation of brittle intermetallic compounds [25], [26]. These phenomena can produce defects like cracks and pores, thereby even causing delamination [12], [27], [28]. Due to these reasons, not all materials are suitable for printing together via LPBF, with interfacial bond strength being crucial when joining dissimilar metals.

Energy density (E) in LPBF, calculated as $E = \frac{P}{v \times h \times t}$, where P is laser power, v is scanning speed, h is hatch spacing and t is layer thickness, is key to managing various factors [29]. Excessive energy density can cause melt pool splashing and surface roughness due to the balling effect, and it may also lead to keyhole porosity from metal vaporisation [30]. Insufficient energy density results in incomplete powder melting, leading to particle adhesion on contour tracks. Optimising energy density in multi-metal LPBF parts reduces defects, as seen in managing steel–copper bimetallic structures [31]. The differing thermal expansion coefficients and conductivities of steel and copper generate residual stresses, weakening bonds and causing interfacial cracking. Adjusting the scanning strategy, such as using island and interlayer staggered methods for SS316L and grade 300 maraging steel structures, also reduces residual stresses and the balling effect [32]. In CuSn and maraging steel 300 bimetallic structures, remelting scanning has been shown to reduce elongation and tensile stress [33].

In this study, AISI 304 grade stainless steel (SS) and SAE grade 300 maraging steel (MS) were used to fabricate bimaterial NTE lattices and were investigated for bonding compatibility as well as interface characterization. These two types of steels were selected for several reasons. Primarily, they have an appreciable difference in their CTE. Their similar compositions help prevent issues related to chemical incompatibility. Additionally, in the LPBF as-built state, MS outperforms SS in yield strength and hardness, creating a beneficial plasticity mismatch. Such mismatches are often found in various applications and are known to slow fatigue crack growth by influencing shielding effects near the material interface. Moreover, 300-series austenitic stainless steel is a common filler metal, used in many welding tasks due to its superior weldability, suggesting a likely strong bond between SS and MS.

In current study, primary objectives include:

1. To analyze the interfacial bond between SS and MS when printed vertically on one another, and to identify the optimal process-structure-property (PSP) parameters at the interface that maximize strength and minimize defects. While previous studies have explored different alloy combinations and reported distinct failure behaviors[10], [21], [34], there remains a gap in the literature regarding the interface between fully LPBF manufactured SS and MS. Notably, although Tan et al. examined the interface produced by depositing grade 300 MS on a conventionally manufactured AISI 304 steel block, no comprehensive study has yet addressed the fully LPBF-manufactured SS and MS interface. This research aims to fill that gap.
2. To assess the feasibility of producing NTE lattices by investigating maximum length of overhangs and minimum angle allowed for support free LPBF fabrication. Increasing the overhang length and reducing the strut angle relative to the build direction in support-free fabrication heightens the risk of delamination, warping, and build failure [35], [36]. Moreover, incorporating supports within lattice cells is generally not recommended due to the challenges associated with support removal post-printing [37], [38]. Additionally, in multimaterial lattices, the heat transfer characteristics vary due to the differing thermal properties of the alloys involved, which influences the overhang and angle limitations differently compared to single-material designs. Therefore, understanding these limitations is essential.
3. To compare finite element analysis (FEA) results with experimental testing of the thermal expansion of the fabricated structures. This comparison will evaluate the feasibility of designing and analyzing such NTE structures without the need to test every individual

structure created using these two alloys. This is particularly important because LPBF-produced materials exhibit variations in properties compared to conventionally manufactured materials, which are typically used in FEA simulations. Furthermore, the mechanical and thermal properties of the interface, as well as its thickness, are not precisely known at this stage. However, simulations often assume a sharp, ideal and defect-free interface. Therefore, a comparative study is necessary.

In this study, we developed bimaterial lattices using metal additive manufacturing with AISI 304 SS and SAE 300 MS exhibiting NTE behaviour. Initially, material and mechanical characterization experiments were carried out to ensure the fabrication of a defect-free bond between the two alloys. Subsequently, lattices were designed using these materials and their thermal performance was assessed through finite element simulations. The lattices were then fabricated using LPBF to evaluate the feasibility of the design in practical fabrication. Finally, thermal expansion experiments were conducted to assess the thermal expansion performance and compare the results with those from numerical simulations.

2.2 Experimental Details

2.2.1 Materials and Machine

For utilization in LPBF manufacturing, gas-atomized MS1 maraging steel powder (MS) was supplied by EOS GmbH, while SS 304L powder (SS) was supplied by Carpenter Additive (Philadelphia, US). The MS and SS powder particles had diameters ranging from 15 μm – 45 μm . The chemical composition of the two powders is presented in Table 2.1.

Table 2.1 Elemental composition of feedstock powders

MS 1 Maraging Steel									
C	Ni	Co	Mo	Ti	Al	Cu,Cr	Mn,Si	P,S	Fe
≤0.03	17-19	8.5-9.5	4.5-5.2	0.6-0.8	0.05-0.15	≤0.5	≤0.1	≤0.01	Bal.
SS 304L Stainless Steel									
C	Cr	Ni	Mn	Si	P,S	Fe			
≤0.03	18-19.5	8-10	0.5-2	0.66	≤0.04	Bal.			

EOS M280 DMLS machine, located at McMaster University, was used for LPBF fabrication.

The machine is equipped with a 400W Yb-fiber with a 100 μm spot size, maximum power of 400 W, laser wavelength of 1070 nm and features a build platform with dimensions of 250mm × 250mm × 325mm. Throughout the process, the powder bed was maintained at a constant temperature of 40°C. Argon gas was used throughout the process to shield the material from oxidation and the oxygen content was maintained below 0.1% for the entire procedure.

Using abovementioned materials and machine, the fabrication of samples can be categorized in two stages:

- Fabrication of solid samples for material characterization and mechanical testing.
- Fabrication of multimaterial lattices.

2.2.2 Fabrication of Solid Samples

In the first stage, solid specimens were manufactured for material characterization and mechanical testing purposes. After investigation of optimum parameters for each material, specimen with interface between the two materials were fabricated for analysis whose details are mentioned in this section.

2.2.2.1 Material Characterization Samples

The samples for material and interface characterization were designed as shown in figure 2.1(a).

Initially, optimal process parameters for SS and MS were determined separately. These parameters were then used as the basis for creating a design of experiments to find the best process variables for the interface. For all samples in this work, including multimaterials, the layer thickness was kept 40 μ m and as part of the scanning strategy, a 67° rotation of scan lines was applied every new layer.

For bimaterial coupons with a single interface, the fabrication process was paused halfway through the sample height. At this stage, the SS powder was removed, the build chamber thoroughly cleaned, and MS powder loaded. The building process then resumed, applying the interface processing parameters for five layers before using the optimal MS parameters for the remainder of the height.

2.2.2.2 Mechanical Characterization Samples

Tensile test samples were printed as cylinders with a total height of 60mm (figure 2.1(b)). The manufacturing process began by printing SS for the first half of the sample's length. Subsequently, the powder was changed to MS1, and interfacial process parameters were applied based on the expected interface thickness derived from material characterization samples. Finally, the process variables were adjusted to the optimal parameters for MS to complete the remaining height of the specimen. Finally, the test samples were machined to 5mm gauge diameter as per ASTM E8 standard for uniaxial tensile testing [39]. For nano-hardness and scratch tests, samples identical to material characterization specimen were fabricated and sectioned vertically in the center.

2.2.3 Material Characterization

For interfacial metallurgical analysis, specimens were sectioned across the interface along the build direction, then polished and examined using a Keyence VHX5000 optical microscope

(OM). For melt pool analysis and morphological investigation, samples were etched using 5% Nital reagent (5 cm³ HNO₃ and 99 cm³ Ethyl alcohol) for 3 minutes and analyzed using Nikon LV500 OM and Vega Tescan scanning electron microscope (SEM). Elemental distribution across the interface was analysed with EDS detector equipped in the Vega Tescan SEM. Grain orientation and phase distribution in the interfacial regions were determined using electron back-scattered diffraction (EBSD). EBSD was performed on interface as well as single constituent regions on an FE Versa 3D field-emission scanning electron microscope (FE-SEM), using a step size of 0.05-0.5 μm, and the data were collected and analyzed using the TSL OIM 7 and HKL Channel 5 software package respectively.

2.2.4 Mechanical Testing

Tensile, nano-hardness and scratch resistance test was performed to mechanically investigate the interface characteristics. The tests were performed at Tensile Testing Metallurgical laboratory (Cleveland, OH, USA) and loading conditions were kept as specified in ASTM E8 for steel [39]. Three identical samples were tested for each combination of processing parameters. The nano-hardness at the interface was assessed using an Anton Paar NHT³ nanoindentation platform in accordance with the ISO standard 14577 [40]. A Berkovich diamond indenter tip was used with linear loading, applying a maximum load of 40 mN and a loading and unloading rate of 80 mN/min. Nine indentations were performed across the interface, with each indentation spaced 25 μm apart. The scratch test was conducted using an Anton-Paar Revetest scratch tester with a Rockwell Diamond indenter of tip radius 200 μm. The test was performed under a constant load of 10 N, with a scratch rate of 2 mm/min and a scratch length of 3 mm, in accordance with the ASTM C1624-05 standard [41]. The sliding contact response was analyzed across the interface based on penetration depth and acoustic emission.

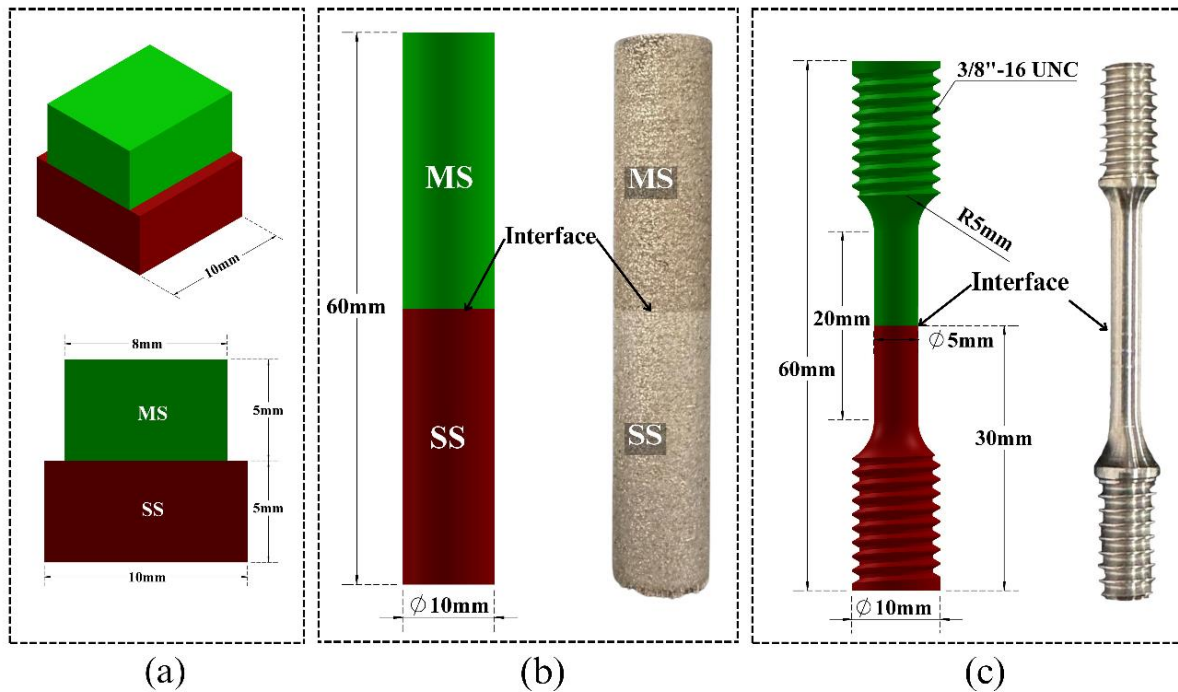


Figure 2.1 (a) Specimen used for OM, SEM, Nano-hardness and scratch testing
(b) Tensile Test Specimen after printing (c) Tensile Test Specimen after machining

2.2.5 Lattice Structures

To develop lattices, the design field was initially evaluated by identifying various constraints and areas of flexibility. For optimal fabrication and performance, the metamaterial lattice designs must satisfy the following requirements:

- Be manufacturable using Laser Powder Bed Fusion (LPBF).
- Achieve a negative net coefficient of thermal expansion (CTE) in at least one direction.

The first criterion imposes several implicit restrictions due to the nature of the LPBF process and the specific machine used:

- The composition must remain uniform within the horizontal plane, with material variation only

in the vertical direction.

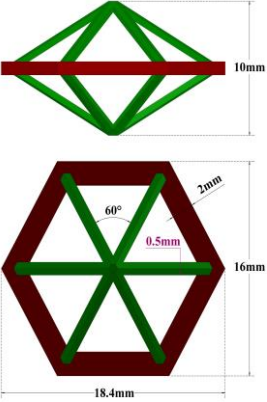
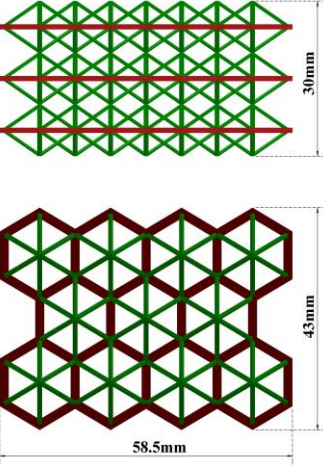
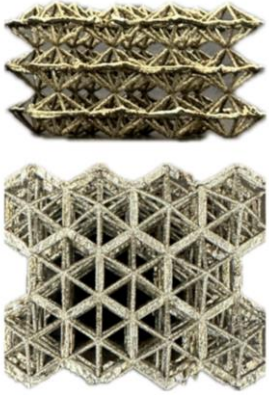
- Support structures cannot be utilized, as their removal from within the lattice is exceedingly challenging.
- Long overhangs are to be avoided due to the absence of supports, which could otherwise result in build failure.

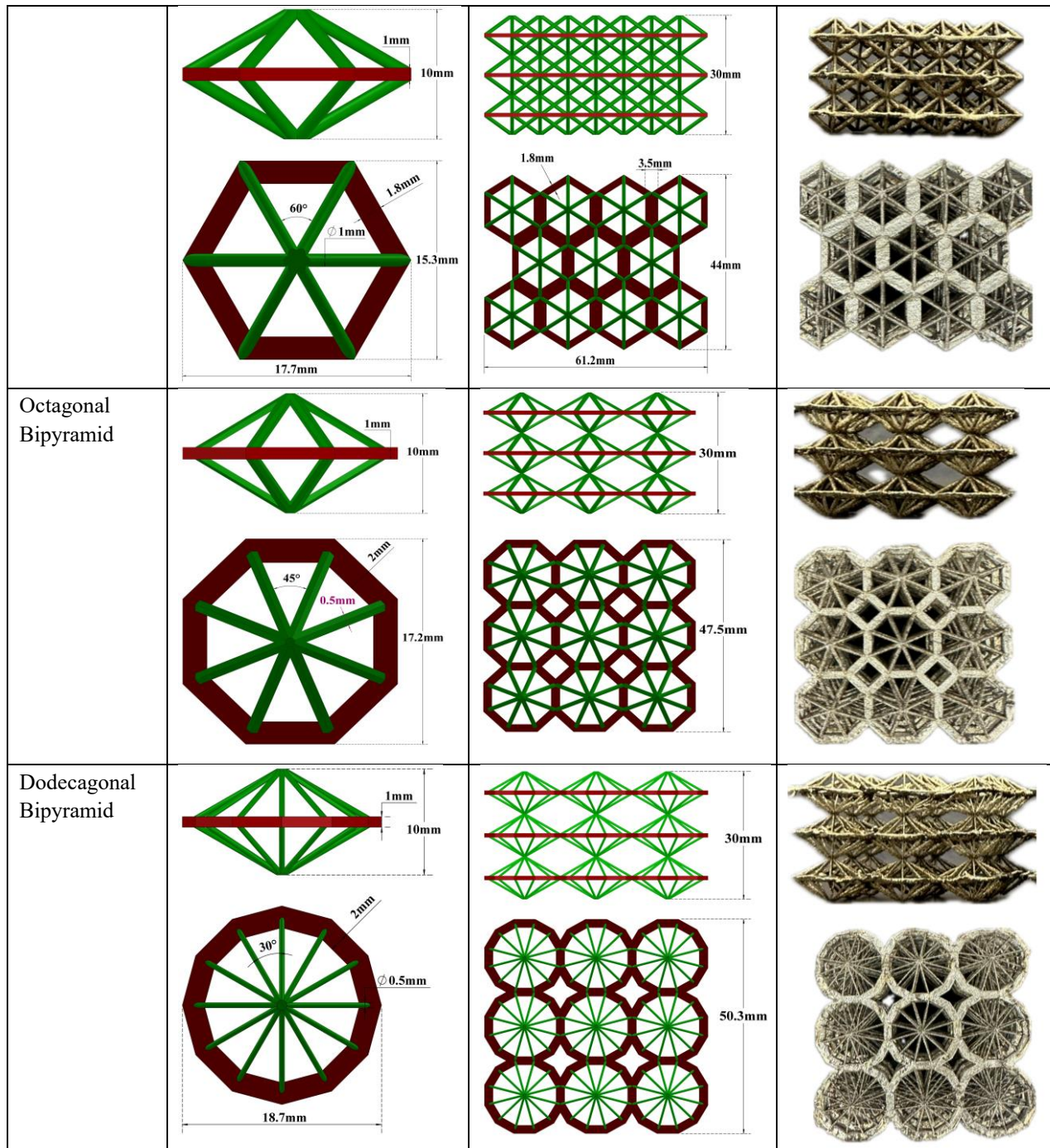
Four distinct lattices were created as shown in table 2.2 based on three unit cell types, each with location-specific constituency. The unit cell of each lattice is based on a bipyramid, which is generated through the tegum product. The tegum product is a geometric concept from polytope theory that generalises polygons and polyhedra to higher dimensions. It involves taking the Cartesian product of the vertices of two polytopes and forming the convex hull of the resulting set [42]. It ensures that every vertex of one polygon connects to every vertex of the other. Tegum product of two polygons (2D) creates a polytope, also called a bipyramid (3D). For instance, applying the tegum product to a line segment and a hexagon yields a hexagonal bipyramid. Similarly, octagonal and dodecagonal bipyramids are created. The three unit cells used in this study were created by taking motivation from hexagonal bipyramid, octagonal bipyramid, and dodecagonal bipyramid.

To create the lattice structure, a specific unit cell was arranged in a horizontal 4×4 grid to form a single layer. Three such layers were then stacked vertically, resulting in a $4 \times 4 \times 3$ lattice configuration. All unit cells have a height of 10mm, therefore all lattices measure 30mm vertically. Two different lattices were constructed using a hexagonal bipyramid-based unit cell, while one lattice each was created using octagonal and dodecagonal bipyramid cells. The two hexagonal lattices differ in strut thickness and cell spacing. The struts composed of the higher CTE material (SS) are shown in red, while those made of the lower CTE material (MS) are

depicted in green (Table 2.2). The vertical direction in the top view, which is also the direction of the building process, indicates where material variation occurs vertically, with the composition remaining consistent within the horizontal plane at any given location vertically. The octagonal and dodecagonal lattices alongwith one of the hexagonal lattices have MS struts of thickness 0.5mm while SS struts are thick. Another hexagonal lattice has 1mm thick MS struts. This allows for the understanding of both structure and strut thickness on NTE performance as well as printability of the designs.

Table 2.2 Metamaterial unit cells and lattice designs used in this study. SS and MS struts are shown in red and green colours respectively.

Type	Unit Cell	Lattice Design	Printed Structure
Hexagonal Bipyramid			



2.2.6 Expansion Simulations

The thermal expansion of the lattices was simulated using the Static Structural module in ANSYS Simulation Software (ANSYS, Inc., PA, USA). The material properties of the alloys used in the numerical simulations are detailed in table 2.3. The variation in CTE and thermal

conductivity with temperature was accounted for by using temperature dependent values provided by ANSYS Granta Pack. The model was discretized using tetrahedral solid elements of quadratic order. As in figure 2.2 for lattice simulations, the boundary conditions were applied as follows:

- The bottom face of central unit cell of lowest stack of lattice was fixed.
- The remaining unit cells in the lowest stack had their bottom faces free to move horizontally (X, Y – displacement = free) but were constrained from any vertical movement (Z-displacement = 0 mm).
- The rest of the lattice was free to expand.
- The temperature of the whole lattice was increased from 22°C to 300°C.

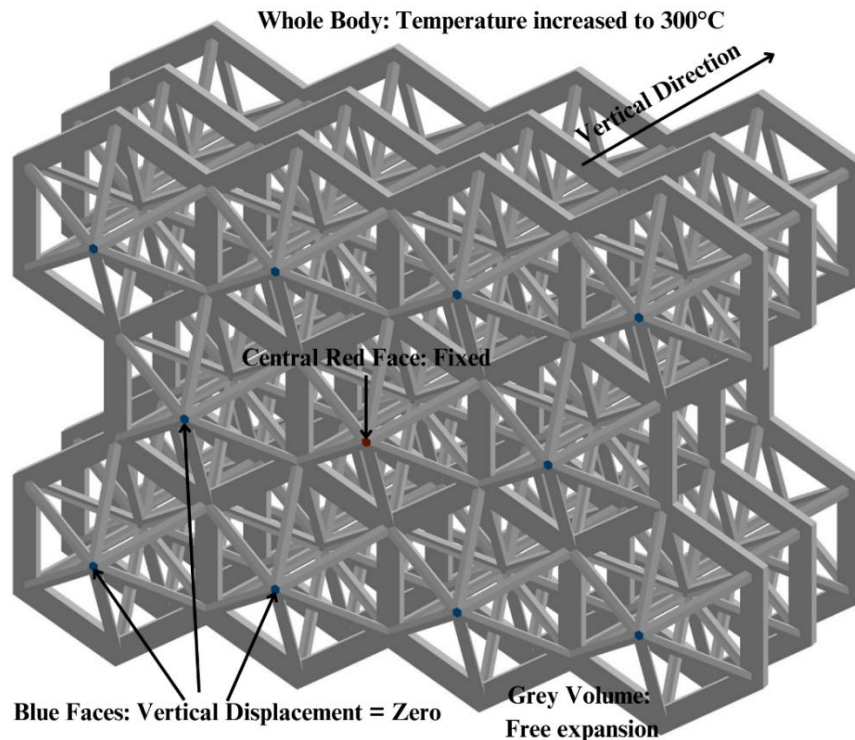


Figure 2.2 Boundary Conditions for finite element analysis.

After conducting a mesh sensitivity analysis on the hexagonal bipyramid unit cell with fixed

bottom face, focusing on net vertical contraction, an element size of 0.3 mm was determined to be suitable and was used for the FEA of full lattice structures.

Table 2.3 Properties of SS and MS as used in FEA simulations.

Alloy	Young's Modulus (GPa)	CTE (at 20°C) ($\times 10^{-6}$) (m/m°C)	Thermal Conductivity (at 20°C) (W/m.K)	Yield Strength (MPa)	Tensile Strength (MPa)
SS	196	15.6	15.8	202	533
MS	188	9.5	14.9	1900	1965

2.2.7 Fabrication of metamaterial lattices

Optimal parameters for both materials and their interfaces were used to fabricate metamaterial lattices. The alloy variation took place at fixed heights according to the change of alloys in lattice design, requiring the manufacturing process to pause and the powder in the machine to be replaced (figure 2.3). The swapping of powders was carried out six times, excluding the initial loading and final removal of the powder after fabrication.

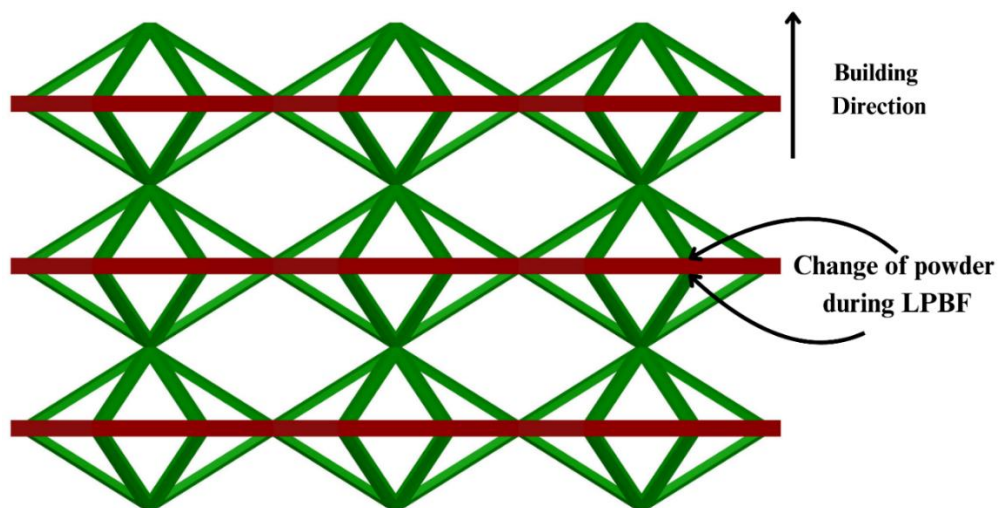


Figure 2.3 Change of alloys during fabrication of bimaterial lattices

2.2.8 Thermal Expansion Testing

The thermal expansion behavior of the lattices was experimentally investigated using digital image correlation (DIC) analysis. The temperature of the samples was increased from 25°C to 300°C within an enclosed furnace. Both heat-treated and non-heat-treated samples were examined. The heat treatment process before testing involved a stress relief procedure, during which the temperature was raised to 300°C at a rate of 100°C every hour, soaking period of 2 hours and cooling in air. For thermal expansion testing using DIC, the temperature was increased from 20 °C to 300°C at the rate of 1 °C every three seconds. The resolution of the entire setup was 0.005mm. Vic-3D DIC system by Correlation Solutions Inc. (South Carolina, USA) was used for strain and deformation measurement with two cameras fitted with polarizers for deformation measurement. The highest priority was given to measurement of deformation in the expected direction of NTE.

2.3 Results and Discussion

2.3.1 Interfacial Process Optimization

A strong, porosity-free bond at the interface between the two materials is crucial for most industrial applications of bimaterial structures, including lattices. In the first stage, investigation of optimum parameters was conducted for each material individually. Literature suggests a range of optimal energy density (energy supplied by laser per unit volume of powder) of 65-95 J/mm³ for grade 300 maraging steel [43], [44], [45]. We conducted an experimental study to identify the precise value within this range, revealing that an energy density of 64.2 J/mm³ produced the highest density parts ($\rho > 99.6\%$). This finding is closely aligned with the 67.47 J/mm³ energy density reported by Tan et al. [44]. For SS, our experiments found that an energy density of 62.5 J/mm³ resulted in the most optimal part density ($\rho > 99.6\%$), which aligns with the observations by Hou et al. [46]. The optimum process parameters observed for each

constituent are mentioned in table 2.4 with density measurement charts in figure 2.4.

Table 2.4 Optimum process parameters for alloys found in this study

Material	Hatch Spacing (μm)	Laser Power (W)	Scanning Speed (mm/s)	Energy Density (J/mm^3)
Maraging Steel 300	110	260	920	64.2
Stainless Steel 304L	80	220	1100	62.5

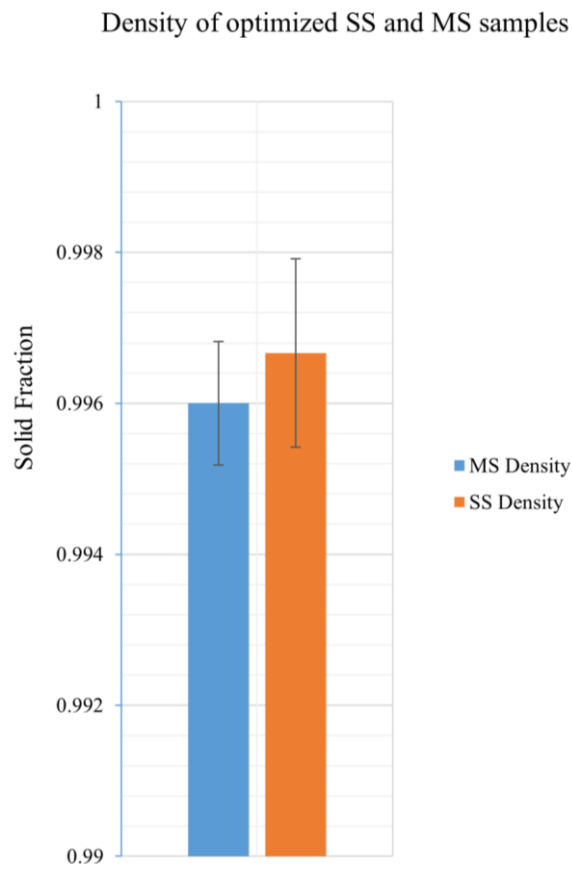


Figure 2.4 Density of optimized SS and MS samples

In the second stage, experiments were conducted to determine the optimal parameters for the interface. To assess the impact of processing parameters on interfacial porosity and mechanical properties, the utilized design of experiments matrix is shown in table 2.5. Observing that MS had a slightly higher optimal energy density required, its optimal process variables were used as the baseline, with variations introduced accordingly. Due to its lower energy requirement per unit volume for melting, SS was printed first, followed by the deposition and melting of MS powder on top using the combination matrix parameters where hatch spacing was kept constant at 110 μm .

Table 2.5 Design of experiments matrix used for identification of optimum process parameters for the interface

Sample No.	Laser Power (W)	Scanning Speed (mm/s)	Energy Density (J/mm^3)
Variation in Scanning Speed			
1-S	260	520	114
2-S	260	620	95
3-S	260	720	82
4-S	260	820	72
5-S	260	920	64
6-S	260	1020	58
7-S	260	1120	53
8-S	260	1220	48
9-S	260	1320	45
Variation in Laser Power			
1-L	185	920	46
2-L	200	920	49
3-L	215	920	53
4-L	230	920	57
5-L	245	920	61
6-L	260	920	64
7-L	275	920	68
8-L	290	920	72
9-L	305	920	75

10-L	320	920	79
11-L	335	920	83
12-L	350	920	86

The optical microscopy (OM) analysis of the polished cross-sections of the printed coupons, as shown in figure 2.5 and figure 2.6, demonstrates that both low and high energy densities lead to an increase in porosity defects. These defects result in a mechanically weaker bond. On the other hand, moderate energy densities produce a significantly stronger interface with minimal interfacial pores. Importantly, none of the samples displayed any cracks. It was also observed that lower energy densities result in a much higher number of pores compared to higher energy densities. Furthermore, the findings indicate that optimal energy densities and processing parameter combinations form a spectrum, rather than being limited to one or two specific values. All specimens within the dotted lines in figure 2.5 and figure 2.6 show an optimal interface according to the optical analysis.

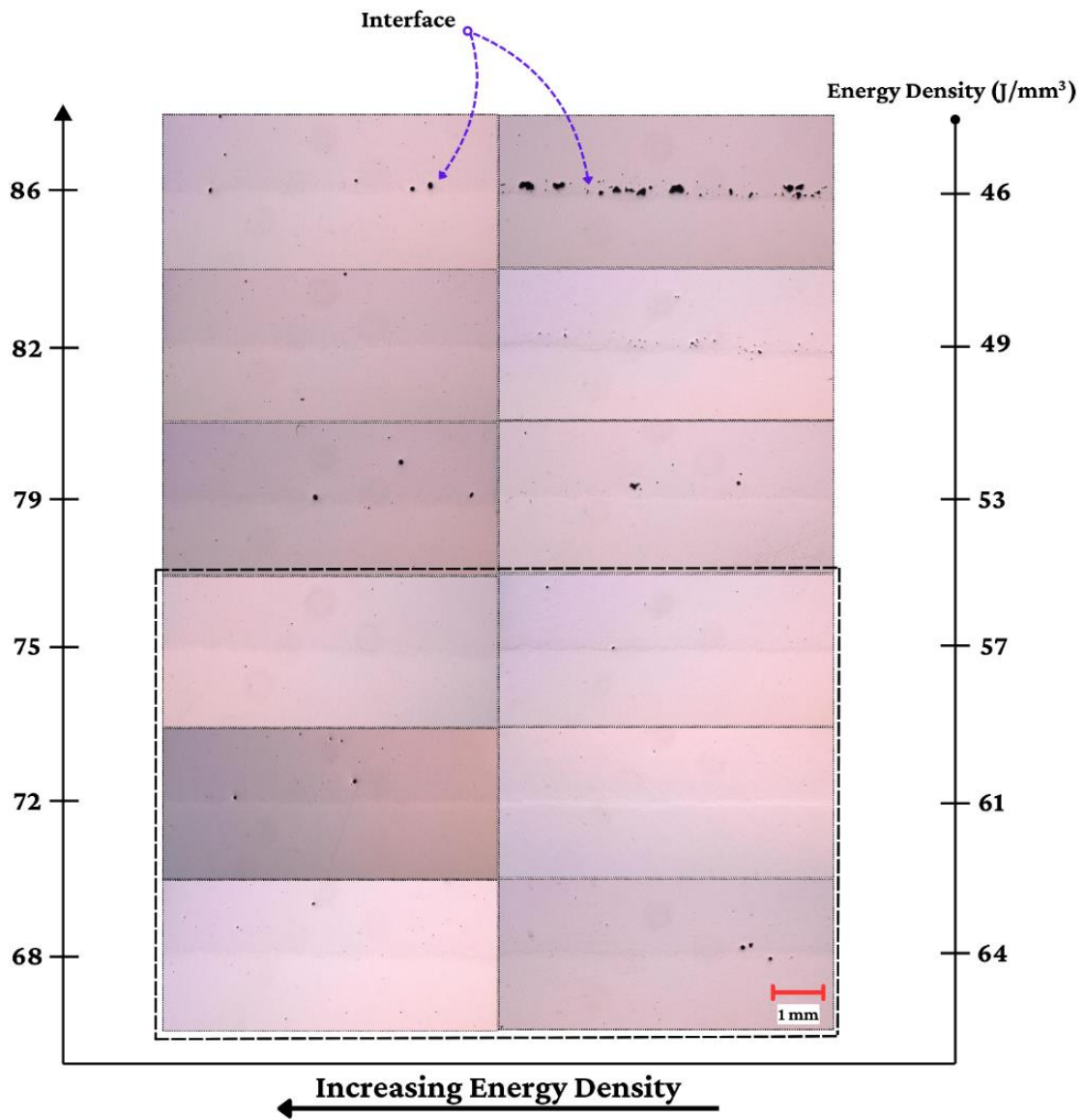


Figure 2.5 Optical microscopy images of various samples fabricated for optimum PSP identification for the interface with variation of scanning speed as per design of experiments matrix. The samples within dotted enclosures are identified to be optimum.

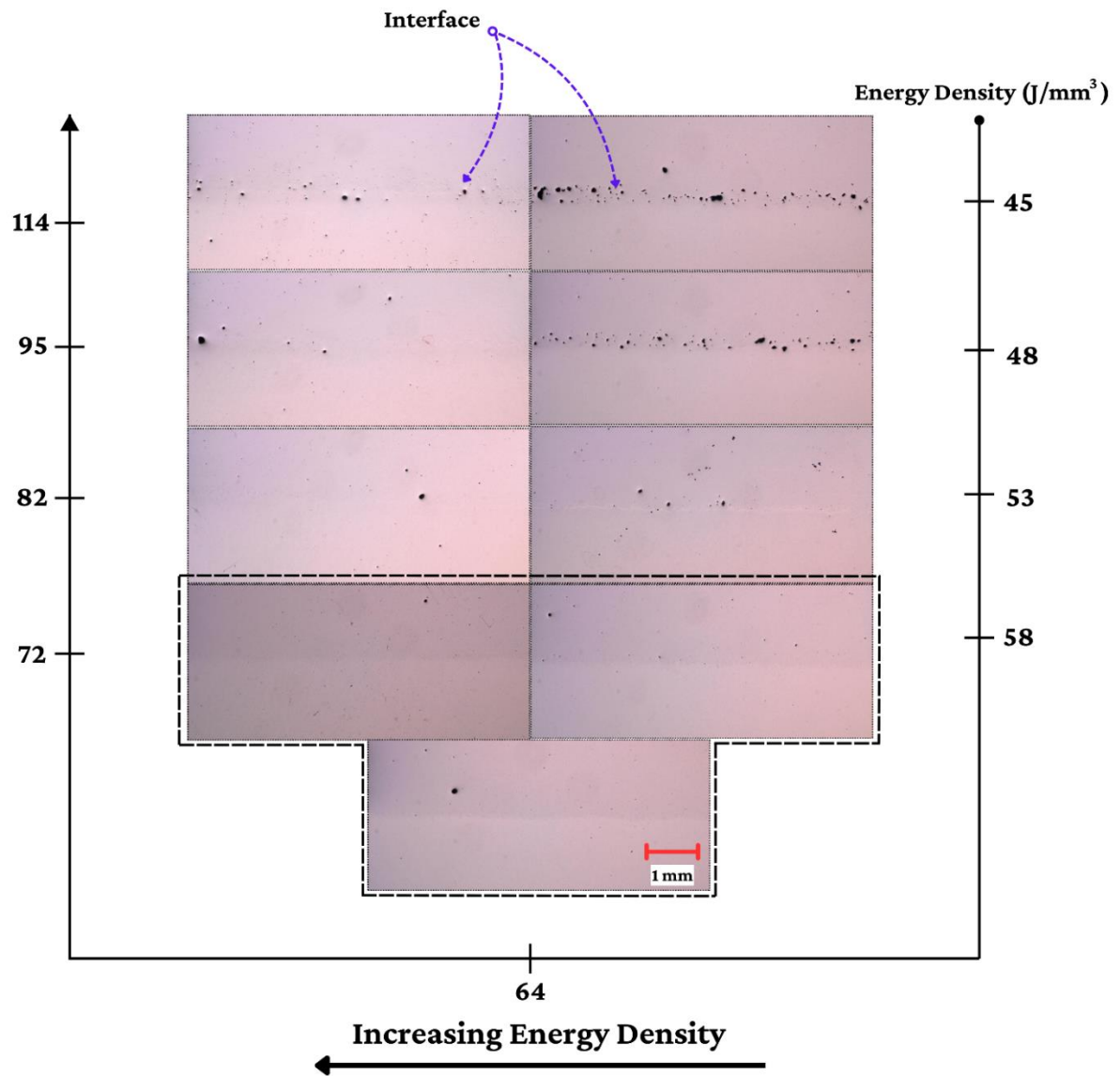


Figure 2.6 Optical microscopy images of various samples fabricated for optimum PSP identification for the interface with variation of laser power as per design of experiments matrix. The samples within dotted enclosures are identified to be optimum.

2.3.2 Interfacial Microstructural Analysis

The interfacial morphology of multimaterials fabricated using optimal processing parameters is observed using optical and scanning electron microscopy (SEM). Figure 2.7 shows images

along a cross-section plane in the center with its normal perpendicular to the building direction. The cross sections of the scan tracks show melt pools with depths of 80-100 μm . Visual observations indicate an inter-diffusion zone of thickness 150-200 μm at the interface encompassing two to four melt pools vertically. No visible defects are observed at the interface. The interfacial contact is characterized by circulatory flows which tend to mix the two constituents in the diffusion zone, thereby strengthening the connection. This circulation in the melt pools is caused by Marangoni convection and is depicted in figure 2.7(c). The Marangoni effect induces liquid movement on the melt pool surface from areas of low surface tension to those with high surface tension. Typically, metals and alloys exhibit a negative temperature coefficient of surface tension, leading to outward convection, where the melt pool flows from high-temperature to low-temperature regions [47]. Therefore, in a melt pool the Marangoni flow generally happens from the hottest location i.e. the point of laser impingement to the periphery of the melt pool.

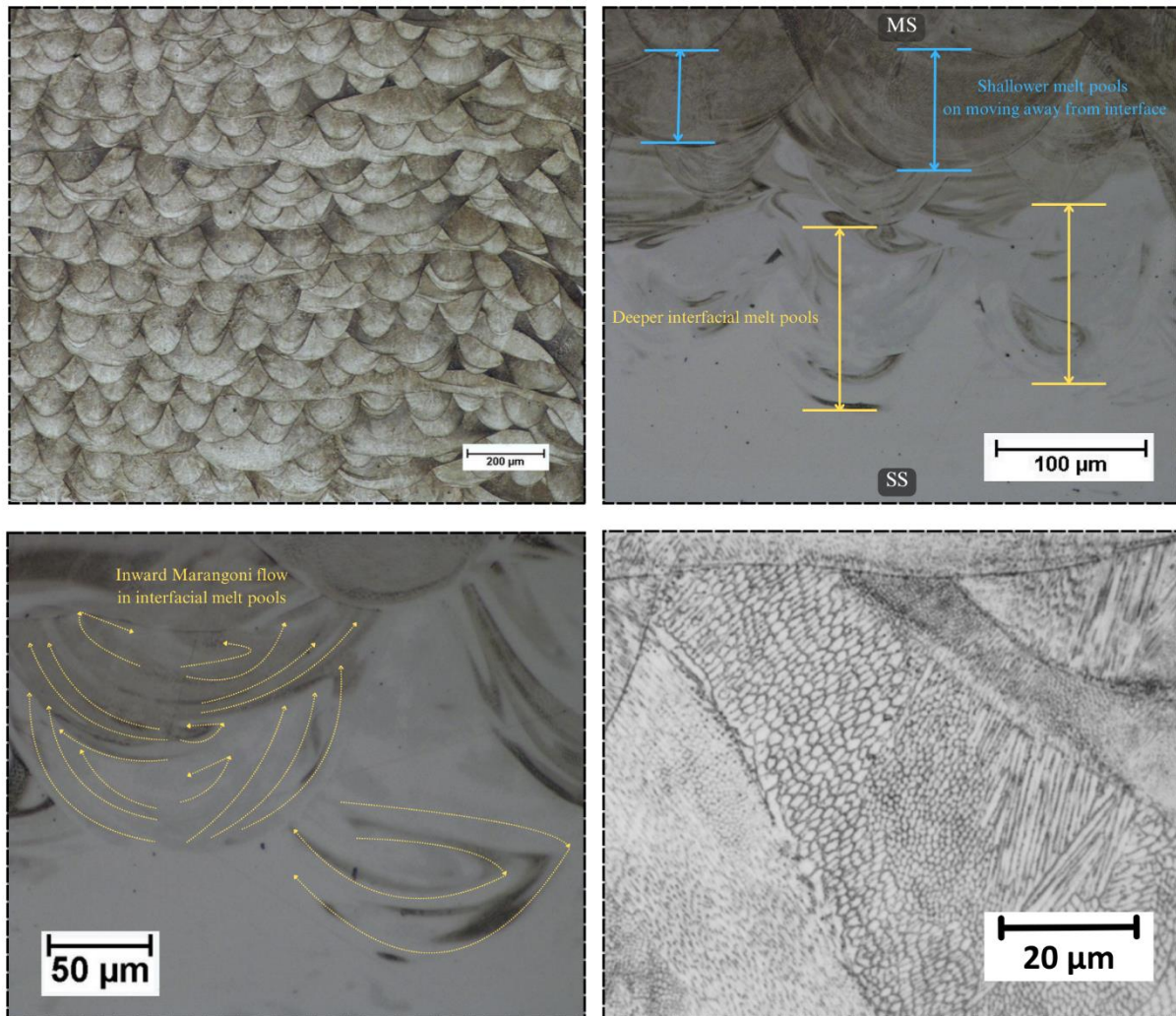


Figure 2.7 Optical microscopy images (a) Melt pools as observed in maraging steel region; (b) Difference in melt pool depth at interface and bulk maraging steel; (c) Inward marangoni flow in melt pools at the interface; (d) Grain structure of maraging steel.

Interestingly, the melt pools observed at the interface are slightly deeper than melt pools of single material MS. This can be explained by inward Marangoni flow in this case contrary to outward Marangoni flow generally reported in laser AM [48], [49]. Experimental investigations in the field of welding have shown that high sulphur steel melt pools exhibit flow in the opposite direction (inward) compared to low sulfur steels [50], [51]. This inward flow can happen due to

small changes in surface-active elements in the molten metal. Studies have found that sulphur levels above 0.003 wt% in steel can cause inward flow. SS powder used in this study has around 0.04 wt% Sulphur which exceeds the critical concentration (Table 2.1). The melt pool at the interface comprises of both steels, with Sulphur concentration becoming higher due to infusion of SS in the molten mix. The high levels of sulfur from SS likely caused the surface tension to increase with temperature. Thus, the hottest liquid metal near the laser impingement point moves downward, increasing the heat load and causing further melting of the previously deposited layers at the bottom. This results in a higher depth-to-width ratio of the melt pool at the interface. Also, embedment of MS in bottom SS leads to a gradient-like composition and better mixing, thereby increasing the bond strength.

High resolution SEM micrographs are shown in figure 2.8. The microstructure of MS comprises of cellular solidification structures which are a result of high cooling rates and fast solidification speeds. The cooling rate can be approximated using the equation $\lambda_{DAS} = CR^{-0.33}$ [52]. Using minimum and maximum dendrite arm spacings of 0.5 μm and 2 μm as observed from figure 2.7, the cooling rate varies from 4.78×10^6 K/s to 7.16×10^4 K/s. In addition, columnar cells and acicular structures are also present in the microstructure. These morphological variations are a result of interplay between temperature gradient and growth rates, which vary within and locally across the melt pools [53]. The observed geometry of the solidification cells (whether cellular or dendritic) can also be influenced by the cutting angle. As reported by Kürnsteiner et al. [54], cellular cells appear elongated when cutting occurs at an angle. Compared to the MS microstructure, the embedded MS region within the SS at the interface, as depicted in figure 2.8(c), shows a similar structure. It features melt pools with both coarse and fine cellular forms, as well as acicular cells of submicron size. Interestingly, the boundary of entrapment of MS

withing SS consists of partially melted powder which seems to be nucleation sites of MS grains. The linear distribution of elemental composition across the interface was investigated using Energy Dispersive Spectroscopy (EDS). As mentioned in table 2.1, the primary alloying elements in SS are Ni, Cr, Mn and Si while those in MS are Ni, Co and Mo. The variation of concentrations of these elements is depicted in figure 2.9. The line was segmented into over 500 points along a total length of 200 μm , with the concentration of each element measured at each location. It's crucial to note that all values were normalized to effectively highlight the trends. The normalization equation employed was:

$$N_c = A_i/A_{max}$$

Where A_i is the concentration of the element at the point i while A_{max} is the maximum concentration of the element on the line.

On top, the composition has minimal concentrations of Co and Mo and other elements are in the range of nominal composition of SS. As location varies downward across the interface, the alloying elements of SS decrease while those of MS gradually increase. This results in a buffer zone where the elements of both SS and MS coexist, indicating chemical intermixing between the two steels. The transition zone spans approximately 150 μm , defining the interface thickness. Consequently, the chemical composition at the interface is not purely MS or SS but a blend of both alloys, forming a sharp gradient around four powder deposition layers thick.

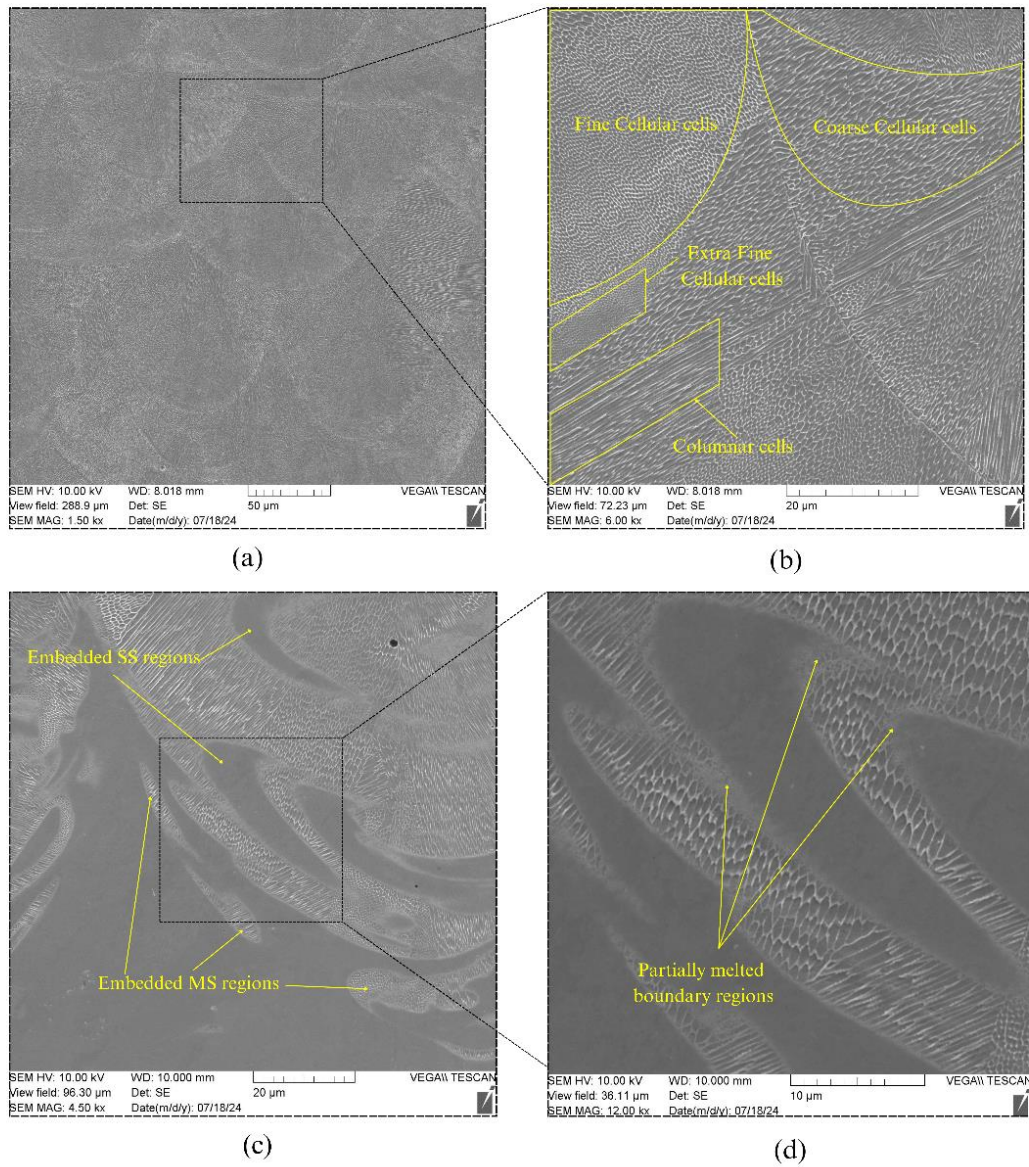


Figure 2.8 Scanning Electron Microscopy images: (a) Melt pools in maraging steel (b) Microstructure of maraging steel (c) Entrapments in interfacial region (d) Partially melted boundary between two alloys at the interface

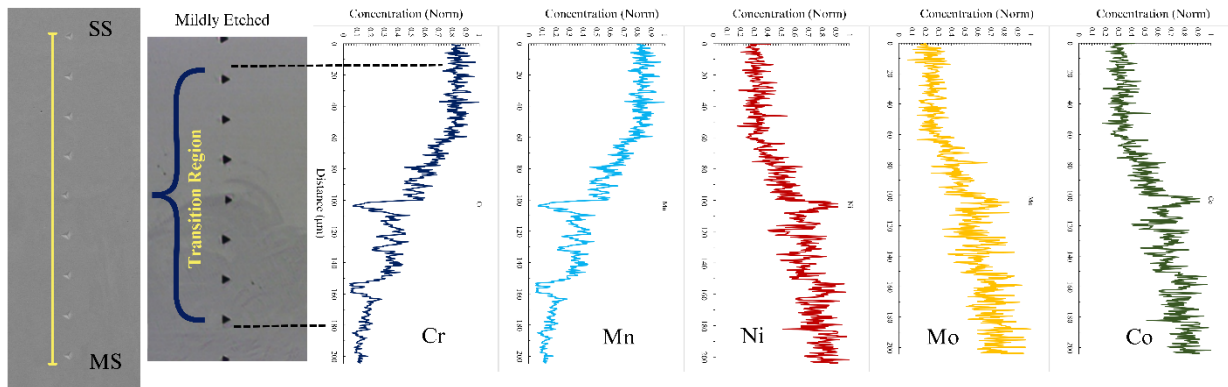


Figure 2.9 Alloying element distributions across the interface using linear EDS analysis.

2.3.3 Interfacial Crystallographic Analysis

Electron Backscatter diffraction (EBSD) analysis was used to investigate grain morphology of bimaterial samples and their interface. Figure 2.10 illustrates the microstructure of the interface as well as bulk constituents on either side. The coarse and fine grain sizes of SS and MS respectively, mark a clear distinction between the two constituents. SS microstructure consists of columnar grains elongated towards the build direction with a fully austenitic composition. The extremely high cooling rate during LPBF prevents ferrite from having enough time to nucleate and grow at the austenite grain boundaries, resulting in a microstructure composed entirely of the austenite phase. This contrasts with microstructure produced by conventional manufacturing which consists of cellular ferrite distributed within an austenitic grain structure [55].

The MS grain morphology consists of cellular and columnar grains with a predominance of the former. The columnar grains show slight deviation from the build direction. This is attributed to local dependence of heat gradient during solidification both inside and outside the melt pools. The microstructure is hierarchical, where martensite lath structures are observed as intragranular

features while cellular cells are formed on a bigger scale. The lath structures roughly align perpendicular to melt pool boundaries, along the thermal gradient. The correlative phase distribution map (PDM) in figure 2.10(b) reveals small amounts (~3%) of retained austenite in distributed in a predominantly martensitic (α -Fe) microstructure. Since reverted austenite formation is based on diffusion [56], rapid cooling rates of LPBF leads to suppression of reverted austenite formation as compared to conventionally manufactured maraging steels [57]. Texture is absent in the IPF because MS grain orientations vary with location, attributed to the 67° rotating laser scan strategy implemented in this study.

The microstructure at the interface demonstrates a seamless bond between the two steels. The initial layer of MS, which solidifies atop the printed SS, presents an exceptionally fine microstructure, a characteristic also observed in the circular sections of MS encapsulated within the SS region at the interface. This occurrence results from the SS section cooling during the powder swap, enabling rapid heat transfer. With the deposition of successive layers, a gradient in MS grain size develops, increasing due to the elevated temperatures of the previously deposited layers. The elongated grains of SS maintain their columnar structure and epitaxial growth through the interface before MS grains gradually take over.

Kernel average misorientation (KAM) measures the average misorientation around a measurement point relative to all its nearest neighboring points. In this context, the local misorientation is determined from the center of a specific grain to all points around the kernel's perimeter [58]. KAM analysis is generally used to understand localized deformation, local lattice distortions, and areas with high dislocation density, which indicate stored strain energy within the grain [59]. For example, deformed grains exhibit higher KAM values due to increased dislocation density. A KAM map of the interface, shown in figure 2.10(d), is used to characterize

the micro-strain. It is evident that the micro-strain at the interface is greater than that in the bulk SS but comparable to the MS side. However, the regions where MS is embedded within the SS exhibit higher inherent micro-strain values compared to both the SS and MS sides. These observations lead to two conclusions: firstly, LPBF-manufactured MS tends to have higher residual stresses than powder bed-fused SS; and secondly, the encapsulated MS-dominated grains experience increased strain due to the surrounding SS-dominated grains. This is primarily attributed to differences in crystallographic sizes, orientations, thermal properties, and mechanical properties of the two constituents.

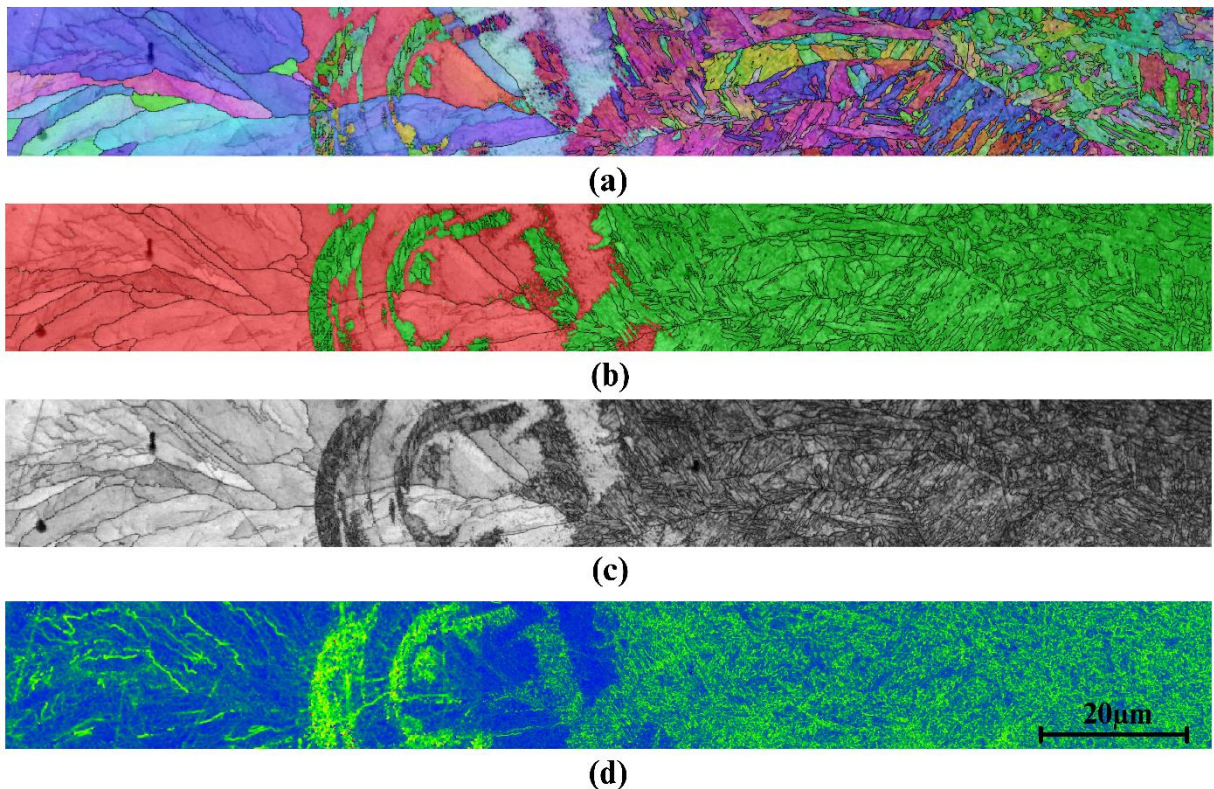


Figure 2.10 Interfacial Electron Backscatter Diffraction data (a) Inverse Pole Figure – Z Map; (b) Correlative Phase Distribution Map ;(c) Band Contrast Map; (d) Kernel Average Misorientation Map

2.3.4 Mechanical Performance Analysis

Tensile tests were performed on the optimum samples identified through optical investigation in Section 3.1 to further assess the interfacial strength. Standard tensile samples were prepared according to the ASTM E8 standard, as depicted in figure 2.1, for testing. The samples fractured on the SS side, well away from the interface, indicating that the interfacial bond strength surpasses that of the SS. This supports the concept of gradual mixing and bonding affinity between the two alloys, which enhances the bond strength due to the dissolution of MS into SS at the interface. The observed elongation is primarily attributed to plastic deformation in the SS, as the MS possesses significantly higher strength. All the samples identified as optimum using OM in figure 2.5 and 2.6 fractured away from the interface with similar tensile strength, which closely matches the tensile strength of LPBF fabricated 304L grade SS [60]. The average tensile strength of bimaterial tensile test samples was found to be around 650 MPa. Hence, rather than identifying a single set of optimal parameters or laser energy density, tensile testing supports the OM findings that a range of values is suitable for producing optimal additively produced bimaterial components of these two alloys. The laser energy density for the optimal interface should be between 57 and 75 J/mm³, alongwith consideration of specific processing parameters. Nano-hardness tests across the interface reinforce the concept of mixing between the two materials. The hardness of SS and MS is around 300 HV and 430 HV respectively as depicted in figure 2.11(a). There is a general increase in nano-hardness across the interface, with one specific location showing a significant hardness spike, nearly equivalent to that of MS. This spot is at the edge of a melt pool with a high MS concentration. The increased hardness here is attributed to the lath martensitic microstructure of MS. Additionally, even if there is some mixing with SS at this point, the finer cellular structures at the edge of the melt pool would lead to higher hardness. Contrastively, the next point falls in an area with a higher SS concentration,

which results in lower hardness.

The variation in penetration depth along the scratch length is illustrated in figure 2.11(b). The scratch begins in the SS region with a penetration depth of approximately 5 μm . As the indenter traverses the interface, the penetration depth gradually decreases to around 4 μm within the MS region, aligning well with the nano-hardness measurements. The region exhibiting this reduction spans roughly 150 μm , corroborating the interface length identified through EDS in the figure 2.9 and the nanohardness variation presented in figure 2.11(a). The acoustic emission shows a marked increase in the MS region beyond the interface. These emissions reflect the release of elastic waves generated by the sudden deformation of materials [61]. The significant emissions observed indicate the formation and propagation of microcracks, thereby suggesting brittle behaviour.

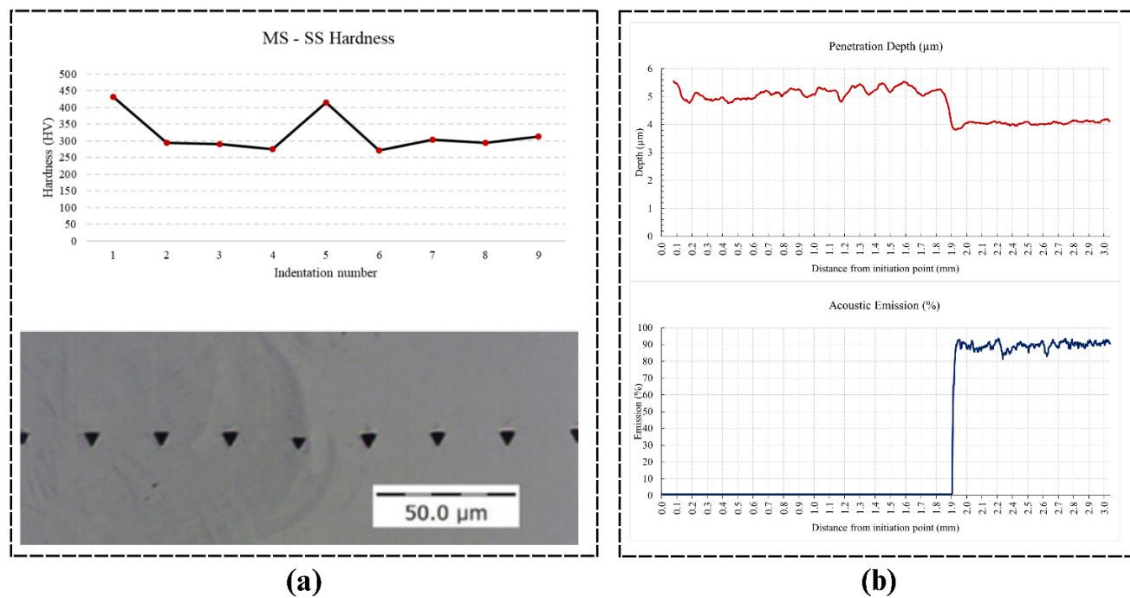


Figure 2.11 (a) Nano-hardness across the interface (b) Depth of penetration and acoustic emission across the interface

2.3.5 Simulation

The simulation results in table 2.6 demonstrate vertical contraction in all lattice structures, indicating vertical NTE. The hexagonal lattice with 0.5mm MS struts, along with the octagonal and dodecagonal lattices, shows a vertical contraction of about 0.5mm. In contrast, the hexagonal lattice with thicker 1mm MS struts experiences a smaller vertical contraction of 0.2mm. MS has a significantly higher yield strength than SS. The greater strength of the 1mm thicker MS struts restricts the stretching, which is essential for these stretch-based lattices, leading to a reduction in contraction by approximately 60%. The deformation contours are depicted in figure 2.12. The NTE behaviour is higher in octagonal lattices, which increases further in dodecagonal lattices.

Table 2.6 Thermal expansion data from Finite Element Analysis

Metamaterial	Vertical Deformation (mm)	Vertical CTE ($\times 10^{-6}$ m/m$^{\circ}$C)
Hexagonal (MS strut 0.5 mm)	-0.0431	-5.17
Hexagonal (MS strut 1 mm)	-0.0134	-1.61
Octagonal	-0.0445	-5.34
Dodecagonal	-0.0483	-5.79

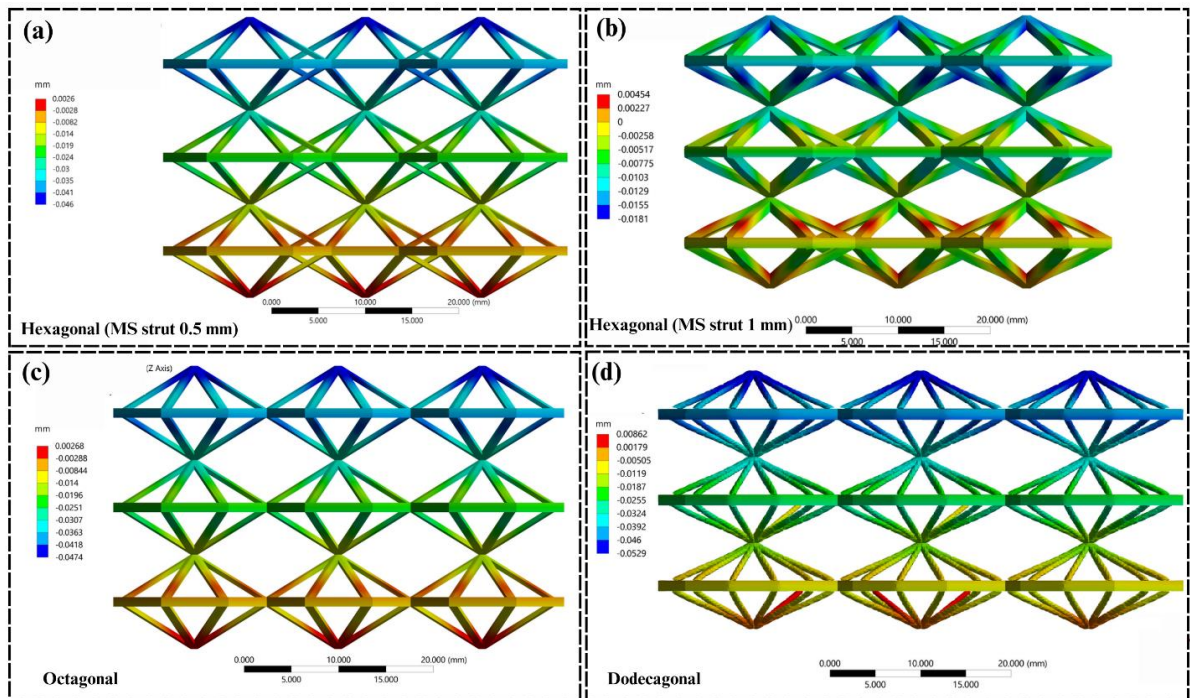


Figure 2.12 Finite element analysis results for vertical expansion for (a)

Hexagonal Lattice with 0.5 mm MS strut thickness (b) Hexagonal Lattice with 1 mm MS strut thickness (c) Octagonal Lattice (d) Dodecagonal Lattice

Being anisotropic NTE metamaterials, all lattice designs show positive expansion in the horizontal plane. The stress analysis shows maximum stress near connecting joints as shown in figure 2.13. This is expected due to differential expansion of the two materials as the bonded joints attempt to keep the struts of different materials connected. Nevertheless, these stresses are within the permissible stress limits identified using tensile tests.

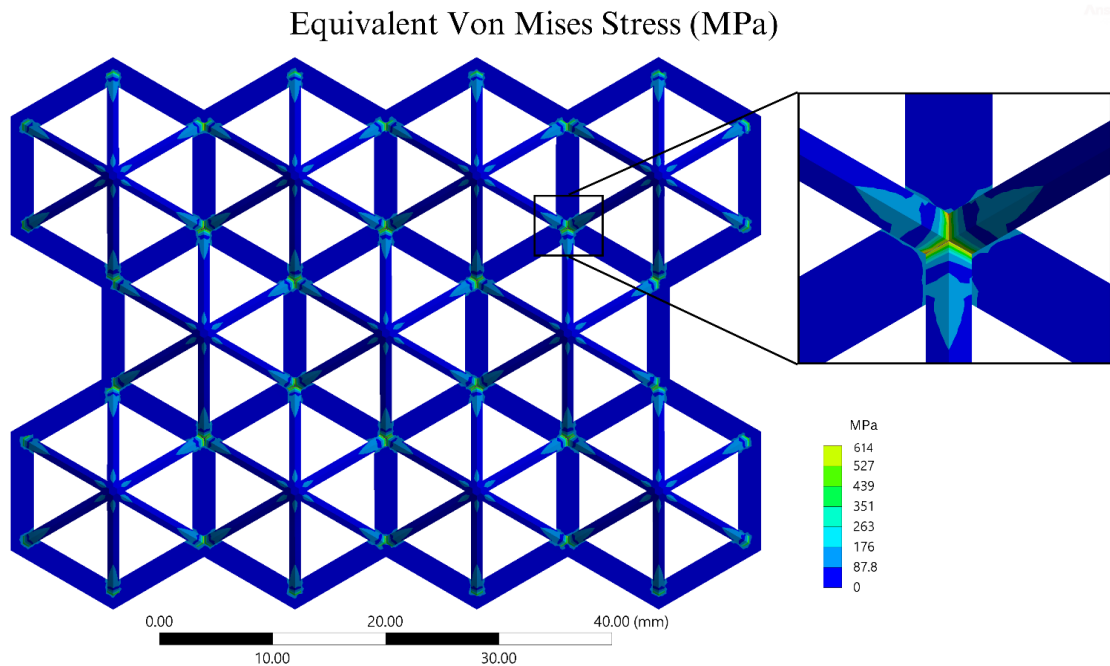


Figure 2.13 Equivalent Von Mises Stress contours in hexagonal lattice with MS Strut thickness 0.5 mm.

2.3.6 Experimental Thermal Testing

Digital Image Correlation (DIC) was used to experimentally visualize and quantify the thermal deformation of an octagonal bipyramid lattice structure. This geometry was selected for testing based on FEA simulations which predicted a superior NTE compared to hexagonal bipyramid lattices, alongside enhanced manufacturability via LPBF with minimal warpage. Conversely, despite the higher FEA-predicted NTE of a dodecagonal unit cell lattice, fabrication issues arose due to its thin metallic struts, resulting in significant warpage.

The DIC results, shown in Figure 2.14, focus on the top face of the LPBF-fabricated lattice. This face was chosen for analysis as it was anticipated to exhibit the highest thermal contraction based on prior simulations. In this specimen-camera configuration, the Z-axis, perpendicular to the camera, aligns with the FEA-predicted contraction direction. The DIC contours illustrate the deformation along the Z-axis, revealing spatial variability in deformation across the top face.

The central region exhibited the most consistent deformation, while measurements ranging from -0.05 mm (contraction) in the bottom-left corner to 0.22 mm (expansion) in the top-right corner were observed along the whole face.

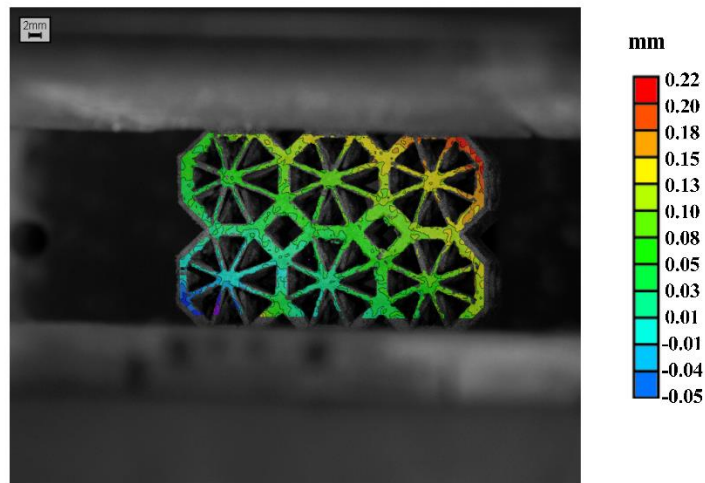


Figure 2.14 Deformation contours on the top face along the Z axis (axis of contraction) in Octagonal Bipyramid lattice. In this specimen-camera configuration, the Z-axis, perpendicular to the camera, aligns with the FEA-predicted contraction direction

Struts located at the lattice edges demonstrated a greater tendency toward expansion. This phenomenon can be attributed to the upward warpage observed during the LPBF process, particularly in peripheral struts. These edge struts are connected to fewer neighbouring struts than those in the lattice centre, leading to reduced heat dissipation during fabrication and consequent warpage. During thermal testing, these struts expanded in the direction of warpage, thereby displaying an anomalous expansion rather than the expected contraction. Additionally, the asymmetric deformation between the left and right sides of the lattice could be partially explained by a slight camera misalignment, which introduced a tilt between the specimen's Z-

axis (actual contraction axis) and the camera's Z-axis (measured contraction axis) in this setup.

2.4 Conclusion

In this study, we successfully fabricated negative thermal expansion mechanical metamaterials using metal additive manufacturing (LPBF) of grade 304 stainless steel and grade 300 maraging steel. The study included a detailed investigation comprising of process parameter development, morphological characterization, interface optimization, mechanical testing, finite element analysis and thermal testing using digital image correlation. The primary conclusions of this study can be classified as:

1. SS-MS Interfacial Bonding: The complete additive fabrication of stainless steel (SS) and maraging steel (MS) using optimized process parameters results in a robust, defect-free interface. This strong bonding is attributed to several key factors:
 - First, as evident in figure 2.8, there is a significant diffusion of elements across the interface, which markedly strengthens the bond. In multi-material additive manufacturing, delamination is a critical issue that can lead to catastrophic failure. However, a gradual transition in composition, facilitated by the diffusion of elements such as chromium (Cr) and nickel (Ni), significantly reduces strain, as corroborated by the KAM map (figure 2.9).
 - Second, no brittle intermetallic phases form during the mixing of the two alloys at the interface, which is a crucial factor in preventing fractures in bimaterial compounds. This avoidance of brittle intermetallics indicates the integrity of the interface (figure 2.7, figure 2.8).
 - Third, the interfacial bonding is further enhanced by the increased depth of melt pools at the interface, a result of inward Marangoni flow. Unlike the typical outward

Marangoni flow observed in most materials, the higher sulphur content in SS induces an inward flow, driving the MS downwards into the previously deposited SS layers (figure 2.7(c)). This creates interlocked structures and a gradient in composition.

2. Mechanical Testing of Interface: A comprehensive evaluation of interfacial strength, conducted through tensile, nano-hardness, and scratch testing, strongly corroborates the robust bonding observed in morphological analyses. The findings can be summarized as:

- Tensile tests reveal an ultimate tensile strength of approximately 650 MPa, with fractures consistently avoiding the interface. These results suggest that optimal interfacial strength in SS and MS can be achieved across a range of energy densities and processing parameters rather than a singular value, specifically between 57 J/mm³ and 75 J/mm³.
- Nano-hardness testing highlights the presence of compositional gradient coupled with micro-segregation at the interface. A noticeable increase in hardness precisely at the centre of the interface, as depicted in (figure 2.11(a)), indicates the presence of a hard MS core, flanked by zones dominated by softer SS.
- Scratch testing reveals smooth, debris-free scratches in the SS region, which transition to slightly jagged scratches with debris in the MS area. This suggests ductile behaviour in SS and a somewhat brittle response in MS. The sharper, high-amplitude acoustic emission signals observed in the MS section further confirm its brittle nature. Additionally, the gradual decrease in penetration depth across the interface reinforces the presence of a distinct compositional gradient (figure 2.10(b)).

3. Finite Element Analysis of Lattices: The numerical analysis results conclude:

- The influence of strut thickness on the overall CTE is considerable. An increase in the thickness of a low-expansion material (MS) leads to a higher overall CTE in the direction of negative expansion. This is because the increased thickness diminishes the extent of strut elongation caused by the faster expansion of stainless steel (SS), given that MS, characterized by its higher yield strength, is inherently stronger.
- Similarly, augmenting the thickness of SS leads to a reduction in negative expansion. This is because the enhanced expansion of SS, due to its increased thickness, contributes directly to expansion in the vertical direction, which aligns with the orientation of NTE.
- NTE performance improves in the following order: thicker hexagonal lattices, thinner hexagonal lattices, octagonal lattices, and dodecagonal lattices. The highest negative thermal expansion observed was for dodecagonal bipyramid lattice, approximately, $-5.79 \times 10^{-6} \text{ m/m}^\circ\text{C}$, followed by octagonal bipyramid at -5.34×10^{-6} . The thickness of struts of low expansion material plays a significant role. Increasing the strut thickness to 1mm from 0.5mm led to an increase in CTE from $-5.17 \times 10^{-6} \text{ m/m}^\circ\text{C}$ to $-1.61 \times 10^{-6} \text{ m/m}^\circ\text{C}$.
- An increase in the number of sides in the base polygon enhances the fabricability of lattices by reducing overhang length and minimizing warpage. Therefore, when employing bipyramid unit cell-based lattices, it is advisable to increase the number of sides in the base polygon.
- The highest stresses occur at the junctions where struts of different materials intersect. However, these stresses remain within the permissible limits established through tensile testing. This outcome is attributable to the rigid defect-free interface achieved through the optimization of interfacial process parameters conducted in this study.

4. Experimental Thermal Testing

The FEA-predicted NTE was partially confirmed, particularly in the central region of the lattice, which exhibited consistent deformation. However, spatial variability was observed across the top face, with some regions demonstrating expansion rather than contraction, particularly at the lattice edges. This unexpected expansion was likely caused by:

- Upward warpage during the LPBF fabrication process, particularly in struts connected to fewer neighbouring elements, where reduced heat dissipation led to greater thermal distortion.
- Furthermore, a slight misalignment between the specimen's and camera's Z-axes likely contributed to the asymmetry in deformation across the lattice face.
- Other minor differences in FEA predictions and experimental testing would be caused by the difference in properties of LPBF fabricated steels and conventionally manufactured steels. FEA simulations did not take into account these differences and predicated based on conventional properties. Also, FEA simulations assumed a sharp interface with no diffusion zone.

The testing highlighted the importance of both lattice geometry and fabrication conditions in influencing thermal behaviour, and they underline the need for careful control of manufacturing parameters to minimize warpage and ensure reliable NTE performance.

In summary, this study successfully demonstrated the potential of using LPBF to fabricate NTE mechanical metamaterials through optimized process parameters and robust interfacial bonding between stainless steel and maraging steel. The bottom-up approach to fabrication and testing revealed key insights into the critical role of interface characteristics, lattice geometry, and

material selection in achieving reliable NTE performance. However, the spatial variability observed in experimental results underscores the need for continued refinement of the process, particularly in managing thermal distortions and improving the accuracy of FEA predictions for additive-manufactured structures. Future work should focus on further optimizing lattice designs, refining interfacial properties, and integrating more accurate LPBF-specific material models into simulations to better predict and control thermal responses in these metamaterials.

References

- [1] P. Juasiripukdee, I. Maskery, I. Ashcroft, and R. Leach, “Low thermal expansion machine frame designs using lattice structures,” *Applied Sciences (Switzerland)*, vol. 11, no. 19, Oct. 2021, doi: 10.3390/app11199135.
- [2] L. Niu, S. J. Dong, T. T. Kong, R. Wang, R. Zou, and Q. Da Liu, “Heat transfer behavior across the dentino-enamel junction in the human tooth,” *PLoS One*, vol. 11, no. 9, Sep. 2016, doi: 10.1371/journal.pone.0158233.
- [3] D. Devoto, P. Paul, S. Narumanchi, and M. Mihalic, “Reliability of Bonded Interfaces for Automotive Power Electronics,” *Proceedings of the ASME 2013 International Technical Conference and Exhibition on Packaging and Integration of Electronic and Photonic Microsystems*. Volume 1, Jul. 2013.
- [4] O. Hodjati-Pugh, A. Dhir, and R. Steinberger-Wilckens, “The development of current collection in micro-tubular solid oxide fuel cells—a review,” Feb. 01, 2021, MDPI AG. doi: 10.3390/app11031077.
- [5] B. Yu, Z. Xu, R. Mu, A. Wang, and H. Zhao, “Design of Large-Scale Space Lattice Structure with Near-Zero Thermal Expansion Metamaterials,” *Aerospace*, vol. 10, no. 3, Mar. 2023, doi: 10.3390/aerospace10030294.

- [6] A. Sahoo and V. R. R. Medicherla, “Fe-Ni Invar alloys: A review,” *Mater Today Proc*, vol. 43, pp. 2242–2244, 2021, doi: <https://doi.org/10.1016/j.matpr.2020.12.527>.
- [7] A. Shokrani, N. Reade, and C. Mahn, “Machining Alloy 52 Kovar using different machining environments,” *Procedia CIRP*, vol. 78, pp. 335–340, 2018, doi: <https://doi.org/10.1016/j.procir.2018.09.047>.
- [8] V. S. Deshpande, M. F. Ashby, and N. A. Fleck, “Foam topology: bending versus stretching dominated architectures,” *Acta Mater*, vol. 49, no. 6, pp. 1035–1040, 2001, doi: [https://doi.org/10.1016/S1359-6454\(00\)00379-7](https://doi.org/10.1016/S1359-6454(00)00379-7).
- [9] Q. Wang, J. A. Jackson, Q. Ge, J. B. Hopkins, C. M. Spadaccini, and N. X. Fang, “Lightweight Mechanical Metamaterials with Tunable Negative Thermal Expansion,” *Phys Rev Lett*, vol. 117, no. 17, Oct. 2016, doi: [10.1103/PhysRevLett.117.175901](https://doi.org/10.1103/PhysRevLett.117.175901).
- [10] D. Dubey, A. S. Mirhakimi, and M. A. Elbestawi, “Negative Thermal Expansion Metamaterials: A Review of Design, Fabrication, and Applications,” *Journal of Manufacturing and Materials Processing*, vol. 8, no. 1, 2024, doi: [10.3390/jmmp8010040](https://doi.org/10.3390/jmmp8010040).
- [11] J. Guan and Q. Wang, “Laser Powder Bed Fusion of Dissimilar Metal Materials: A Review,” Apr. 01, 2023, MDPI. doi: [10.3390/ma16072757](https://doi.org/10.3390/ma16072757).
- [12] D. Wang et al., “Recent progress on additive manufacturing of multi-material structures with laser powder bed fusion,” 2022, Taylor and Francis Ltd. doi: [10.1080/17452759.2022.2028343](https://doi.org/10.1080/17452759.2022.2028343).
- [13] L. S. Kollmannsperger, O. Maurer, R. Kose, A. T. Zeuner, D. Bähre, and S. C. L. Fischer, “Acoustic emission of lattice structures under cycling loading relates process parameters with fatigue properties,” *Communications Engineering*, vol. 3, no. 1, p. 56, 2024, doi: [10.1038/s44172-024-00196-2](https://doi.org/10.1038/s44172-024-00196-2).

- [14] A. Mussatto, “Research progress in multi-material laser-powder bed fusion additive manufacturing: A review of the state-of-the-art techniques for depositing multiple powders with spatial selectivity in a single layer,” *Results in Engineering*, vol. 16, p. 100769, 2022, doi: <https://doi.org/10.1016/j.rineng.2022.100769>.
- [15] L. Xiao and W. Song, “Additively-manufactured functionally graded Ti-6Al-4V lattice structures with high strength under static and dynamic loading: Experiments,” *Int J Impact Eng*, vol. 111, pp. 255–272, 2018, doi: <https://doi.org/10.1016/j.ijimpeng.2017.09.018>.
- [16] Z. Wu, S. P. Narra, and A. Rollett, “Exploring the fabrication limits of thin-wall structures in a laser powder bed fusion process,” *The International Journal of Advanced Manufacturing Technology*, vol. 110, no. 1, pp. 191–207, 2020, doi: [10.1007/s00170-020-05827-4](https://doi.org/10.1007/s00170-020-05827-4).
- [17] T. F. Babuska, B. A. Krick, D. F. Susan, and A. B. Kustas, “Comparison of powder bed fusion and directed energy deposition for tailoring mechanical properties of traditionally brittle alloys,” *Manuf Lett*, vol. 28, pp. 30–34, Apr. 2021, doi: [10.1016/j.mfglet.2021.02.003](https://doi.org/10.1016/j.mfglet.2021.02.003).
- [18] C. Schwerz, F. Schulz, E. Natesan, and L. Nyborg, “Increasing productivity of laser powder bed fusion manufactured Hastelloy X through modification of process parameters,” *J Manuf Process*, vol. 78, pp. 231–241, 2022, doi: <https://doi.org/10.1016/j.jmapro.2022.04.013>.
- [19] F. Ceccanti, A. Giorgetti, and P. Citti, “A Support Structure Design Strategy for Laser Powder Bed Fused Parts,” *Procedia Structural Integrity*, vol. 24, pp. 667–679, 2019, doi: <https://doi.org/10.1016/j.prostr.2020.02.059>.
- [20] C. F. Tey, X. Tan, S. L. Sing, and W. Y. Yeong, “Additive manufacturing of multiple materials by selective laser melting: Ti-alloy to stainless steel via a Cu-alloy interlayer,” *Addit Manuf*, vol. 31, Jan. 2020, doi: [10.1016/j.addma.2019.100970](https://doi.org/10.1016/j.addma.2019.100970).
- [21] C. Wei et al., “Multi-material additive-manufacturing of tungsten - copper alloy bimetallic

structure with a stainless-steel interlayer and associated bonding mechanisms,” *Addit Manuf*, vol. 50, Feb. 2022, doi: 10.1016/j.addma.2021.102574.

[22] Y. Bai, J. Zhang, C. Zhao, C. Li, and H. Wang, “Dual interfacial characterization and property in multi-material selective laser melting of 316L stainless steel and C52400 copper alloy,” *Mater Charact*, vol. 167, p. 110489, 2020, doi: <https://doi.org/10.1016/j.matchar.2020.110489>.

[23] Z. H. Liu, D. Q. Zhang, S. L. Sing, C. K. Chua, and L. E. Loh, “Interfacial characterization of SLM parts in multi-material processing: Metallurgical diffusion between 316L stainless steel and C18400 copper alloy,” *Mater Charact*, vol. 94, pp. 116–125, 2014, doi: 10.1016/j.matchar.2014.05.001.

[24] X. Mei, X. Wang, Y. Peng, H. Gu, G. Zhong, and S. Yang, “Interfacial characterization and mechanical properties of 316L stainless steel/inconel 718 manufactured by selective laser melting,” *Materials Science and Engineering: A*, vol. 758, pp. 185–191, Jun. 2019, doi: 10.1016/j.msea.2019.05.011.

[25] S. L. Sing, L. P. Lam, D. Q. Zhang, Z. H. Liu, and C. K. Chua, “Interfacial characterization of SLM parts in multi-material processing: Intermetallic phase formation between AlSi10Mg and C18400 copper alloy,” *Mater Charact*, vol. 107, pp. 220–227, Jul. 2015, doi: 10.1016/j.matchar.2015.07.007.

[26] A. Hinojos et al., “Joining of Inconel 718 and 316 Stainless Steel using electron beam melting additive manufacturing technology,” *Mater Des*, vol. 94, pp. 17–27, 2016, doi: <https://doi.org/10.1016/j.matdes.2016.01.041>.

[27] M. G. Scaramuccia, A. G. Demir, L. Caprio, O. Tassa, and B. Previtali, “Development of processing strategies for multigraded selective laser melting of Ti6Al4V and IN718,” *Powder*

Technol, vol. 367, pp. 376–389, May 2020, doi: 10.1016/J.POWTEC.2020.04.010.

[28] R. Wang, D. Gu, K. Lin, C. Chen, Q. Ge, and D. Li, “Multi-material additive manufacturing of a bio-inspired layered ceramic/metal structure: Formation mechanisms and mechanical properties,” *Int J Mach Tools Manuf*, vol. 175, p. 103872, 2022, doi: <https://doi.org/10.1016/j.ijmachtools.2022.103872>.

[29] A. Bin Anwar and Q.-C. Pham, “Study of the spatter distribution on the powder bed during selective laser melting,” 2018, doi: 10.1016/j.addma.2018.04.036.

[30] G. Kasperovich, J. Haubrich, J. Gussone, and G. Requena, “Correlation between porosity and processing parameters in TiAl6V4 produced by selective laser melting,” 2016, doi: 10.1016/j.matdes.2016.05.070.

[31] C. Tan, K. Zhou, W. Ma, and L. Min, “Interfacial characteristic and mechanical performance of maraging steel-copper functional bimetal produced by selective laser melting based hybrid manufacture,” *Mater Des*, vol. 155, pp. 77–85, Oct. 2018, doi: 10.1016/j.matdes.2018.05.064.

[32] J. Chen, Y. Yang, C. Song, M. Zhang, S. Wu, and D. Wang, “Interfacial microstructure and mechanical properties of 316L /CuSn10 multi-material bimetallic structure fabricated by selective laser melting,” *Materials Science and Engineering: A*, vol. 752, pp. 75–85, Apr. 2019, doi: 10.1016/j.msea.2019.02.097.

[33] M. Zhang, Y. Yang, D. Wang, C. Song, and J. Chen, “Microstructure and mechanical properties of CuSn/18Ni300 bimetallic porous structures manufactured by selective laser melting,” *Mater Des*, vol. 165, Mar. 2019, doi: 10.1016/j.matdes.2019.107583.

[34] S. Shakerin, A. Hadadzadeh, B. S. Amirkhiz, S. Shamsdini, J. Li, and M. Mohammadi, “Additive manufacturing of maraging steel-H13 bimetals using laser powder bed fusion

technique,” *Addit Manuf*, vol. 29, Oct. 2019, doi: 10.1016/j.addma.2019.100797.

[35] D. Wang, Y. Yang, Z. Yi, and X. Su, “Research on the fabricating quality optimization of the overhanging surface in SLM process,” *The International Journal of Advanced Manufacturing Technology*, vol. 65, no. 9, pp. 1471–1484, 2013, doi: 10.1007/s00170-012-4271-4.

[36] C. K. Sit, L. N. S. Chiu, Y. Tang, and A. Huang, “Towards supportless laser powder bed fusion: fundamental understanding of the formation of 1st layer overhang through parameter optimisation and in-situ high-speed thermal imaging,” *Virtual Phys Prototyp*, vol. 18, no. 1, p. e2231906, Dec. 2023, doi: 10.1080/17452759.2023.2231906.

[37] F. Calignano, “Design optimization of supports for overhanging structures in aluminum and titanium alloys by selective laser melting,” *Mater Des*, vol. 64, pp. 203–213, 2014, doi: <https://doi.org/10.1016/j.matdes.2014.07.043>.

[38] G. Yang et al., “Support design of overhanging structure for laser powder bed fusion,” *Journal of Materials Research and Technology*, vol. 24, pp. 8693–8702, 2023, doi: <https://doi.org/10.1016/j.jmrt.2023.05.087>.

[39] A. I. C. E.-28 on M. Testing, *Standard test methods for tension testing of metallic materials*. ASTM international, 2021.

[40] International Standard ISO 14577-1:2015, “Metallic materials — Instrumented indentation test for hardness and materials parameters,” International Organization for Standardization, 2015.

[41] ASTM Standard C1624-22, “Standard Test Method for Adhesion Strength and Mechanical Failure Modes of Ceramic Coatings by Quantitative Single Point Scratch Testing,” ASTM International, 2022.

- [42] I. Gleason and I. Hubbard, “Products of abstract polytopes,” *J Comb Theory Ser A*, vol. 157, pp. 287–320, 2018, doi: <https://doi.org/10.1016/j.jcta.2018.02.002>.
- [43] G. Casalino, S. L. Campanelli, N. Contuzzi, and A. D. Ludovico, “Experimental investigation and statistical optimisation of the selective laser melting process of a maraging steel,” *Opt Laser Technol*, vol. 65, pp. 151–158, 2015, doi: <https://doi.org/10.1016/j.optlastec.2014.07.021>.
- [44] C. Tan, K. Zhou, W. Ma, P. Zhang, M. Liu, and T. Kuang, “Microstructural evolution, nanoprecipitation behavior and mechanical properties of selective laser melted high-performance grade 300 maraging steel,” *Mater Des*, vol. 134, pp. 23–34, 2017, doi: <https://doi.org/10.1016/j.matdes.2017.08.026>.
- [45] J. Suryawanshi, K. G. Prashanth, and U. Ramamurty, “Tensile, fracture, and fatigue crack growth properties of a 3D printed maraging steel through selective laser melting,” *J Alloys Compd*, vol. 725, pp. 355–364, 2017, doi: <https://doi.org/10.1016/j.jallcom.2017.07.177>.
- [46] J. Hou, W. Chen, Z. Chen, K. Zhang, and A. Huang, “Microstructure, tensile properties and mechanical anisotropy of selective laser melted 304L stainless steel,” *J Mater Sci Technol*, vol. 48, pp. 63–71, 2020, doi: <https://doi.org/10.1016/j.jmst.2020.01.011>.
- [47] S. A. Khairallah, A. T. Anderson, A. Rubenchik, and W. E. King, “Laser powder-bed fusion additive manufacturing: Physics of complex melt flow and formation mechanisms of pores, spatter, and denudation zones,” *Acta Mater*, vol. 108, pp. 36–45, 2016, doi: <https://doi.org/10.1016/j.actamat.2016.02.014>.
- [48] J. Wang, R. Zhu, Y. Liu, and L. Zhang, “Understanding melt pool characteristics in laser powder bed fusion: An overview of single- and multi-track melt pools for process optimization,” *Advanced Powder Materials*, vol. 2, no. 4, p. 100137, 2023, doi: <https://doi.org/10.1016/j.apsm.2023.100137>.

<https://doi.org/10.1016/j.apmate.2023.100137>.

[49] T. Ramakrishnan et al., “Crack-Free Tungsten Fabricated via Laser Powder Bed Fusion Additive Manufacturing,” *Adv Funct Mater*, vol. 34, no. 12, Mar. 2024, doi: 10.1002/adfm.202309304.

[50] S. Mishra, T. J. Lienert, M. Q. Johnson, and T. DebRoy, “An experimental and theoretical study of gas tungsten arc welding of stainless steel plates with different sulfur concentrations,” *Acta Mater*, vol. 56, no. 9, pp. 2133–2146, 2008, doi: <https://doi.org/10.1016/j.actamat.2008.01.028>.

[51] L. Aucott et al., “Revealing internal flow behaviour in arc welding and additive manufacturing of metals,” *Nat Commun*, vol. 9, no. 1, p. 5414, 2018, doi: 10.1038/s41467-018-07900-9.

[52] Th. Schubert, W. Löser, S. Schinnerling, and I. Bächer, “Alternative phase formation in thin strip casting of stainless steels,” *Materials Science and Technology*, vol. 11, no. 2, pp. 181–185, Feb. 1995, doi: 10.1179/mst.1995.11.2.181.

[53] T. DebRoy et al., “Additive manufacturing of metallic components – Process, structure and properties,” *Prog Mater Sci*, vol. 92, pp. 112–224, 2018, doi: <https://doi.org/10.1016/j.pmatsci.2017.10.001>.

[54] P. Kürnsteiner, M. B. Wilms, A. Weisheit, P. Barriobero-Vila, E. A. Jäggle, and D. Raabe, “Massive nanoprecipitation in an Fe-19Ni-xAl maraging steel triggered by the intrinsic heat treatment during laser metal deposition,” *Acta Mater*, vol. 129, pp. 52–60, 2017, doi: <https://doi.org/10.1016/j.actamat.2017.02.069>.

[55] A. Hunter and M. Ferry, “Phase formation during solidification of AISI 304 austenitic stainless steel,” *Scr Mater*, vol. 46, no. 4, pp. 253–258, 2002, doi:

[https://doi.org/10.1016/S1359-6462\(01\)01215-5](https://doi.org/10.1016/S1359-6462(01)01215-5).

[56] X. Li and Z. Yin, “Reverted austenite during aging in 18Ni(350) maraging steel,” *Mater Lett*, vol. 24, no. 4, pp. 239–242, 1995, doi: [https://doi.org/10.1016/0167-577X\(95\)00109-3](https://doi.org/10.1016/0167-577X(95)00109-3).

[57] M. K. El-Fawkhry, M. Eissa, A. Fathy, and T. Mattar, “Development of Maraging Steel with Retained Austenite in Martensite Matrix,” *Mater Today Proc*, vol. 2, pp. S711–S714, 2015, doi: <https://doi.org/10.1016/j.matpr.2015.07.381>.

[58] S. I. Wright, M. M. Nowell, and D. P. Field, “A Review of Strain Analysis Using Electron Backscatter Diffraction,” *Microscopy and Microanalysis*, vol. 17, no. 3, pp. 316–329, 2011, doi: DOI: 10.1017/S1431927611000055.

[59] S. J. Sun, Y. Z. Tian, H. R. Lin, Z. J. Wang, and Z. F. Zhang, “Revisiting the role of prestrain history in the mechanical properties of ultrafine-grained CoCrFeMnNi high-entropy alloy,” *Materials Science and Engineering: A*, vol. 801, p. 140398, 2021, doi: <https://doi.org/10.1016/j.msea.2020.140398>.

[60] Q. Wang et al., “Microstructure and Mechanical Performance of 304 Stainless Steel Fabricated by Laser Powder Bed Fusion: The Effect of Post-Processing Heat Treatment,” *J Mater Eng Perform*, vol. 32, no. 2, pp. 695–711, 2023, doi: 10.1007/s11665-022-07108-5.

[61] Z. Nazarchuk, V. Skalskyi, and O. Serhiyenko, “Acoustic emission,” *Foundations of Engineering Mechanics*, 2017.

**3 Chapter 3 Negative Thermal Expansion lattices
using laser powder bed fusion of SS304L and Invar
36**

Abstract

Steel is the most widely used alloy worldwide, and the development of negative thermal expansion (NTE) structures based on steel could transform industries like precision devices by reducing reliance on rare negative expansion materials. This study presents the comprehensive development of NTE lattice metamaterials produced via laser powder bed fusion (LPBF), encompassing material characterization, mechanical testing, structural design, numerical simulation, fabrication, and thermal expansion performance evaluation. AISI 304L stainless steel and Invar 36 were selected as the constituent alloys. The research commences with an investigation into the process-structure-property relationships, focusing on optimizing processing parameters to strengthen the interfacial bonding between the alloys. Microstructural analysis, nano-hardness, and scratch resistance testing were carried out to evaluate interfacial behaviour, with advanced microscopy techniques providing insights into interface formation. Bimaterial lattice structures were subsequently designed with a focus on thermal expansion performance and support-free manufacturability. Finite element simulations informed the selection of designs, which were fabricated using the optimized parameters. Three of the designs exhibited negative thermal expansion, while one demonstrated near-zero expansion, highlighting the potential for customization based on application-specific thermal properties. The thermal expansion behaviour of identified lattices was verified through digital image correlation experiments.

3.1 Introduction

Metamaterials are architected materials characterized by unique properties that arise primarily from their architecture rather than their natural composition [1]. These materials have garnered significant interest due to their customizable multifunctional properties, which are not found in naturally occurring or conventionally manufactured materials. Mechanical metamaterials, a specific category of metamaterials, rely on static mechanisms and achieve their unique properties through the modification of structural patterns [2]. Their examples include materials with negative Poisson ratios [3], tunable stiffness [4], and negative coefficient of thermal expansion (CTE) [5]. This study focuses on mechanical metamaterials with negative CTE properties, which exhibit exceptional thermal characteristics, such as negative or negligible thermal expansion. Most natural solid materials exhibit positive thermal expansion, expanding when heated and contracting when cooled due to changes in interatomic bond lengths. However, some exceptions exist, such as natural zeolites [6] and composites like PbTiO_3/Cu [7] and cement/ ZrW_2O_8 [8], which display negative thermal expansion (NTE) but only within a limited temperature range. These composites typically possess random microstructures, making it difficult to finetune their NTE properties. Unlike traditional composites, additively manufactured lattice metamaterials with defined topologies offer precise control over thermal expansion, making them ideal for applications requiring minimal thermal expansion, like space structures [9], precision devices [10], medical implants [11], and semiconductor technologies [12].

The architecture of NTE metamaterials is primarily multiphase lattice structures, typically integrating at least two constituents with substantially different CTE. These constituent materials are arranged in such a way that expansion of one counteracts that of the others. The

designs typically feature a periodically repeating structure, also called a lattice, where a unit cell is engineered according to specific functional requirements [13]. This unit cell is repeated in one, two, or three dimensions to form the lattice. Nonetheless, depending on the intended application, metamaterials can also feature functionally graded, semi-regular, or irregular structural design [14], [15]. The working mechanisms of these metamaterials can be categorized into bending-dominated and stretch-dominated systems [16]. In bending-based architectures, the differential expansion between materials induces bending within the structure, leading to overall contraction in one or more directions. Examples include bimaterial strips, chiral structures, and re-entrant cells. However, bending-dominated designs often suffer with stiffness at elevated temperatures due to the bending of structural elements during performance. To enhance the strength and stiffness of lattices, it is beneficial to avoid bending-dependent architecture. Stretch-dominated lattices, which operate with minimal bending, function based on the expansion of their edges. To achieve increased structural strength, the current work focuses on stretch-dominated lattices.

Very few NTE metamaterials have been fabricated using metals in literature. Among these, most have been produced using assembly-based manufacturing methods [5]. Laser powder bed fusion (LPBF), a metal additive manufacturing technique, is promising for fabrication of metal NTE lattices due to its capability of fabricating high resolution complex structures and ability to produce multiphase structures right out of the machine with slight modifications [17]. However, since LPBF is primarily a single material manufacturing, certain challenges need to be addressed. These include insolubility of constituents [18], difference in physical properties (e.g., melting point) [19], formation of brittle intermetallic phases at the interface [20], and cracking due to differential thermal properties [21]. These undesirable phenomena can lead to defects

like porosity, cracking, and delamination, which can severely compromise the joint strength between different metals and alloys. Therefore, process optimization is essential to create strong, defect-free interfaces when fabricating multi-material components using LPBF, including NTE metamaterials.

In this study, AISI 304 grade stainless steel (SS) and Invar 36 (FeNi36) alloy were used to fabricate bimaterial NTE lattices and were investigated for bonding compatibility as well as interface characterization. These two types of steels were selected for several reasons. Primarily, they have a high difference in their CTE. SS has a thermal expansion coefficient of $\sim 21 \times 10^{-6}$ m/m°C [22], while Invar has a CTE of $\sim 2 \times 10^{-6}$ m/m°C [23]. The low positive CTE of Invar would also be beneficial towards NTE performance of the overall structure. Both being iron alloys, a similar composition would help prevent issues related to chemical incompatibility. Nevertheless, an investigation is necessary to identify optimum process parameters to ensure a defect-free bond between the two alloys. This is the first step before approaching the fabrication of the complex lattices which shall have many bi-alloy interfaces. Therefore, an extensive characterization analysis of the interface must precede the actual design and testing study of NTE metamaterials.

This study investigates both compositional and geometric complexity involved in creating a metallic NTE metamaterial. To simplify this, we utilized a staged approach in this paper with following research steps:

- Process optimization to achieve a defect-free interface between SS and Invar alloys.
- Development of an understanding of interfacial morphology and its characterization.
- Structural design of multiphase NTE lattices using the two alloys.
- Performance analysis of the designed lattices using finite element analysis (FEA).

- Fabrication of lattices using LPBF and investigation of the process-based constraints on design.
- Experimental testing of the thermal expansion of the lattices and comparison with FEA results.

3.2 Experimental Details

3.2.1 Machine and Materials

For LPBF fabrication, gas atomized SS304L powder, supplied by Carpenter Technology Ltd (Philadelphia, US) and Invar 36 powder was supplied by Sandvik Osprey Ltd (Neath, UK), were used as raw feedstock. The powder particles had diameters ranging from 15 μ m – 60 μ m. The elemental composition of the two powders is mentioned in table 3.1.

Table 3.1 Elemental composition of feedstock powder

SS 304L Stainless Steel						
C	Cr	Ni	Mn	Si	P,S	Fe
≤0.03	18-19.5	8-10	0.5-2	0.66	≤0.04	Bal.
Invar 36						
Ni	Mn	Si	Fe			
36.1	0.21	0.2	Bal.			

For LPBF fabrication, EOS M280 DMLS machine at McMaster University was used. It has a 400W Yb-fibre laser with a 100 μ m spot size, operating at a wavelength of 1070 nm, and offers a build platform of 250 mm \times 250 mm \times 325 mm. During the process, the powder bed temperature was consistently maintained at 40°C. Argon gas was pumped in the chamber to shield the material from oxidation, ensuring the oxygen level remained below 0.1% throughout. The fabrication process was divided into two primary stages: the production of solid samples for material characterization and mechanical testing, followed by the creation of bimaterial

lattices.

3.2.2 Fabrication of Characterization Samples

In this phase, solid specimens were produced for the purposes of material characterization and mechanical testing. The process began with determining optimal parameters for each alloy individually, using 10 mm cubic samples and assessing their density using the Archimedes method [24]. Following this, specimens with a material interface were fabricated for further analysis. For bimaterial coupons featuring a single interface, the fabrication was paused at the midpoint of the sample's height. At this juncture, the SS powder was removed, the build chamber was meticulously cleaned, and Invar powder was introduced. The process then resumed, applying interface-specific parameters across five layers before proceeding with the optimal Invar parameters to complete the build. In all instances, including multimaterial samples, the layer thickness was consistently maintained at 40 μm , and a 67° rotation of scan lines was implemented with each new layer.

For mechanical characterization, nano-hardness and scratch tests were performed to evaluate hardness and scratch resistance properties at the interface. Identical samples to those used in material characterization were fabricated and vertically sectioned at the centre to facilitate these tests.

3.2.3 Material Characterization

For the metallurgical analysis of the interface, the specimens were sectioned along the build direction, followed by polishing and examination with a Keyence VHX5000 optical microscope. To assess the melt pool and morphology, the samples underwent a 3-minute etching process using Carpenter etchant (8.5g FeCl_3 , 2.4g CuCl_2 , 122ml Ethanol, 122ml HCl and 6ml HNO_3). Subsequent analyses were performed using a Nikon LV500 optical microscope and a Vega

Tescan SEM. The elemental distribution across the interface was examined using the EDS detector integrated into the Vega Tescan SEM. Additionally, the grain orientation and phase distribution in the interfacial regions were evaluated through electron back-scattered diffraction (EBSD). This analysis was carried out on both the interface and the individual material regions using an FE Versa 3D field-emission SEM, with a step size ranging from 1 to 5 μm . The collected data were processed and analysed using the TSL OIM 7 and HKL Channel 5 software packages.

3.2.4 Mechanical Testing

To evaluate interfacial mechanical properties, nano-hardness and scratch resistance tests were performed. The nano-hardness at the interface was measured using an Anton Paar NHT3 nanoindentation platform, adhering to the ISO standard 14577 [25]. It utilized a Berkovich diamond indenter tip, applying a linear load up to 40 mN, with loading and unloading rates of 80 mN/min. A total of 10 indentations were made traversing across the interface with a distance of 25 μm between each penetration. For the scratch test, an Anton-Paar Revetest scratch tester with a Rockwell Diamond indenter (tip radius of 200 μm) was used. The test was carried out under a constant load of 10 N, at a scratch rate of 2 mm/min over a length of 3 mm, in accordance with ASTM C1624-22 [26]. The sliding contact response across the interface was analysed by monitoring penetration depth and acoustic emission.

3.2.5 Design of Lattice Structures

To create efficient lattice structures, the design phase focused on understanding the constraints and opportunities within the design field. The aim was to ensure that the metamaterial lattices could be manufactured successfully and deliver the desired performance outcomes. The primary requirements for the design can be summarized as:

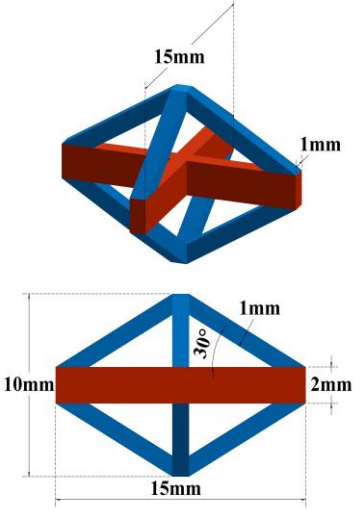
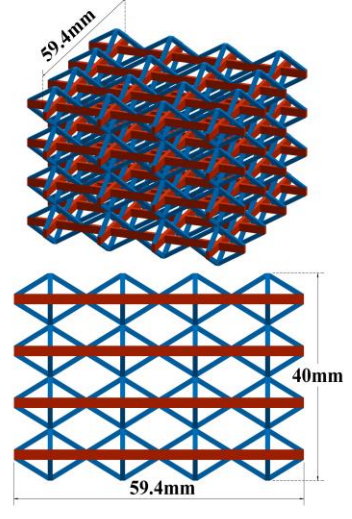
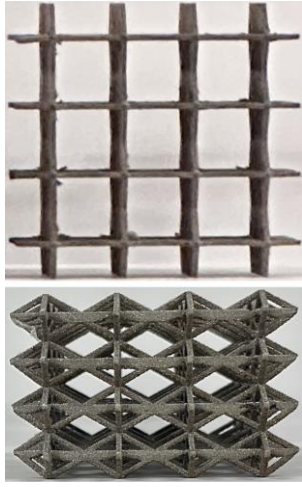
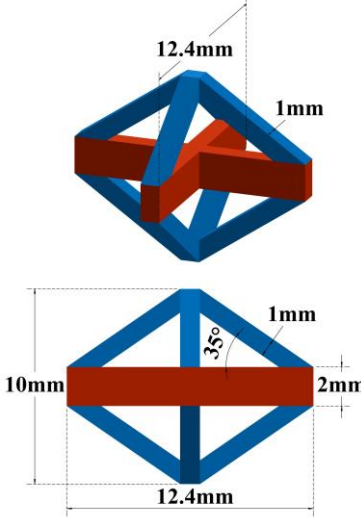
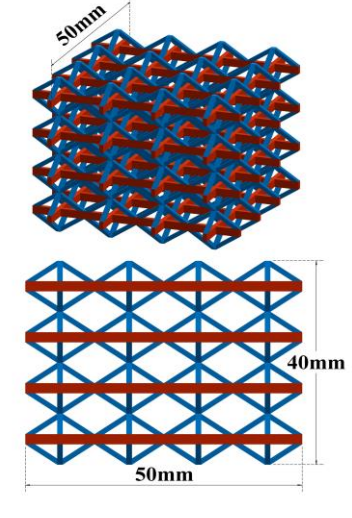
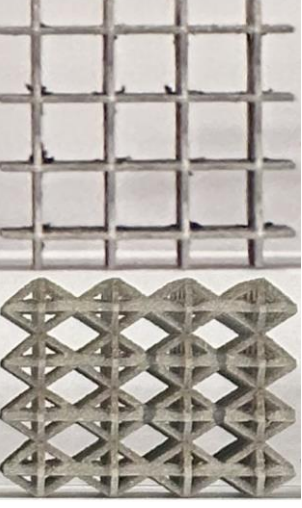
1. Manufacturability using LPBF: The design must be compatible with the LPBF process, adhering to the specific capabilities and limitations of the equipment.
2. Thermal Expansion Control: The lattice must achieve a negative net CTE in at least one direction.

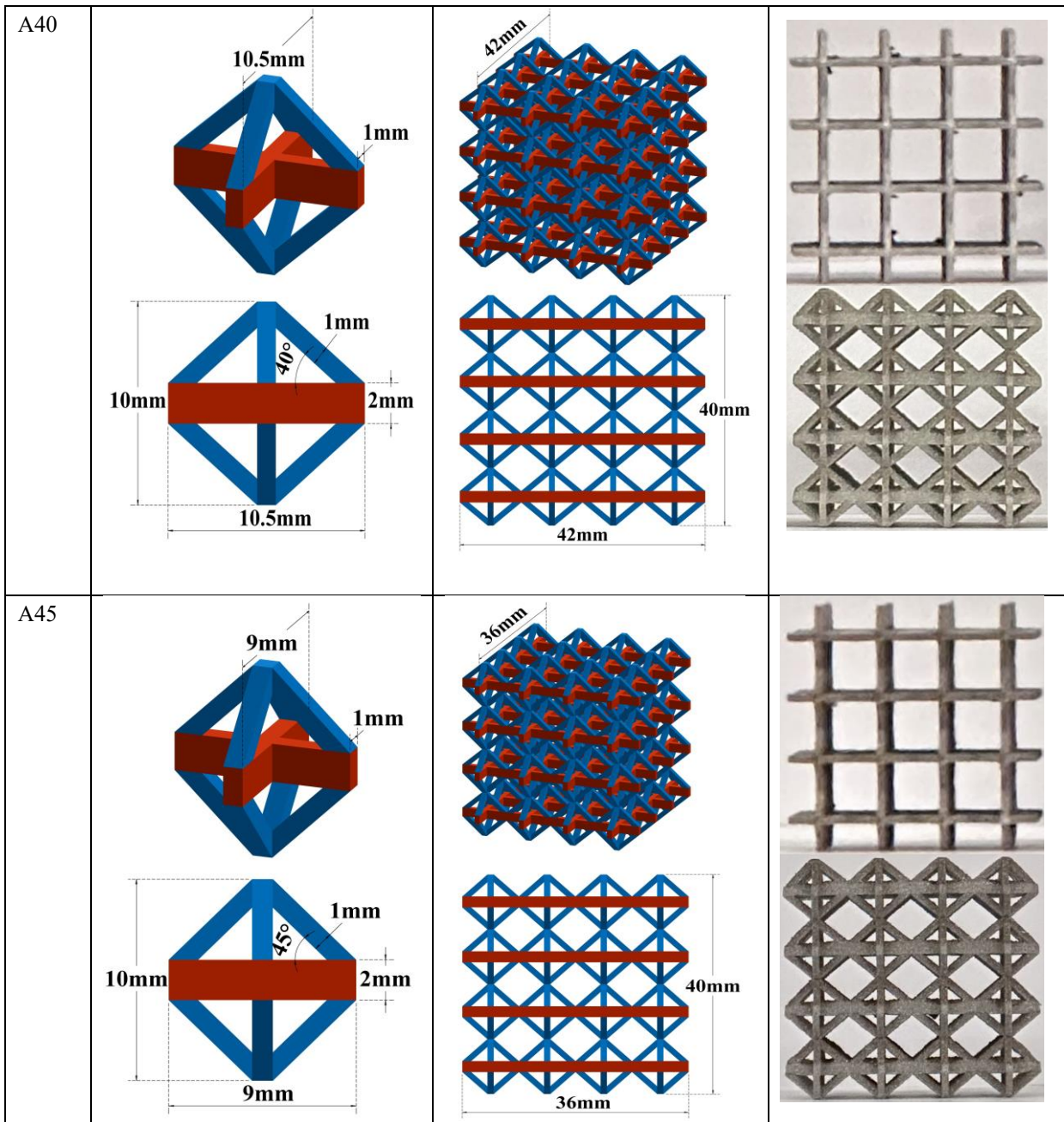
The first criterion imposes several implicit constraints on the design, which must be carefully considered. These include:

- Material Variation: Change in constituent is only permissible in the vertical direction. The composition must be homogeneous in the horizontal plane parallel to the build plate.
- Support-Free Design: The use of support structures is not viable, as their removal from within the lattice is exceedingly difficult. Therefore, the design must be self-supporting.
- Avoidance of Long Overhangs: Long overhangs are problematic due to the lack of supports, which increases the risk of build failure. The design must minimize such features to ensure a successful manufacturing process.

Five distinct unit cells were designed using the two alloys, leading to the creation of five different lattices (Table 3.2). The composition of the lattices varies by location, where red struts are made of higher CTE alloy, SS, while blue struts are made of low CTE alloy, Invar. The unit cell design is inspired by an octahedron, where the edges of the rectangle from the central plane were replaced with the diagonals of the rectangle. These unit cells, and the resulting lattices, are labelled as A30, A35, A40, and A45, where the number after 'A' represents the angle between the blue and red struts. This approach enables the assessment of how strut angle influences the NTE performance of the various designs.

Table 3.2 Metamaterial unit cells and lattice designs used in this study. SS 304L and Invar struts are shown in red and blue colours respectively.

Name	Unit Cell	Lattice Design	Printed Structure
A30			
A35			



3.2.6 Finite Element Simulations

The thermal expansion characteristics of the lattices were examined using the Static Structural module within ANSYS Simulation Software (ANSYS, Inc., PA, USA). The specific properties of the alloys used in these simulations were provided by ANSYS Granta. The simulations

accounted for variations in CTE and thermal conductivity by utilizing temperature-dependent values provided in ANSYS. The model was discretized with tetrahedral solid elements of quadratic order.

In configuring the lattice simulations, the following boundary conditions were established:

- The bottom face of one central unit cell in the lowest layer of the lattice was fixed.
- The bottom faces of the remaining unit cells in this layer were permitted horizontal movement (free X and Y displacements) but were restricted from any vertical movement (Z-displacement = 0 mm).
- The rest of the lattice was left free to expand.
- The temperature of the lattice was uniformly increased from 22°C to 300°C.

To ensure the accuracy of the finite element analysis (FEA) for the full lattice structures, a mesh sensitivity analysis was conducted, focusing on the net vertical contraction of a unit cell of A30 lattice with a fixed bottom face. This analysis determined that an element size of 0.3 mm was optimal, and this was subsequently adopted for the complete FEA.

3.2.7 LPBF fabrication of lattices

Metamaterial lattices were fabricated using the optimal parameters established for each material and their interfaces. The transition between alloys occurred at predetermined heights, corresponding to change of constituents in the lattice design. This necessitated pausing the manufacturing process to switch out the powder in the machine (Figure 3.1). The powder replacement procedure was conducted eight times throughout the fabrication, not including the initial loading of the powder and its final removal once the process was completed. All lattices were manufactured on the same build plate in one net process.

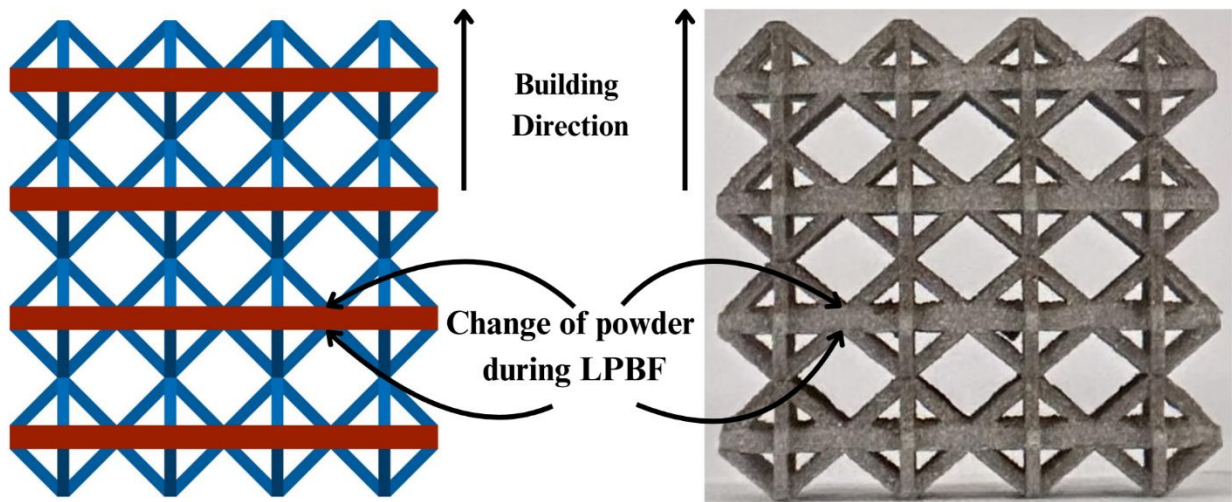


Figure 3.1 Change of alloys during fabrication of bimaterial lattices

3.2.8 Thermal Expansion Testing

The thermal expansion behaviour of the lattices was studied experimentally using digital image correlation (DIC) analysis. The samples were heated from 25°C to 300°C inside a controlled furnace environment. Tests were conducted on both heat-treated and untreated samples. The heat treatment involved a stress relief procedure, where the temperature was gradually increased by 3°C per minute to 300 °C, maintained for 2 hours, and then allowed to cool slowly within the furnace. The data was captured every 5 °C change in temperature. For thermal expansion testing using DIC, the temperature was increased from 20 °C to 300°C at the rate of 1 °C every three seconds. The resolution of the entire setup was 0.005mm. Vic-3D DIC system by Correlation Solutions Inc. (South Carolina, USA) was used for strain and deformation measurement with two cameras fitted with polarizers for deformation measurement. The highest priority was given to measurement of deformation in the expected direction of NTE.

3.3 Results and Discussion

3.3.1 Process Optimization

The achievement of a strong porosity and defect-free interface is essential for a strong bond

between the two alloys. In LPBF, energy density is a parameter used to provide a measure of energy applied per unit volume of powder by the laser and is defined as:

$$E = \frac{P}{v \cdot h \cdot t}$$

where P is laser power, v is scanning speed, h is hatch spacing and t is layer thickness [27]. This is the primary parameter considered in process optimization in LPBF, along with more specific process inputs like laser power, scanning speed and hatch spacing. In the first step, we investigated the optimum process parameters for each alloy individually. The single alloy optimum parameters results found are provided in Table 3.3.

Table 3.3 Optimal process parameters determined for the two alloys.

Material	Hatch Spacing (μm)	Laser Power (W)	Scanning Speed (mm/s)	Energy Density (J/mm³)
SS 304L	80	220	1100	62.5
Invar 36	100	200	870	57.5

The optimum parameters found optimal for SS are identical to those reported by Hou et al. [28] with an optimum energy density of 62.5 J/mm³. For Invar, the optimal energy density was found to be 57.5 J/mm³, marking a difference between the optimal process requirement of the two alloys. The part densities, measured using the Archimedes method, were found to be 99.6% for SS and 99.8% for Invar at their respective optimal parameters. Given the varying energy requirements of the two materials, a design of experiments matrix was established for process parameter optimization at the interface (Table 3.4). Due to the higher thermal conductivity of SS, it facilitates more efficient energy transfer to the build plate and was therefore printed first. Following the SS deposition, Invar was printed on top, with the parameters from table 3.4 applied to the Invar sections across different specimens.

Table 3.4 Design of experiments matrix used for identifying optimum process parameters for the interface

Sample No.	Hatch Spacing (mm)	Laser Power (W)	Scanning Speed (mm/s)	Energy Density (J/mm ³)
1	0.1	200	870	57.5
2	0.1	210	870	60.3
3	0.1	218	870	62.6
4	0.08	220	1100	62.5
5	0.1	270	1000	67.5
6	0.1	310	1000	77.5
7	0.1	270	1000	67.5
8	0.1	310	1000	77.5

The printed coupons underwent optical microscopy (OM) analysis following grinding and polishing. As illustrated in figure 3.2, it was observed that higher energy densities (samples 5, 6, 7, and 8) adversely affect bonding, resulting in the formation of pores at the interface. Conversely, samples 1 to 4 exhibited defect-free bonds; however, the energy densities of samples 1 and 2 were found to be below the optimal level required for SS. Given that LPBF involves the remelting of previously deposited layers, this could potentially cause less-than-ideal remelting of the earlier SS layers. To ensure reliability, samples 3 and 4 were deemed to possess a flawless interface. To keep the process straightforward, the parameters from sample 4, which match the optimal parameters for SS, were deemed optimal for the interface and subsequently used in the further fabrication processes in this study.

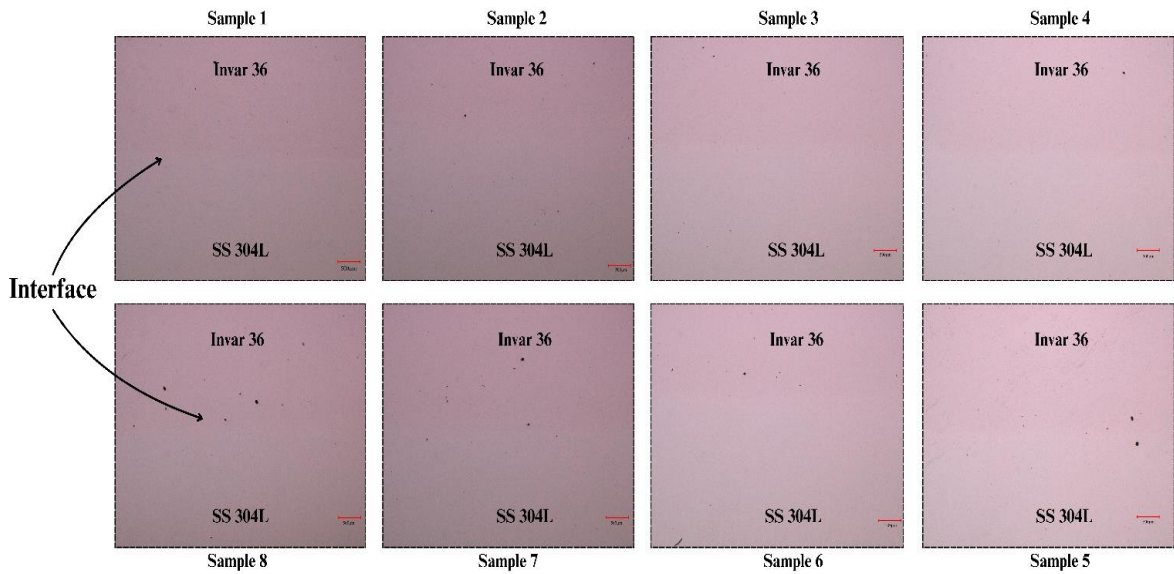


Figure 3.2 Interface observation using optical microscopy for process-parameter optimization

3.3.2 Microstructural Analysis

The microstructure of the interface produced using optimized processing parameters was further examined using optical microscopy (OM) after etching. Figure 3.3 presents a cross-sectional view along a plane with a normal parallel to the building direction in the Invar section. The cross-section reveals melt pools with a depth of 60-80 μm , accompanied by columnar grains elongated along the building direction. The LPBF process is characterized by rapid solidification, resulting in a significant temperature gradient between the solidified material and the unsolidified solution. During the process, heat dissipation occurs parallel to the build orientation, leading to the formation of numerous columnar grains that extend through the melt pools [29]. The micrographs of the interface, as in figure 3.3(c), highlight three distinct zones: the top Invar region, the central interfacial region, and the SS region at the bottom. Within the interfacial melt pools, a prominent circular flow pattern is evident, attributed to Marangoni convection. This Marangoni flow arises in the melt pools, moving outward from the laser impact

point due to density differences between the molten alloy in the hotter zones and the relatively cooler areas [30], [31]. The interfacial region also reveals embedded SS and Invar regions within each other resulting in compositional gradience with scattered heterogeneous zones.

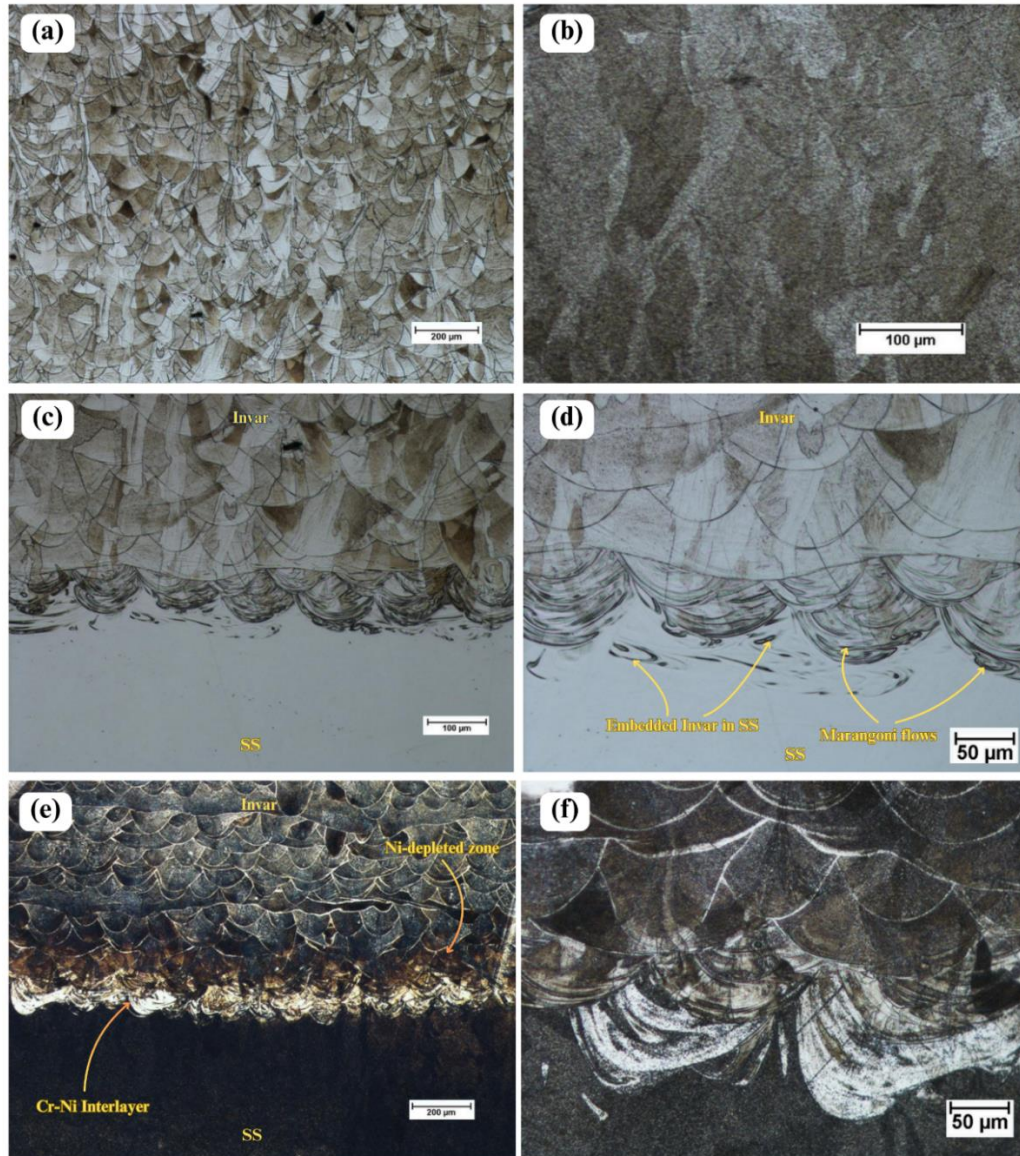


Figure 3.3 (a) Microstructure of Invar (b) microstructure of SS (c) Interfacial morphology (d) Marangoni flows and embeddings at the interface (e) Interlayer observed in overetched sample (f) Interlayer at high magnification

However, over-etching of the samples revealed intriguing observations. An interlayer is formed

at the fusion boundary, exhibiting higher corrosion resistance than both alloys. This is visible as a bright white layer within the melt pools in figure 3.3(a). This phenomenon is likely due to the segregation of alloying elements in this region, particularly Cr, which is well-known for improving the corrosion resistance of iron alloys [32]. Additionally, a more layer with increased corrosion is observed towards the Invar section, just above the white corrosion-resistant layer. This zone appears brown, likely due to corrosion of Fe, which is accelerated by the depletion of Ni in the Invar section as it tends to diffuse towards the SS region (interlayer). It is therefore suspected that the highly corrosion-resistant interlayer formed between the two alloys primarily consists of alloying elements, particularly Cr and Ni, which diffuse between the materials and accumulate in this interlayer. We believe that this Cr-Ni interlayer is beneficial for the stability of the inter-alloy bonding, as it effectively resists the formation of cracks or delamination at the interface. This is because an increased concentration of Cr in Fe-based composition increases high-temperature stability and hardness [33], while Ni improves toughness and strength without compromising ductility [34]. Interlayer formation has also been observed by Tan et al in additively manufactured bimaterial interfaces [35].

The micrographs from SEM are shown in figure 3.4. Cellular structures are observed in Invar with some elongated solidification cells cause by high cooling rates in LPBF [36]. The interfacial mixing of constituents is clearly observed with extensive circular flow creating embedded zones throughout the bonding region. The approximate thickness of diffusion region at the interface suggested by microscopic analysis is approximately 200 μm . The observations from OM regarding Marangoni flow and embedded regions at the interface were confirmed by SEM.

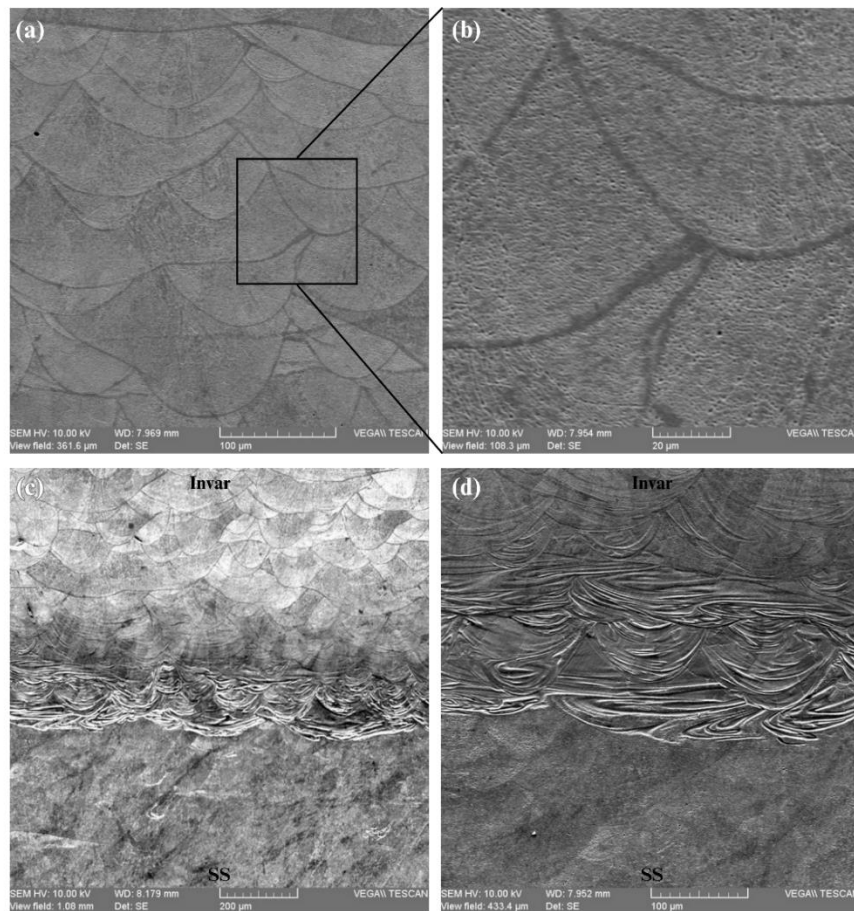


Figure 3.4 Scanning Electron Microscopy images: (a) Melt pools in Invar (b) Microstructure of Invar (c) Observed Interface (d) Marangoni flow with interfacial melt pools at high magnification

The elemental composition across the interface was assessed through Energy Dispersive Spectroscopy (EDS) with a linear distribution analysis. As delineated in table 3.1, the principal alloying constituents in stainless steel (SS) include Ni, Cr, Mn, and Si, whereas in mild steel (MS), they comprise Ni, Co, and Mo. Figure 3.5 illustrates the concentration profiles of these elements. The line was divided into over 500 points spanning a total distance of 200 μm , with the concentration of each element recorded at each point. It is important to emphasise that all values were normalised to effectively visualise the observed trends. The normalisation equation used was:

$$N_c = A_i/A_{max}$$

where A_i represents the concentration of the element at a given point i , and A_{max} denotes the maximum concentration of the element along the line.

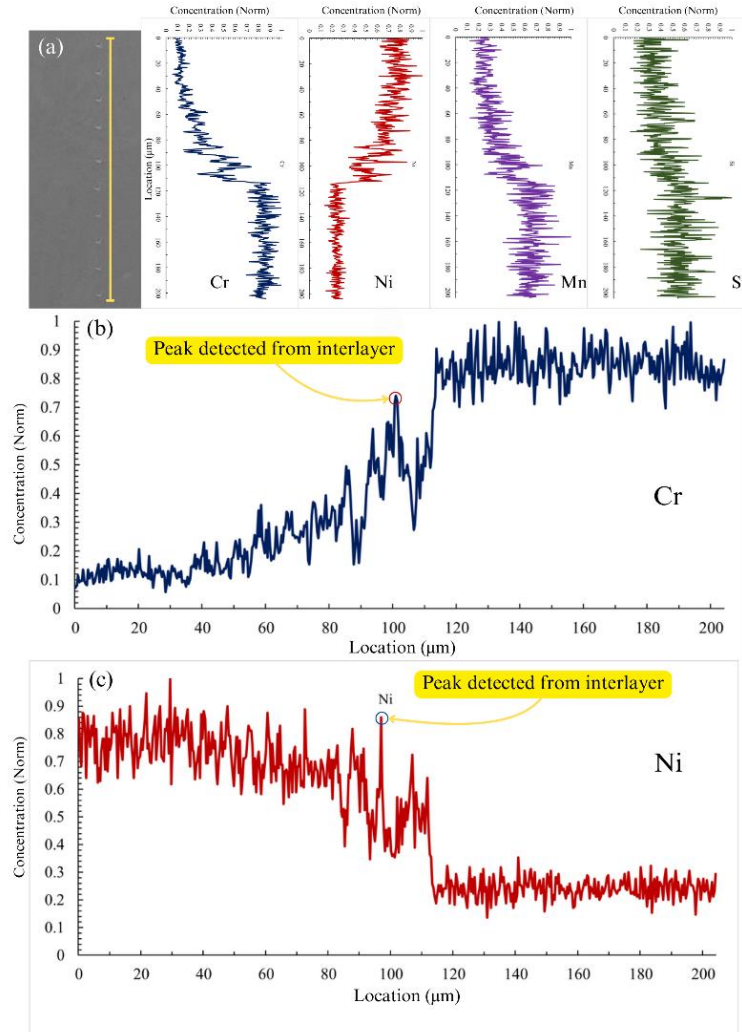


Figure 3.5 (a) Alloying element distributions across the interface based on linear EDS analysis (b) Interlayer peak identification from Cr-distribution curve (c) Interlayer peak identification from Ni-distribution curve.

3.3.3 Crystallographic Analysis

Electron Backscatter Diffraction (EBSD) analysis was employed to examine the grain morphology of the bimaterial samples and their interface. As depicted in figure 3.7, the

microstructure shows the interface along with the bulk regions on both sides. Both stainless steel (SS) and Invar exhibit irregular columnar grains that are elongated along the build direction, with finer grains present at the interface. Both materials possess an austenitic structure. Due to the extremely rapid cooling during the LPBF process, ferrite does not have sufficient time to nucleate and grow at the austenite grain boundaries, resulting in a predominantly austenitic microstructure. This contrasts with the microstructure typically produced by conventional manufacturing methods, where cellular ferrite is distributed within austenitic morphology [37]. The interface's microstructure reveals a continuous bond between the two alloys, with the finest grains predominantly located in the first melt pool layer at the interface, indicating that regions of entrapment lead to finer grain sizes.

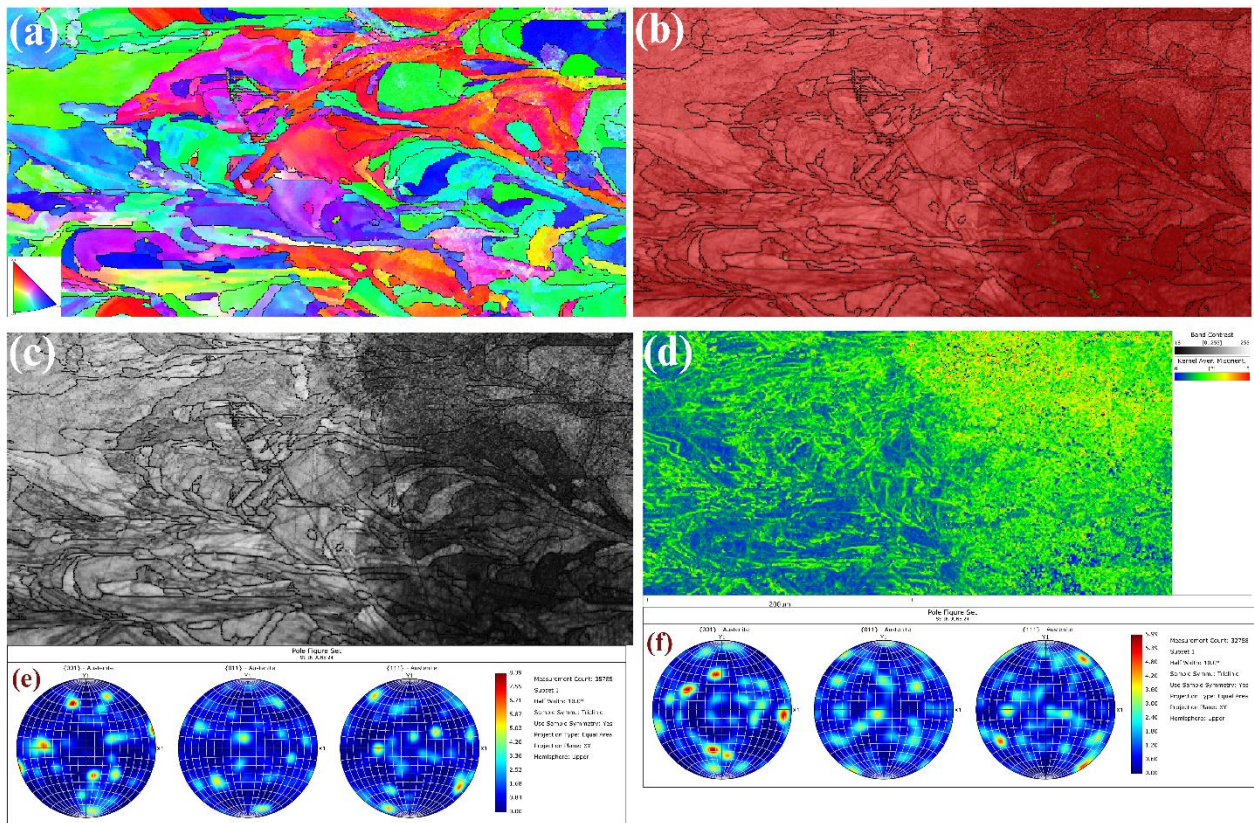


Figure 3.6 Interfacial Electron Backscatter Diffraction data (a) Inverse Pole Figure – Z Map; (b) Correlative Phase Distribution Map ;(c) Band Contrast Map;

(d) Kernel Average Misorientation Map (e) Pole figures for SS (f) Pole figures for Invar.

Kernel Average Misorientation (KAM) quantifies the average angular difference between a specific measurement point and its neighboring points, providing insights into local grain misorientation [38]. In this analysis, the local misorientation is calculated from the grain's center to points along the kernel's boundary. KAM is typically utilized to assess localized deformation, lattice distortions, and regions with high dislocation density, which reflect stored strain energy within the grain. Deformed grains generally show elevated KAM values due to increased dislocation activity. The KAM map of the interface, illustrated in figure 3.7(d), characterizes the micro-strain distribution. Notably, Invar exhibits a higher micro-strain than SS, with a gradual increase observed across the interface. In certain areas of the interfacial diffusion region, particularly in the upper central zone, the micro-strain is significantly higher than in other regions. This suggests that specific locations within the interface are subjected to increased strain, likely due to embedded Invar or SS regions within the interfacial layer surrounded by other constituent. These regions experience greater stress due to the thermal contraction mismatch between the two materials during the rapid cooling phase of LPBF. This leads to increased micro-strain within the grain structure at the interface.

3.3.4 Mechanical Performance Analysis

Nano-hardness testing at the interface supports the idea of material intermixing between the two alloys. The hardness values of Invar and SS are approximately 200 HV and 300 HV, respectively, as shown in figure 3.7. A noticeable increase in nano-hardness is observed across the interface, with a gradual rise when transitioning from Invar to SS. This confirms the existence of a compositional gradient at the interface, which corresponds to the hardness

gradient. The gradual change takes place from indentation 3 to indentation 7, thereby predicting the length of diffusion range to be 200 μm .

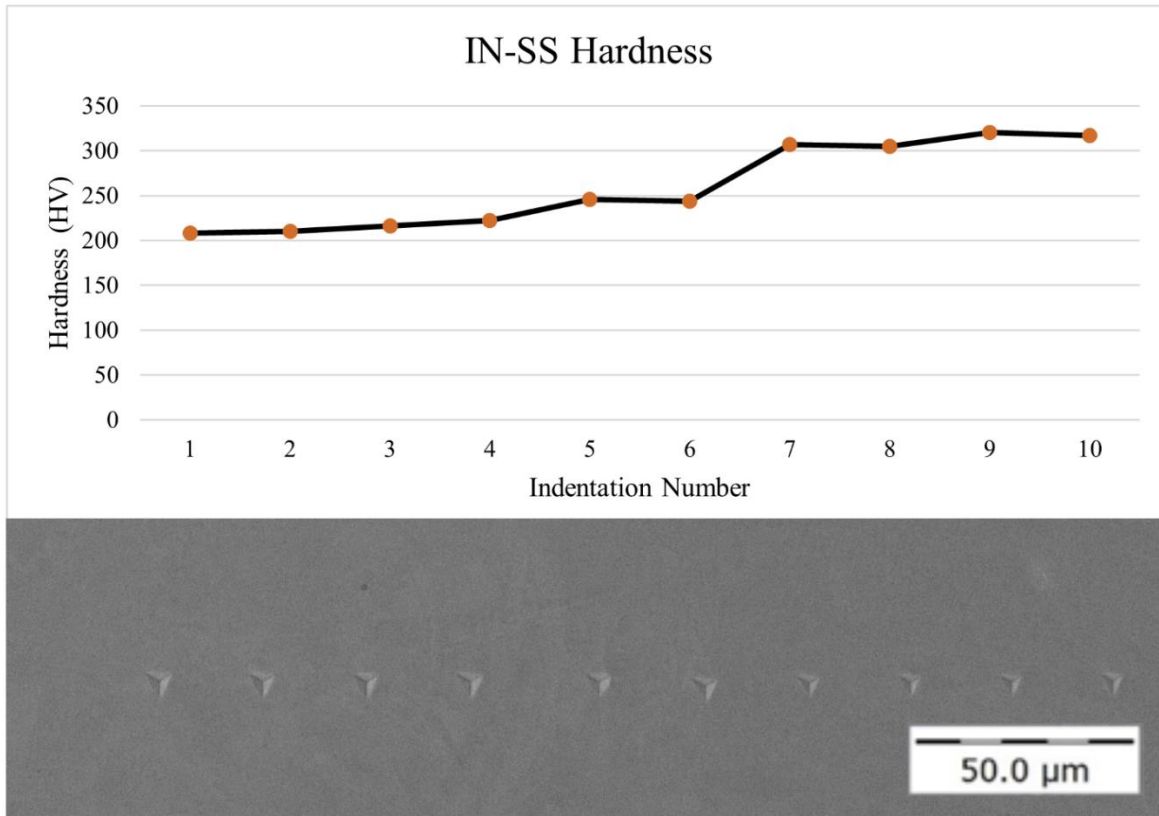


Figure 3.7 Nano-hardness across the interface

The variation in penetration depth along the scratch path is depicted in figure 3.8. Initially, the scratch starts in the SS region, with a penetration depth of about 6 μm . As the indenter crosses the interface, the depth progressively increases to around 9 μm within the Invar region, consistent with nano-hardness measurements, verifying that Invar is softer and more prone to scratching than SS. The region showing this reduction spans approximately 200 μm , which aligns with the interface length identified by EDS in figure 3.5, as well as the nano-hardness gradient presented in figure 3.7. Acoustic emission data (figure 3.8(b)) exhibits significant fluctuations in the Invar region beyond the interface. These fluctuations indicate the emission

of elastic waves caused by abrupt material deformation [39]. The pronounced acoustic emissions suggest the formation and propagation of microcracks, indicative of brittle behaviour in the material.

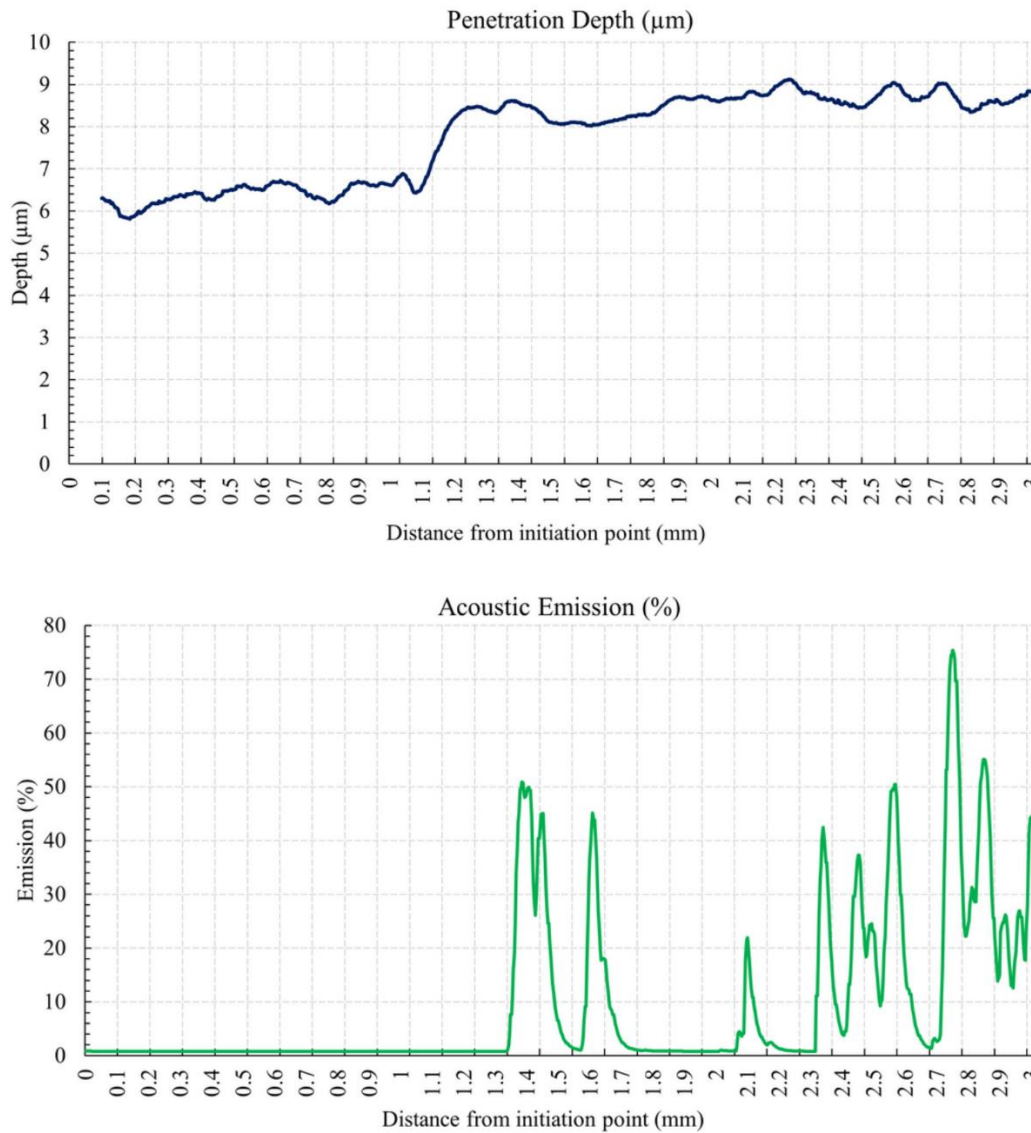


Figure 3.8 (a) Depth of penetration, and (b) acoustic emission, across the interface using scratch resistance testing

3.3.5 Simulation

The simulation results indicate vertical contraction in three lattice structures, indicating vertical

NTE (figure 3.9). Lattices with Invar-SS strut angles of 30, 35, and 40 degrees exhibit overall contraction as the temperature increases, whereas the lattice with a 45-degree strut angle shows a slight overall expansion, approaching nearly zero. The angle between struts of differing materials is a critical factor influencing NTE behaviour and serves as an important design parameter for NTE metamaterials. Furthermore, increasing the thickness of the Invar struts restricts the overall contraction by reducing the vertical shrinkage, which arises from the stretching of low-expansion Invar struts by the more expansible SS. As anisotropic NTE metamaterials, all lattice designs exhibit positive expansion in the horizontal plane. Stress analysis revealed increased stress concentrations near the connecting joints. This behaviour is expected, given the differential expansion of the two materials, with the bonded joints working to maintain the connection between struts of differing materials. However, these stresses remain within the allowable limits of the two alloys.

Table 3.5 Negative Thermal Expansion Performance of different lattices using FEA

Metamaterial	Vertical Deformation - FEA (mm)	Vertical CTE - FEA ($\times 10^{-6}$ m/m$^{\circ}$C)
A30	-0.12	-10.8
A35	-0.06	-5.4
A40	-0.016	-1.4
A45	0	0

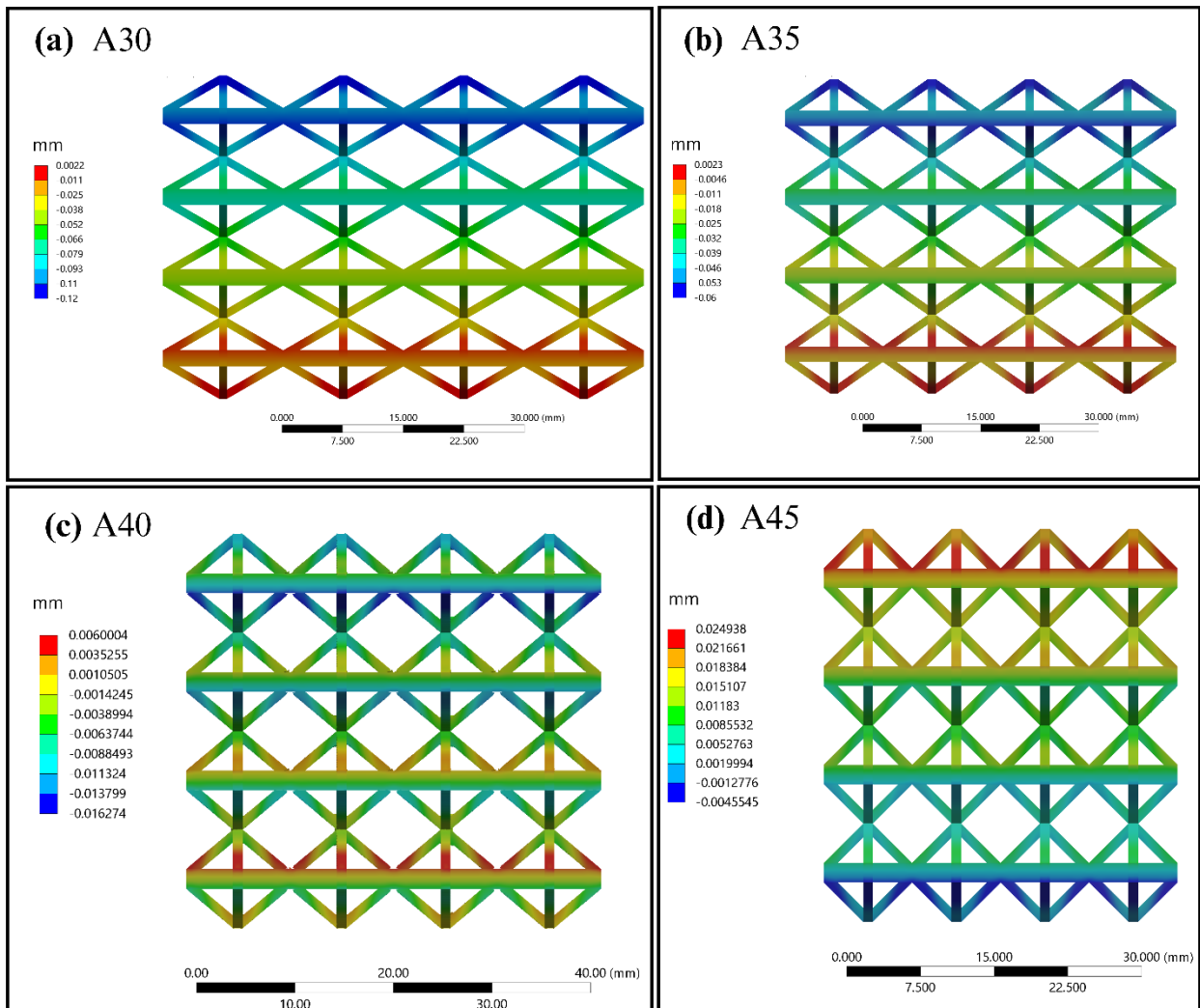


Figure 3.9 Finite element analysis results for thermal expansion of lattices in vertical direction (a) A30 (b) A35 (c) A40 (d) A45

3.3.6 Experimental Thermal Testing

DIC experiments were conducted for A30 specimen after fabrication. This specimen was chosen due to its superior predictions for NTE from FEA simulations as compared to other designs. The contours observed for deformation in vertical direction i.e. the direction of expected contraction are shown in figure 3.10. Due to the limited viewing window of the furnace, only three vertical stacks of layers were observed, rather than the full height of four stacks. The deformation measured at the top of the third vertical stack was approximately -0.07 mm, which closely aligns

with the FEA-predicted value of -0.08 mm. The minor deviation in deformation is attributed to differences between the properties of LPBF-manufactured stainless steel and Invar alloys and the properties of their conventionally manufactured counterparts used in the FEA predictions. Moreover, the FEA assumed a sharp interface, whereas this study revealed a diffusion zone of about 200 μm at the interface. During thermal testing, the second stack of layers displayed expansion. This is likely due to defects and warpage in certain struts during fabrication, which become more pronounced under high-temperature testing, affecting nearby struts and causing abnormal behaviour in some unit cells. This effect is more noticeable in unit cells located at the ends of the lattice, where connectivity is limited.

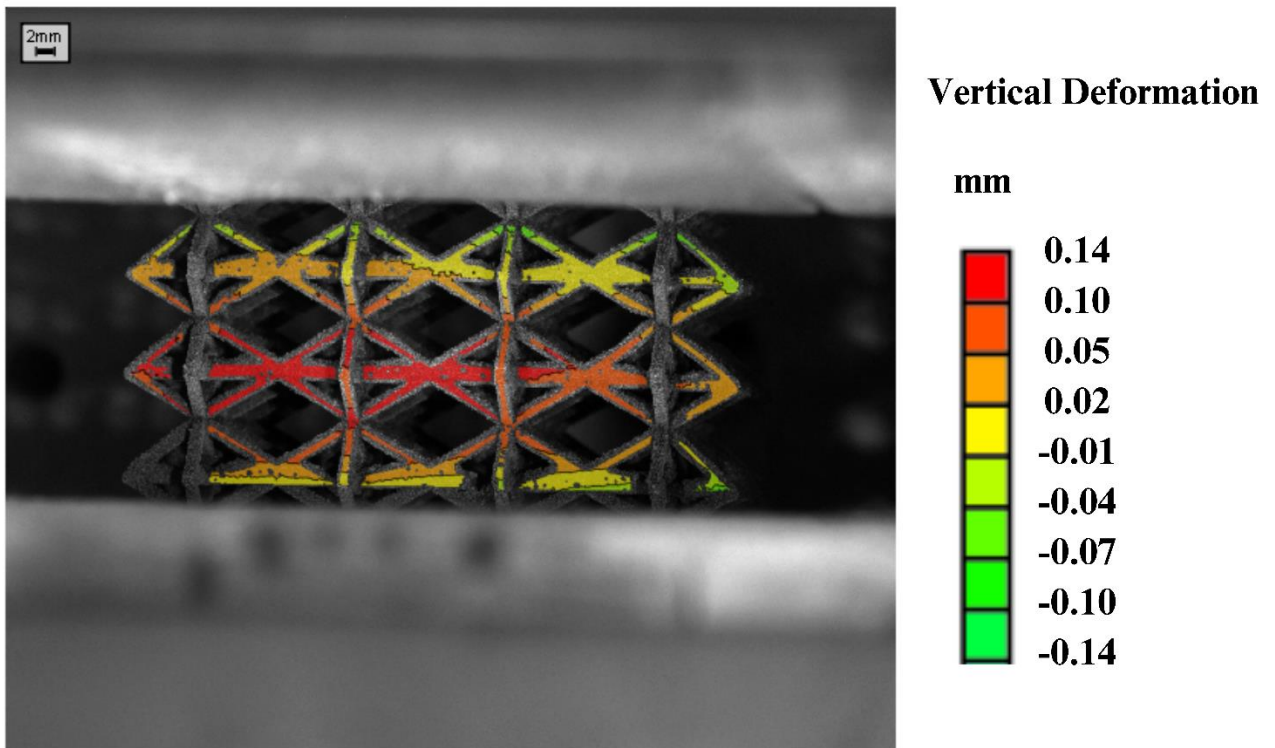


Figure 3.10 Vertical deformation in A30 lattice using DIC analysis

3.4 Conclusion

In this study, we successfully fabricated negative thermal expansion (NTE) mechanical metamaterials using metal additive manufacturing (LPBF) of grade 304 stainless steel and Invar 36. The research involved a comprehensive analysis encompassing process parameter development, morphological characterization, interface optimization, mechanical testing, finite element analysis, and thermal testing via digital image correlation. The principal conclusions drawn from this study are as follows:

1. **Interfacial Bonding:** The complete additive manufacturing process, employing optimized parameters, yielded a strong, defect-free interface between the two alloys. This robust bonding is primarily attributed to two factors:
 - i. Firstly, there is significant elemental diffusion across the interface, which substantially strengthens the bond. In multi-material additive manufacturing, delamination is a critical issue that can lead to catastrophic failure. However, the gradual transition in composition, driven by the diffusion of elements such as Cr and Ni, significantly alleviates strain, as evidenced by the KAM map.
 - ii. Secondly, no brittle intermetallic phases were observed to form during the alloy mixing at the interface, a crucial factor in preventing fractures in bimaterial systems. This absence of brittle intermetallics underscores the integrity of the interface.
2. **Mechanical Testing of the Interface:** The mechanical properties of the interface were thoroughly assessed through nano-hardness and scratch testing, which strongly supported the morphological observations of robust bonding. Key findings include:
 - i. Nano-hardness testing revealed a compositional gradient across the interface, leading to a gradual variation in hardness within the diffusion zone.

- ii. Scratch testing demonstrated smooth, debris-free scratches in the SS region, transitioning to slightly jagged, debris-laden scratches in the Invar region, indicative of slight brittle behaviour in LPBF-manufactured Invar. The sharper, higher-amplitude acoustic emissions detected in the Invar region further confirm its brittle nature at certain points. The gradual reduction in penetration depth across the interface also reinforces the existence of a distinct compositional gradient.
3. Finite Element Analysis of Lattices: The numerical analysis concluded the following:
 - i. The best NTE performance is shown by A30 lattice, with a CTE of $-10.8 \times 10^{-6} \text{ m/m}^\circ\text{C}$.
 - ii. NTE performance improves as the angle between struts of different compositions decreases.
 4. Experimental Thermal Testing: Thermal testing using DIC confirmed the NTE behaviour of the A30 specimen, which was selected for testing based on superior FEA predictions.
 - i. The measured deformation closely matched the predicted values, with minor deviations attributed to the inherent differences between LPBF-manufactured materials and their conventionally manufactured counterparts, as well as the presence of a diffusion zone at the interface.
 - ii. The observed expansion in certain layers, particularly in the second stack, was linked to fabrication defects and warpage in the struts, which were exacerbated during high-temperature testing.

In conclusion, this study demonstrates the successful fabrication and optimization of multi-material lattices with negative thermal expansion properties using LPBF. The comprehensive approach, which integrated process parameter optimization, mechanical and thermal testing, as well as finite element analysis, highlights the critical role of interfacial bonding and lattice

geometry in achieving reliable NTE performance. The findings highlight the importance of controlling manufacturing parameters to minimize defects and warpage, ensuring robust interfacial bonding and consistent thermal behaviour. Future work should focus on refining lattice designs and exploring alternative material combinations to further enhance NTE performance and address fabrication challenges, advancing the development of novel mechanical metamaterials for real-world applications.

References

- [1] Y. Chen, Y.-W. Mai, and L. Ye, “Perspectives for multiphase mechanical metamaterials,” *Materials Science and Engineering: R: Reports*, vol. 153, p. 100725, 2023, doi: <https://doi.org/10.1016/j.mser.2023.100725>.
- [2] P. Sinha and T. Mukhopadhyay, “Programmable multi-physical mechanics of mechanical metamaterials,” *Materials Science and Engineering: R: Reports*, vol. 155, p. 100745, 2023, doi: <https://doi.org/10.1016/j.mser.2023.100745>.
- [3] A. Airoidi, N. Novak, F. Sgobba, A. Gilardelli, and M. Borovinšek, “Foam-filled energy absorbers with auxetic behaviour for localized impacts,” *Materials Science and Engineering: A*, vol. 788, p. 139500, 2020, doi: <https://doi.org/10.1016/j.msea.2020.139500>.
- [4] J. Mueller, J. R. Raney, K. Shea, and J. A. Lewis, “Architected Lattices with High Stiffness and Toughness via Multicore–Shell 3D Printing,” *Advanced Materials*, vol. 30, no. 12, p. 1705001, Mar. 2018, doi: <https://doi.org/10.1002/adma.201705001>.
- [5] D. Dubey, A. S. Mirhakimi, and M. A. Elbestawi, “Negative Thermal Expansion Metamaterials: A Review of Design, Fabrication, and Applications,” *Journal of Manufacturing and Materials Processing*, vol. 8, no. 1, 2024, doi: 10.3390/jmmp8010040.
- [6] P. Lightfoot, D. A. Woodcock, M. J. Maple, L. A. Villaescusa, and P. A. Wright, “The widespread occurrence of negative thermal expansion in zeolites,” *J Mater Chem*, vol. 11, no. 1, pp. 212–216, 2001, doi: 10.1039/B002950P.
- [7] J. Sheng et al., “Thermal expansion behavior of copper matrix composite containing negative thermal expansion PbTiO₃ particles,” *Mater Des*, vol. 132, pp. 442–447, 2017, doi: <https://doi.org/10.1016/j.matdes.2017.06.061>.
- [8] M. Kofteros, S. Rodriguez, V. Tandon, and L. E. Murr, “A preliminary study of thermal

expansion compensation in cement by ZrW₂O₈ additions,” *Scr Mater*, vol. 45, no. 4, pp. 369–374, 2001, doi: [https://doi.org/10.1016/S1359-6462\(01\)01009-0](https://doi.org/10.1016/S1359-6462(01)01009-0).

[9] B. Yu, Z. Xu, R. Mu, A. Wang, and H. Zhao, “Design of Large-Scale Space Lattice Structure with Near-Zero Thermal Expansion Metamaterials,” *Aerospace*, vol. 10, no. 3, Mar. 2023, doi: [10.3390/aerospace10030294](https://doi.org/10.3390/aerospace10030294).

[10] P. Juasiripukdee, I. Maskery, I. Ashcroft, and R. Leach, “Low thermal expansion machine frame designs using lattice structures,” *Applied Sciences (Switzerland)*, vol. 11, no. 19, Oct. 2021, doi: [10.3390/app11199135](https://doi.org/10.3390/app11199135).

[11] A. R. Eriksson and T. Albrektsson, “Temperature threshold levels for heat-induced bone tissue injury: A vital-microscopic study in the rabbit,” *J Prosthet Dent*, vol. 50, no. 1, pp. 101–107, 1983, doi: [https://doi.org/10.1016/0022-3913\(83\)90174-9](https://doi.org/10.1016/0022-3913(83)90174-9).

[12] D. Devoto, P. Paul, S. Narumanchi, and M. Mihalic, “Reliability of Bonded Interfaces for Automotive Power Electronics,” *Proceedings of the ASME 2013 International Technical Conference and Exhibition on Packaging and Integration of Electronic and Photonic Microsystems*. Volume 1, Jul. 2013.

[13] H. Z. Zhong et al., “Design of conformal lattice metamaterials for additive manufacturing,” *Curr Opin Solid State Mater Sci*, vol. 30, p. 101162, 2024, doi: <https://doi.org/10.1016/j.cossms.2024.101162>.

[14] J. Gao et al., “Rational designs of mechanical metamaterials: Formulations, architectures, tessellations and prospects,” *Materials Science and Engineering: R: Reports*, vol. 156, p. 100755, 2023, doi: <https://doi.org/10.1016/j.mser.2023.100755>.

[15] Y. Jia, K. Liu, and X. S. Zhang, “Modulate stress distribution with bio-inspired irregular architected materials towards optimal tissue support,” *Nat Commun*, vol. 15, no. 1, p. 4072,

2024, doi: 10.1038/s41467-024-47831-2.

[16] V. S. Deshpande, M. F. Ashby, and N. A. Fleck, “Foam topology: bending versus stretching dominated architectures,” *Acta Mater*, vol. 49, no. 6, pp. 1035–1040, 2001, doi: [https://doi.org/10.1016/S1359-6454\(00\)00379-7](https://doi.org/10.1016/S1359-6454(00)00379-7).

[17] A. Mussatto, “Research progress in multi-material laser-powder bed fusion additive manufacturing: A review of the state-of-the-art techniques for depositing multiple powders with spatial selectivity in a single layer,” *Results in Engineering*, vol. 16, p. 100769, 2022, doi: <https://doi.org/10.1016/j.rineng.2022.100769>.

[18] C. Wei et al., “Multi-material additive-manufacturing of tungsten - copper alloy bimetallic structure with a stainless-steel interlayer and associated bonding mechanisms,” *Addit Manuf*, vol. 50, Feb. 2022, doi: 10.1016/j.addma.2021.102574.

[19] Y. Bai, J. Zhang, C. Zhao, C. Li, and H. Wang, “Dual interfacial characterization and property in multi-material selective laser melting of 316L stainless steel and C52400 copper alloy,” *Mater Charact*, vol. 167, p. 110489, 2020, doi: <https://doi.org/10.1016/j.matchar.2020.110489>.

[20] M. G. Scaramuccia, A. G. Demir, L. Caprio, O. Tassa, and B. Previtali, “Development of processing strategies for multigraded selective laser melting of Ti6Al4V and IN718,” *Powder Technol*, vol. 367, pp. 376–389, May 2020, doi: 10.1016/J.POWTEC.2020.04.010.

[21] K. Chen et al., “Selective laser melting 316L/CuSn10 multi-materials: Processing optimization, interfacial characterization and mechanical property,” *J Mater Process Technol*, vol. 283, Sep. 2020, doi: 10.1016/j.jmatprotec.2020.116701.

[22] D. Fang, Q. Jun-mao, and D. Hao-hua, “Study on Thermal Physical Properties of 304 Stainless Steel,” in *6th International Symposium on High-Temperature Metallurgical*

Processing, T. Jiang, J.-Y. Hwang, G. R. F. Alvear F., O. Yücel, X. Mao, H. Y. Sohn, N. Ma, P. J. Mackey, and T. P. Battle, Eds., Cham: Springer International Publishing, 2016, pp. 99–104. doi: 10.1007/978-3-319-48217-0_13.

[23] C. Qiu, N. J. E. Adkins, and M. M. Attallah, “Selective laser melting of Invar 36: Microstructure and properties,” *Acta Mater*, vol. 103, pp. 382–395, 2016, doi: <https://doi.org/10.1016/j.actamat.2015.10.020>.

[24] ASTM Standard B962-23, “Standard Test Methods for Density of Compacted or Sintered Powder Metallurgy (PM) Products Using Archimedes’ Principle,” ASTM International, 2023, doi: 10.1520/B0962-23.

[25] International Standard ISO 14577-1:2015, “Metallic materials — Instrumented indentation test for hardness and materials parameters,” International Organization for Standardization, 2015.

[26] ASTM Standard C1624-22, “Standard Test Method for Adhesion Strength and Mechanical Failure Modes of Ceramic Coatings by Quantitative Single Point Scratch Testing,” ASTM International, 2022.

[27] G. V de Leon Nope, L. I. Perez-Andrade, J. Corona-Castuera, D. G. Espinosa-Arbelaez, J. Muñoz-Saldaña, and J. M. Alvarado-Orozco, “Study of volumetric energy density limitations on the IN718 mesostructure and microstructure in laser powder bed fusion process,” *J Manuf Process*, vol. 64, pp. 1261–1272, 2021, doi: <https://doi.org/10.1016/j.jmapro.2021.02.043>.

[28] J. Hou, W. Chen, Z. Chen, K. Zhang, and A. Huang, “Microstructure, tensile properties and mechanical anisotropy of selective laser melted 304L stainless steel,” *J Mater Sci Technol*, vol. 48, pp. 63–71, 2020, doi: <https://doi.org/10.1016/j.jmst.2020.01.011>.

[29] Z. Hu et al., “Columnar grain width control for SS316L via hatch spacing manipulation in

laser powder bed fusion,” *Mater Res Lett*, vol. 11, no. 3, pp. 231–238, Mar. 2023, doi: 10.1080/21663831.2022.2140018.

[30] S. J. Clark, C. L. A. Leung, Y. Chen, L. Sinclair, S. Marussi, and P. D. Lee, “Capturing Marangoni flow via synchrotron imaging of selective laser melting,” *IOP Conf Ser Mater Sci Eng*, vol. 861, no. 1, p. 012010, 2020, doi: 10.1088/1757-899X/861/1/012010.

[31] J. Yang et al., “Experimental quantification of inward Marangoni convection and its impact on keyhole threshold in laser powder bed fusion of stainless steel,” *Addit Manuf*, vol. 84, p. 104092, 2024, doi: <https://doi.org/10.1016/j.addma.2024.104092>.

[32] B. Sun, X. Zuo, X. Cheng, and X. Li, “The role of chromium content in the long-term atmospheric corrosion process,” *Npj Mater Degrad*, vol. 4, no. 1, p. 37, 2020, doi: 10.1038/s41529-020-00142-5.

[33] P. Dupin, J. Saverna, and J. M. Schissler, “A Structural Study of Chromium White Cast Irons.(Retroactive Coverage),” *Transactions of the American Foundrymen’s Society.*, vol. 90, pp. 711–718, 1982.

[34] D.-Y. Ryoo, N. Kang, and C.-Y. Kang, “Effect of Ni content on the tensile properties and strain-induced martensite transformation for 304 stainless steel,” *Materials Science and Engineering: A*, vol. 528, no. 6, pp. 2277–2281, 2011, doi: <https://doi.org/10.1016/j.msea.2010.12.022>.

[35] C. Tan et al., “In-situ synthesised interlayer enhances bonding strength in additively manufactured multi-material hybrid tooling,” *Int J Mach Tools Manuf*, vol. 155, Aug. 2020, doi: 10.1016/j.ijmachtools.2020.103592.

[36] Y. Zhou, Q. Yang, R. Huang, J. Zhou, K. Wei, and X. Yang, “Influence of laser powder bed fusion process on microstructures and low cycle fatigue performance of Invar 36 alloy,” *J*

Mater Sci, vol. 59, no. 7, pp. 3133–3149, 2024, doi: 10.1007/s10853-024-09331-y.

[37] A. Hunter and M. Ferry, “Phase formation during solidification of AISI 304 austenitic stainless steel,” *Scr Mater*, vol. 46, no. 4, pp. 253–258, 2002, doi: [https://doi.org/10.1016/S1359-6462\(01\)01215-5](https://doi.org/10.1016/S1359-6462(01)01215-5).

[38] S.-S. Rui et al., “Correlations between two EBSD-based metrics Kernel Average Misorientation and Image Quality on indicating dislocations of near-failure low alloy steels induced by tensile and cyclic deformations,” *Mater Today Commun*, vol. 27, p. 102445, 2021, doi: <https://doi.org/10.1016/j.mtcomm.2021.102445>.

[39] Z. Nazarchuk, V. Skalskyi, and O. Serhiyenko, “Acoustic emission,” *Foundations of Engineering Mechanics*, 2017.

4 Chapter 4 Summary, Strengths and Future Work

4.1 Summary

This research explored the design, fabrication, and characterization of negative thermal expansion metamaterials using the Laser Powder Bed Fusion technique. The primary aim was to manufacture these metamaterials with the alloys AISI 304L stainless steel and Invar 36, as well as AISI 304L stainless steel and SAE 300 maraging steel. The study focused on optimizing the process parameters for multimaterial additive manufacturing and evaluating the thermal and mechanical properties of the resulting bimaterial interfaces alongwith design, FEA simulations, production and testing of lattice metamaterials based on optimum interface strengths.

The study commenced with a detailed investigation of the optimal LPBF parameters for each constituent material. This stage was critical for ensuring the successful fabrication of high-quality multimaterial lattices. The materials SS304 and Invar 36, as well as SS304 and MS300, were chosen based on their differing coefficients of thermal expansion, with the expectation that these differences would contribute to the NTE behavior in the fabricated metamaterials.

Interfacial bonding between these materials was a crucial factor for the success of the designs. Process optimization focused on achieving strong, defect-free interfaces through the diffusion of key elements like chromium (Cr) and nickel (Ni). The mechanical integrity of the fabricated lattices was confirmed through extensive testing, including tensile, nano-hardness and scratch resistance evaluations, as well as FEA simulations to predict the thermal behavior of the NTE lattices.

The fabricated lattices demonstrated the desired NTE properties, with experimental results roughly aligning with FEA predictions. The ability to control thermal expansion through the design of the lattice structures offers promising applications for aerospace, precision instruments, and other fields where thermal stability is critical.

4.2 Strengths

One of the main strengths of this research is the successful fabrication of robust, defect-free interfaces in multimaterial systems using LPBF. Achieving such interfaces is crucial in additive manufacturing, especially when working with materials that have substantially different thermal expansion coefficients. The ability to fabricate these interfaces without the formation of brittle intermetallic phases is a significant achievement, which ensures the structural integrity of the metamaterials under thermal and mechanical loads.

Another strength lies in the comprehensive approach adopted for the characterization of the interfaces. This study utilized advanced techniques, including nano-hardness and scratch resistance tests, to assess the mechanical properties of the interfaces. Additionally, EBSD analysis provided insights into the grain orientation and phase distribution across the interface, offering a detailed understanding of the metallurgical phenomena at play.

The use of FEA simulations to predict the thermal behavior of the fabricated lattices adds further strength to the study. These simulations allowed for the optimization of lattice designs before fabrication, saving both time and resources. The agreement between the FEA predictions and experimental results validates the effectiveness of the simulation models used.

4.3 Limitations

Despite the success of the research, some limitations were encountered. One limitation is the restricted design freedom in LPBF fabrication. The requirement for support-free designs, especially in complex lattice structures, imposes constraints on the geometry of the lattices. The restrictions exist on length of overhangs and angle of struts for successful fabrication using LPBF. In addition, due to the restrictions of the machine, change of constituent was only

possible in the vertical direction which hugely affects the design flexibility of multimaterial lattices. Although the study explored various lattice designs, the potential for further optimization exists.

The study also highlighted the challenges of managing the differential thermal properties of the constituent materials during fabrication. The differences in CTE between SS304 and Invar 36 or MS300 can lead to residual stresses and, in some cases, delamination. While these issues were mitigated through process optimization, further research is needed to fully understand the long-term performance of these interfaces under cyclic thermal loading and fatigue related applications.

4.4 Future Work

Building on the findings of this research, several avenues for future work can be proposed. First, further optimization of the multimaterial interface with new materials is necessary to enhance the mechanical properties of the bond between two alloys. This could involve exploring alternative material combinations or adjusting the process parameters to create a more uniform interface.

Second, future studies should focus on the long-term performance of NTE metamaterials, particularly under cyclic thermal and mechanical loading. While this study demonstrated the feasibility of fabricating NTE metamaterials with LPBF, the long-term durability of these materials in real-world applications remains to be tested. Fatigue testing and thermal cycling experiments would provide valuable insights into the reliability of the fabricated structures.

Another important direction for future research is the exploration of alternative lattice geometries. The study primarily focused on stretch-dominated lattices, but there is potential for further optimization of the lattice design to improve NTE performance. Bending-dominated

architectures, for instance, could offer improved thermal stability while reducing the reliance on complex geometries that are difficult to fabricate with LPBF.

Furthermore, future work could explore the integration of additional materials into the lattice structures. The current study focused on bimaterial systems, but the incorporation of a third or fourth material could offer additional control over the thermal and mechanical properties of the metamaterials. This would give rise to new possibilities for tailoring the properties of NTE metamaterials to specific applications.

Finally, there is significant potential for expanding the producibility of NTE metamaterials by modification of existing machines to allow variation in constituents in directions other than vertical or building direction. Also, care must be taken to ensure a sharp interface in these other directions.

In conclusion, this research has demonstrated the successful design, fabrication, and characterization of NTE metamaterials using LPBF. The study has highlighted the strengths and limitations of using SS304 and Invar 36 or MS300 in bimaterial systems, with a focus on optimizing the interfacial properties for improved mechanical and thermal performance. While a few challenges remain, particularly in terms of interface uniformity and design freedom, the findings of this study provide a strong foundation for future research in the field of NTE metamaterials.